# Development of Large-Scale Models and HVDC Control Strategies to Improve Resiliency of North American Power System

A Dissertation Presented for the
Doctor of Philosophy
Degree
The University of Tennessee, Knoxville

Lakshmi Sundaresh

May 2020

*dedicated to my family*

# Acknowledgments

I am really grateful to my advisor Dr. Yilu Liu for giving me this great opportunity to learn. I also thank her for always pushing me to achieve my goals. I would like to thank my family: my mother Sheela, my uncle Krishna Kumar, my sister Sanjana, my brother-in-law Sandeep, my nephew Vishnu, and my late grandmother VijayaLakshmi for their unconditional love and support. I would like to thank my aunt Lakshmi, uncle Venkatesh, and cousins Ananya and Aditi who have given me a home away from home in California. I could not have done this without their help.

I would like to express my utmost gratitude to Dr. Fran Li, Dr. Hector Pulgar, and Dr. Jiuping Pan for being a part of my committee. I would like to thank my friends Rakesh, Jerome, and Dony for always being there to pull my spirits up and also feed me dinner when I was too lazy to cook. I would like to thank Apoorva, Bailey and Roshan for being there for me through thick and thin. I would like to thank the faculty and staff of the CURENT center and the EECS department at UTK for providing a great platform to help me become a better engineer.

As a graduate student, I had the opportunity to work with industry members on multiple projects. I would like to thank Dr. Mark Buckner and Dr. Alfonso Tarditi from ORNL; Dr. Marcus Monroe, Dr. Lothar Wenzel, and Dr. Ben Black from National Instruments; Dr. Hongming Zhang and Dr. Slaven Kincic from Peak Reliability; and Dr. Jiuing Pan from ABB Research for their guidance. I have learned a lot from my peers at the Power IT Lab. I am very grateful to Shutang You, Yu Su, Micah Till, Abby Till, Mirka, Weikang Wang , Lin Zhu, Kaiqi Sun and Yinfeng Zhao for their friendship and support.

# Abstract

With drastic transformation of the electrical power system, the challenges related to planning, operation, and maintenance of power systems are increasing. The controls and operating procedures of the power systems have to be re-evaluated because certain inherent characteristics of the power system—like inertia, response time, and control behavior—are changing drastically. With improved wide area measurements and analysis techniques detecting wide area phenomena, analyzing them and eventually developing mitigation procedure that not only ensure resiliency but in some cases even improve it have become necessary.

Resiliency of a power system is an amalgamation of broad concepts like robustness, resourcefulness, rapid recovery, and adaptability. The exact implication of these concepts on power system planning and operation is subject to the characteristics of the system and also the phenomena under study. Therefore, based on these distinctive characteristics, it is important to identify the appropriate tools and techniques to assess them. In this thesis, new algorithms to analyze the wide area measurements, new models to analyze future scenarios, and new control techniques to ensure the resiliency of the system are discussed.

# Table of Contents

# List of Tables

# List of Figures

# Chapter 1

# Introduction

Electric power system is one of the largest man-made networks in the world. A reliable and efficient bulk electric system (BES) is the backbone of a thriving economy. The conditions of BES are constantly changing due to a number of factors like constantly changing load requirements, contingencies, climate, gas supply, EMP attacks, etc. In spite of these changing conditions, the balance between generation and load and operating of all the components within safe limits must be ensured at all times. Therefore, maintaining and improving the resilience of the system is a challenge. Therefore, there are a number of organizations working together to ensure the stability of the power system.

Electric Reliability Organization (ERO) Enterprise is comprised of the North American Electric Reliability Corporation (NERC) and the seven Regional Entities (REs). Their mission is to assure the effective and efficient reduction of risks to the reliability and security of the grid.[1] Recently, the Reliability Issues Steering Committee (RISC) has developed a framework to assess and maintain the resilience of the bulk energy system as shown in Fig. (1.1) (reproduced from [1]). The four outcome based resilience are included as follows:

1. Robustness: This is the ability of the system to continuously operate during contingencies, including certain low-probability events like geomagnetic events. Robustness includes development of redundant systems, inclusion of better equipment, and devising mitigation procedures to handle high impact events.

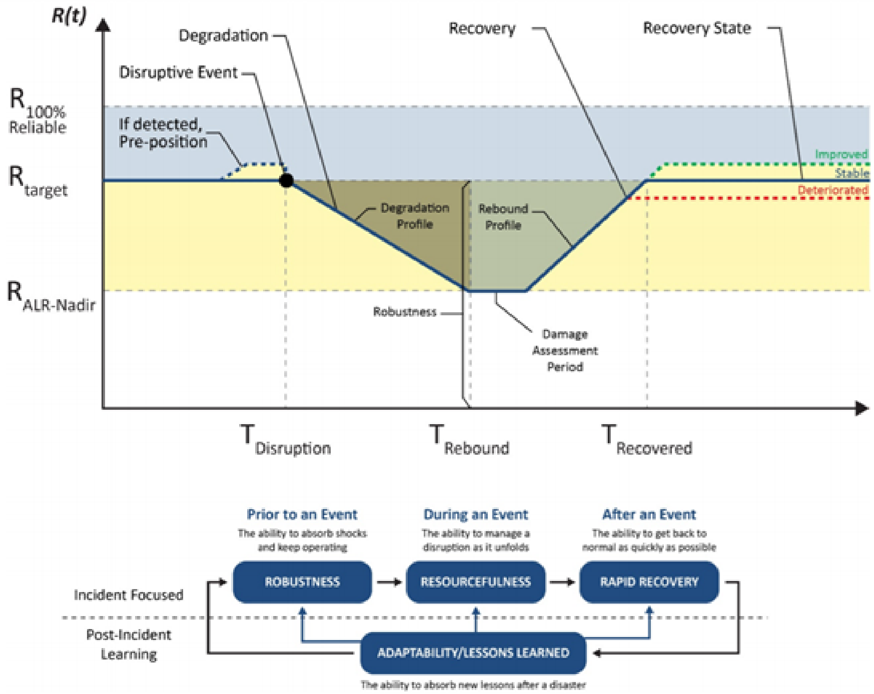


**Figure 1.1:** RISC's Model for Reliable Operation of the BPS

2. Resourcefulness: This is the ability to detect events, identify their origin, and determine the risk to the system. Resourcefulness includes using all the possible measurements, previous event analysis, and expertise of people to mitigate the situation.

3. Rapid recovery: This is the capacity of the system to return within safe operating limits by using flexible resources like high-voltage direct current (HVDC) and battery with the help of controls including wide area controls.

4. Adaptability: Considering the rapidly changing nature of the power system, adaptability is the ability of the system to be flexible and maintain the stability, which is also important from a resilience standpoint.

NERC identifies the risks to the reliability of the BPS, as well as the mitigating factors that may reduce or eliminate the reliability risk. This identification is done based on data, event analysis, and expert judgment of the staff. These sources provide a guideline for the regional entities to focus their planning, monitoring, and mitigating activities. However, the priority of these risks is identified on a continent-wide level, providing a broad guideline for each of the regional entities to focus their efforts into studying the risks that affect their region specifically.

The rate of renewable energy integration has been increasing at an unprecedented rate. In 2018 alone, around 181 GW of renewable power generation was installed. As a result, the renewable power capacity has more than doubled in the decade 2007–2018. As shown in Fig. 1.2 (reproduced from [2]), solar PV accounted for highest increase and was in fact higher than both fossil fuel and nuclear generation combined. The total renewable power capacity is currently around 2378 GW. The generation mix of the United States is shown in Fig. 1.3 (reproduced from [3]).

In the United States, the contribution of renewable energy sources other than hydro power is projected to increase to 13 percent by 2020 [3]. Around 11 GW of wind generation and around 4 GW of solar generation is predicted to come online by 2019. The annual electricity change by energy source is shown in Fig. 1.4 (reproduced from [3]).

The RISC has identified many risks to the power system. One of them is the changing generation mix, which is considered as a risk because with increased penetration of renewable energy sources, the fundamental nature of BES will change. The characteristics of renewable energy sources will have a far-reaching effect on planning, operations, and stability of the system. Some of the issues related to renewable energy sources are as follows:

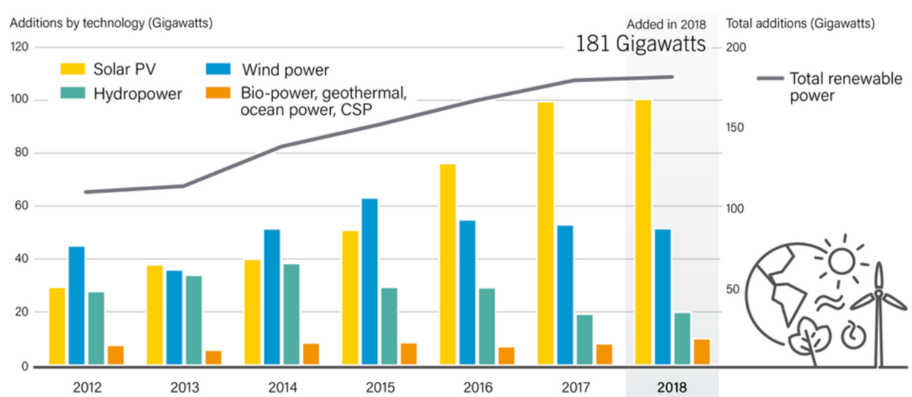


**Figure 1.2:** Annual Additions of renewable power capacity, by technology and total, 2012 2018

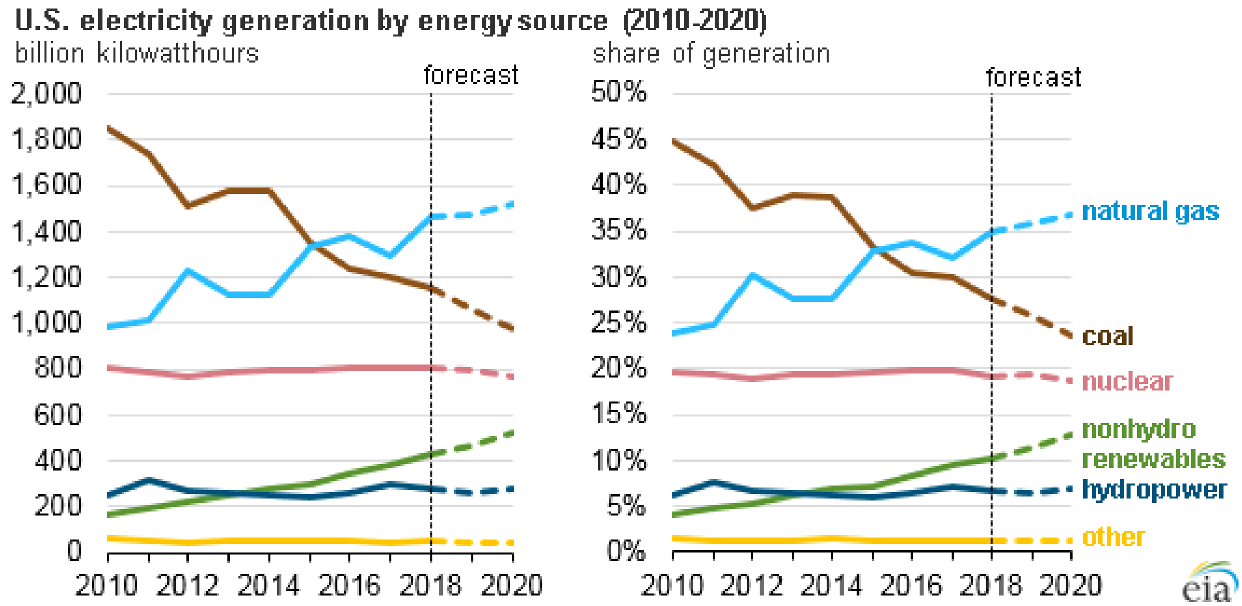


**Figure 1.3:** US electricity generation by generation source

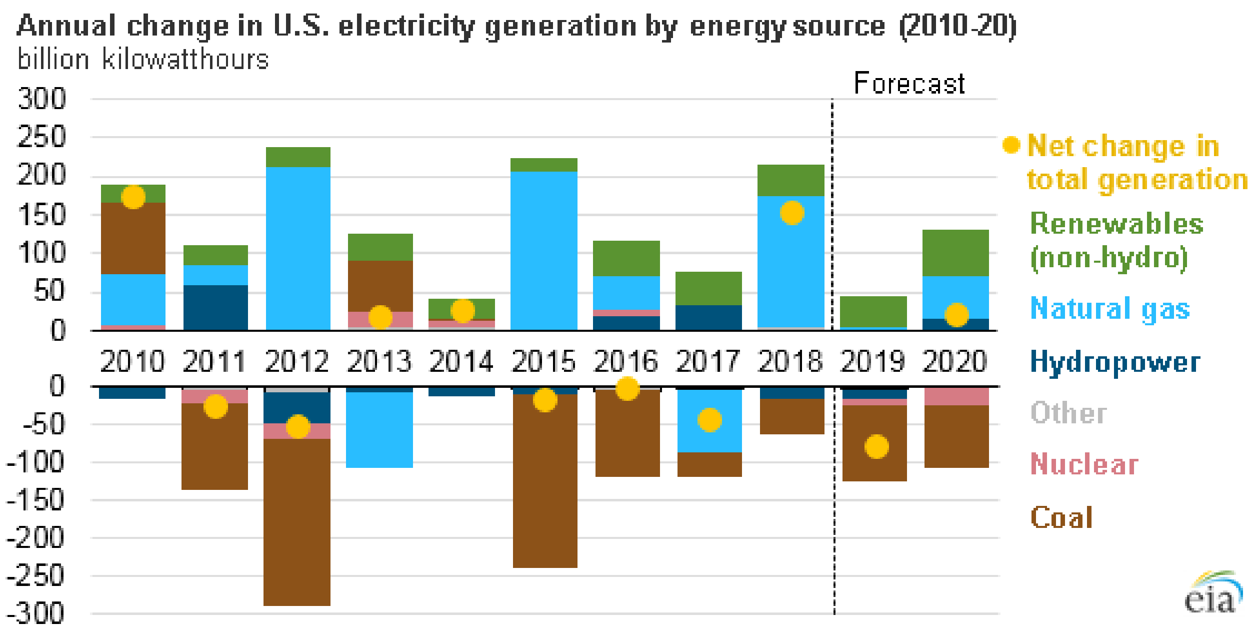


**Figure 1.4:** The annual electricity change by energy source

1. The load profile of the system will change especially with large-scale additions of rooftop solar PV. New ramping and in some cases over-generation scenarios will have to be studied.

2. There will be increased variability in the system due to the close coupling of power generation and climate. Therefore, additional resources like energy storage will have to be deployed.

3. The inertia of the entire power system will reduce due to retiring of the traditional power generators. The inherent capability of the power system to resist change will reduce and will have to be replaced.

4. The control characteristics of the inverters, including interactions between the systems, will have to be studied in detail.

In order to deal with transformation of the grid, analyzing and studying the effects of these models is important. Transient stability simulations have been one of the most widely used tools to study the stability of the system. These simulations are phasor-based time domain simulations that are used to potentially identify risks to the BES. They are also one of the primary tools used to study future scenarios and test new control strategies. Thus the main focus of this thesis is to develop models, scenarios, and algorithms to help understand the effects of the changing generation mix but also find new solutions to improve them.

Each of these interconnections has different capacities. The largest of the interconnections is the Eastern Interconnection (EI). The net generation in the EI reached almost 570 GW in the winter of 2017. The second largest interconnection in terms of generation capacity is the Western Interconnection, whose peak generation reached over 180 GW. The Quebec Interconnection generates over 33 GW predominantly from the hydroelectric dams in the area. The Texas Interconnection generates over 76 GW and has the highest penetration level of renewable energy.

As they are connected to each other only through DC ties, stability studies are performed on each of these interconnections by themselves. Over the years, there have been several models developed to study them. These planning models have to meet the standards specified by NERC. In the EI, the Multiregional Modeling Working Group (MMWG), under the oversight of the Eastern Interconnection Reliability Assessment Group (ERAG), develops models for the interconnection. Similarly there are WECC and ERCOT models. The summer peak model was the most commonly used model because the largest load amount used to be in the summer. However, the light spring model is also becoming important, especially to study the effect of increased renewable energy penetration.

These models have now been further validated based on the FNET measurements[4–6]. In [6], the importance of accurate modeling of governor dead band on the frequency response of the system was shown. In [4], the WECC and ERCOT models were also tuned for an event. Thus, apart from analyzing future scenarios, these models are essential for testing new control schemes. However, these are only a snapshot of the bulk electric system. In this work, the model is further tuned using PMU data.[7]

All of these interconnections are connected through back-to-back DC connections. They are seen to be isolated and thus are usually studied one at a time. However, there have been several proposals to connect these interconnections. The main motivation behind connecting these interconnections is to share the ancillary services among the interconnections and make power system operation more economical. As the geographical footprint of the entire system is quite large, the variation in load across the three interconnections will be more balanced. In the future, there will be a need to integrate renewable energy sources, and most them are found far away from the load centers and in the central part of the continent. Thus, it would be beneficial to study plans of better utilization.

In this dissertation, Chapter 1 deals with the generation trip estimation based on the rate of change of frequency (ROCOF) calculated from frequency disturbance recorders (FDRs). In Chapter 2, the estimation of PV generation that underwent momentary cessation is done. In Chapter 3, the influence of load model on the frequency response of the WECC system is discussed. In Chapter 4, an auxiliary controller that improves the transient stability of the WECC system using short-term overloading capability of the HVDC system is proposed and tested. In Chapter 5, the issues related to developing a North American large-scale dynamic model is discussed. In Chapter 6, the frequency sharing between the interconnections is proposed and tested. The overall conclusion and the proposed future work are discussed in the last section

# Chapter 2

# Generation Drop Estimation using FNET measurements

## 2.1 Introduction

Wide area monitoring systems (WAMS) have become a vital part of power system monitoring, operation, and control[8–10]. FNET/GridEye is one such system that has been monitoring and analyzing power systems all over the world [11] . The most important component of the system are the Frequency Disturbance Recorders (FDRs). These are the sensors that acquire GPS-synchronized frequency, voltage, and phase angle measurements at 120 V outlets (homes and work places) and transmit them via internet to the central servers. Two data centers have also been configured to receive, process, and store all the measurement data collected by these FDRs. The structure of the FNET/GridEye system is shown in Fig. 2.1 (reproduced from [10]).

Over the years, various applications have been developed using these measurements [10]. Among the applications like event visualization [12], model validation [13], historical data analysis [10], and modal analysis using ambient measurement data [14], disturbance detection and location [15] is one of the most popular applications that is currently used by many industry members including the NERC.

Applications to detect and analyze various disturbances [16] including generator trip [17], line trip [17], islanding, and oscillation detection [18] are constantly improved. Among these

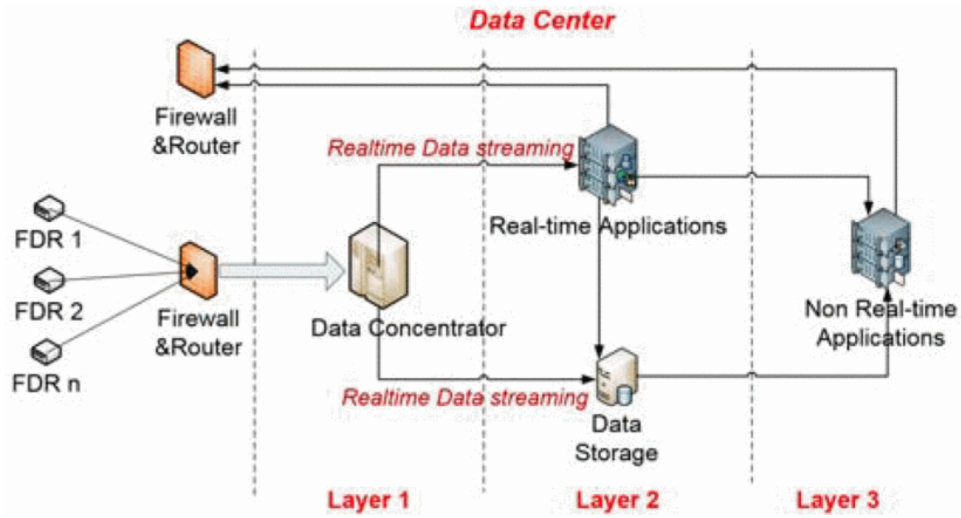


**Figure 2.1:** Multi-layer architecture of fnet/grideye data center

applications, generator trip location and estimation has received a lot of attention as it provides useful information to the operators in an interconnection. As soon as a generator trip is detected, FNET/GridEye sends an alert to all the members.

The event location application is quite accurate. However, estimation of actual generator trip amount needs to be improved. The current method uses the frequency response value and the pre-disturbance frequency and post-disturbance settling frequency to determine the total generation lost[17, 19]. However, frequency response in an interconnection is not constant and can vary significantly based on the generator headroom and load response.

Recently, there was a considerable amount of work done in [20] to improve the accuracy of the generation estimation using the rate of change of frequency (ROCOF) and also taking into account the seasonal and daily variation. This improved algorithm was even able to identify low-inertia events in the system. However, in this algorithm a single ROCOF was considered for the entire interconnection. Considering the size of these interconnections, it is not accurate to consider just the median.

Apart from the work done in the FNET lab, there have been other studies conducted to improve generation estimation based on the frequency measurements. In the context of designing an adaptive under-frequency load shedding scheme, ROCOF-based generation loss estimation has been proposed [21]. The loss has been estimated based on the swing equation and the ROCOF value at all generators. In another work conducted, [22], an analytical method to estimate the generation drop is proposed that also accounts for the reduction in system inertia due to the loss of the generation itself. In the work conducted on the Great Britain system [23], a method to estimate the system's inertia is proposed. The authors use multiple measurements and generation drop knowledge to calculate the inertia of the system.

The aim of the work discussed in this chapter is to improve the existing generator estimation algorithm for the FNET system, taking advantage of the inertia data available from the NERC. In this chapter, multiple FDR measurements, NERC regional inertia data, and Western Electricity Coordinating Council (WECC) event data are used to calculate the generation drop in the WECC system. A comparison of the methods previously used in the FNET system is done and the results are presented.

The basic stages of determining the generator lost are shown in Fig. 2.2. Each of these stages is discussed in detail in the following sections. The results of the estimation are discussed.

## 2.2 Processing of Raw FNET Data

Phasor measurements are done in each of the FDRs using a GPS signal receiver that regulates the sampling process. The basic architecture of the system is shown in Fig. 2.1. The voltage, frequency, and phase angle magnitude calculation is done based on a discrete Fourier transformation algorithm. The data is then stored in data centers after they are time stamped. Over the years, the FDR has been regularly been improved to its most current form shown in 10 data points per second are stored.

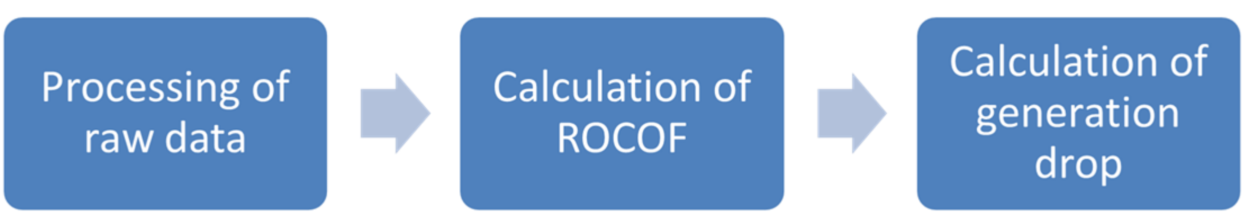


**Figure 2.2:** Stages of Calculation of Generation drop

Event detection and alerts are an important part of the FNET applications. Generation drop is one of the most commonly detected events. For active power imbalance, the thresholds are empirically determined, e.g., 3.3 mHz/sec for the Eastern Interconnection, 7 mHz/sec for the Western Interconnection. These events are stored automatically. The data plot for one of the events is shown in Fig. 2.3. A total of 10 minutes of the event is shown in Fig. 2.3. With this level of resolution, it seems like the frequency of the entire interconnection is similar. However, when the plot is zoomed in, the difference in frequency and ROCOF is evident as shown in Fig. 2.4.

When the median of the data is plotted as the black line, it is clear from the Fig. 2.4 that using the median smooths the curve and also removes some oscillations present. In order to calculate the initial frequency, nadir, and settling frequency, using the median of the frequency data seems to be adequate. ROCOF is to be calculated using the data after 0.5 s of the event, and the calculation is not straightforward.

The raw data has a lot of noise. Calculation of ROCOF based on the just the raw data will contain a lot of noise, and the oscillations of the system will also impact the ROCOF of the system. Currently the 10 data points per second are stored. Therefore, there is a need to find a compromise between ensuring the accurate ROCOF can be determined while filtering the noise. In this work, similar to the filtering technique in [24], a Butterworth filter is used

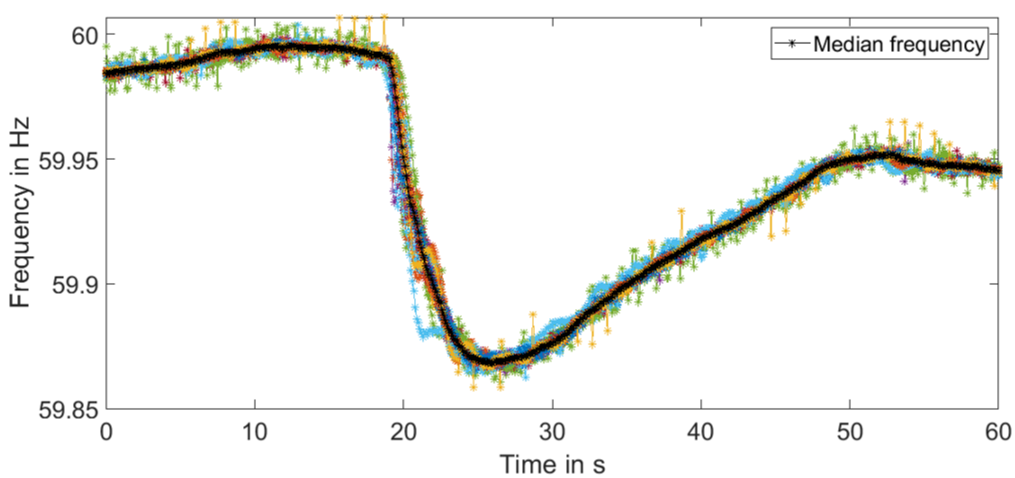


**Figure 2.3:** Generation drop event data plot

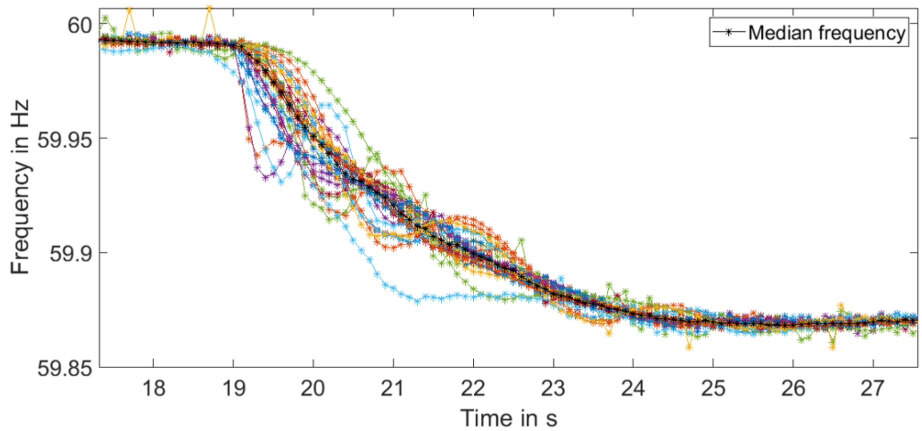


**Figure 2.4:** Generation drop event data plot (zoomed)

to remove the transients and noise from the frequency measurements. The effect of choosing the cutoff frequency on the filtered frequency value is shown in Fig. 2.5

There are over 300 FDRs around the world. In order to determine the generator drop, one of the basic approaches is to assume that the entire system is a one large synchronous machine. Therefore, using all the raw data to find a single frequency response of the entire system that ignores all the noise and oscillations of the system and provides a smooth frequency response will determine the ROCOF. This is the method that has been used in previous ROCOF-based determination [20]. In [20], the frequency of the entire interconnection is determined by using a median filter on all of the FDR measurements. This eliminates some of the oscillations as well. In this work, the center of inertia (COI) frequency of the entire system is calculated by grouping the available measurements based on the control areas of the WECC system. The COI frequency of the entire interconnection is determined based the inertia value of the regions. The comparison of these frequencies is shown in Fig. 2.6. The frequency behavior at this resolution seems equivalent. However, when zoomed in after the event as shown in Fig. 2.7, the difference is evident.

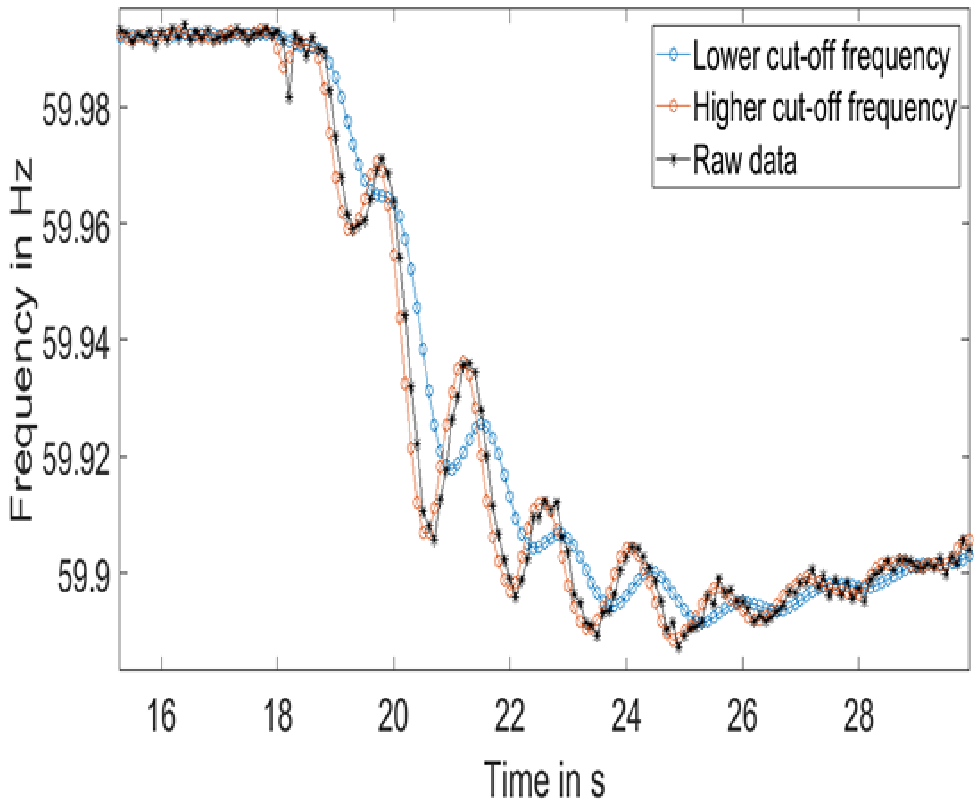


**Figure 2.5:** Effect of filtering on raw data

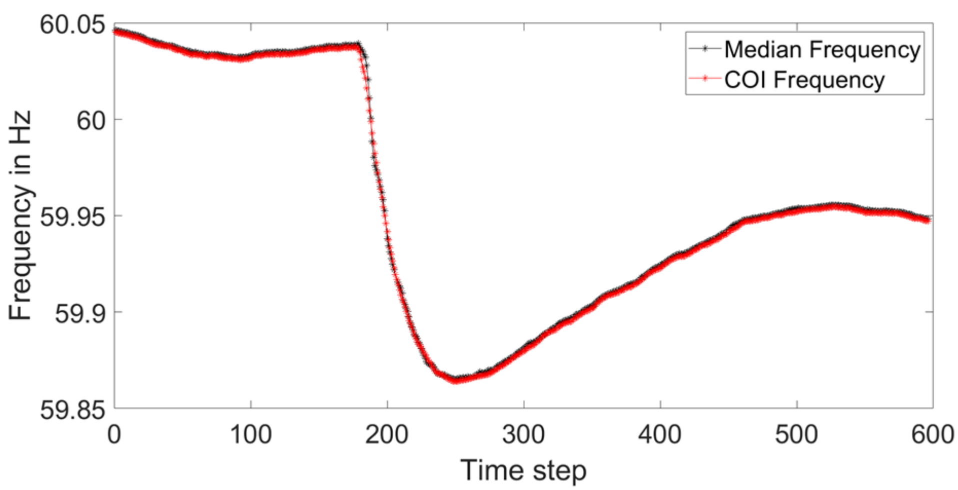


**Figure 2.6:** Comparison of the frequency measurements

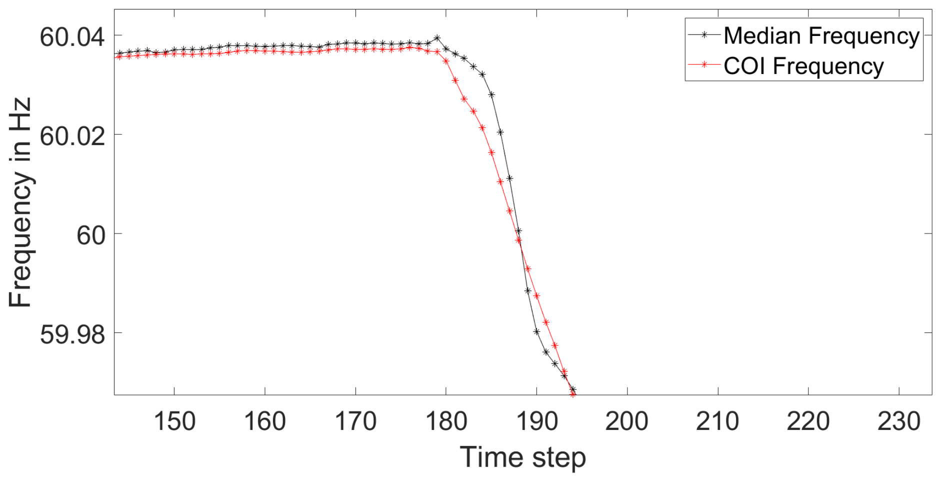


**Figure 2.7:** Comparison of the frequency measurements (zoomed)

## 2.3 Calculation of ROCOF

In the past, several ROCOF values have been employed to assess the frequency response of the system. The ROCOF based on the 3s sliding window is commonly used to determine the frequency response of the entire interconnection. This large window size will ensure that most the local oscillations are attenuated. However for calculation the generation drop based on the initial ROCOF value, three seconds window size is too large as the governor response and load response will have an impact. The other most commonly used ROCOF method is based on the sliding window of 500ms. This method has also been used to determine the generation drop. In [20], the ROCOF value with a 500 ms sliding window on the median frequency has been used to determine the generation trip amount. This method is more accurate. However, for systems like the Western Interconnection that are geographically widespread, the median ROCOF determined will be an average value as shown in Fig. 2.4 and might ignore some of the local inertial and load response.

In the current work, in order to ensure higher accuracy, the sliding window of 100ms is used to determine the ROCOF. Similar to the frequency data plot, a ROCOF plot can also be obtained. After some experimentation it was seen that using of the maximum value of the ROCOF during the event might provide the most accurate estimate of the generation lost.

## 2.4 Calculation of Generation Drop

After a generation trips in the system, there is a power imbalance in the system. This imbalance is most predominantly reflected in the frequency change of the system. A typical frequency response (reproduced from [25]) in the power system is shown in Fig. 2.8. After the generation drop, the inertial support represented by the yellow curve is almost instantaneous. During this initial period, the frequency drop seen in the system is the highest. The slope of the curve at this point is primarily dependent on the inertia of the system. The load responds to the reduction in voltage and frequency and provides some support to the system as shown by the purple curve. However, the frequency decline is arrested at point C after the governors start responding. The governor response as shown by the blue curve is delayed due to the dead band and the inherent time delays present in the system. Therefore, even after the frequency stops declining, the governors keep providing additional support, eventually leading to the frequency settling. At this stage, the inertial support reduces to zero and the load and governor response are the only factors affecting the settled frequency.

In this chapter, two methods are discussed based on the primary frequency response to calculate the generation drop. The first method involves the calculation of generation drop based on the governor response and the difference in frequency before the event and frequency when it is settled after the event. This method is simpler of the methods as only the

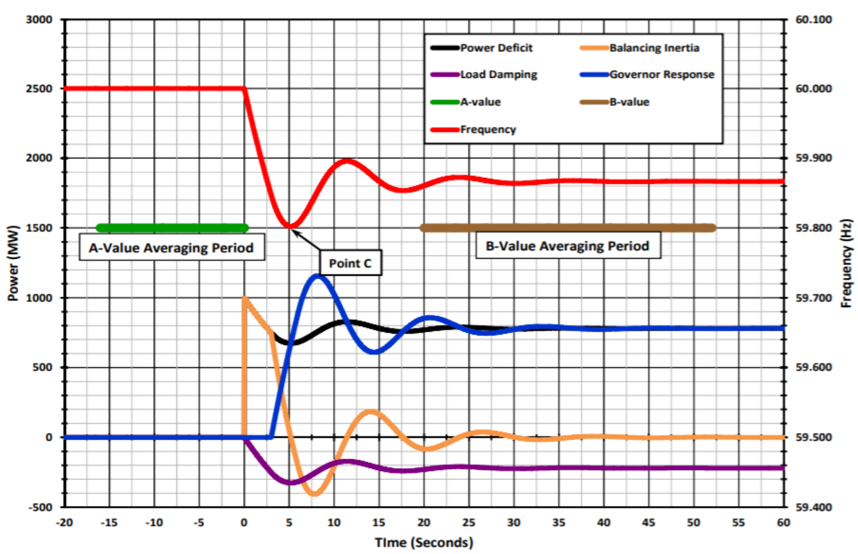


**Figure 2.8:** Primary frequency response

calculation of the average frequency measurements is needed. Considering the large number of FDRs available, there will be a lot of redundancies in the calculation, thus ensuring higher reliability.

The primary response of the system constantly changes. Therefore, using only the initial inertial response to calculate the generation lost will be more accurate. With increased penetration of renewable energy sources and their variable and fast response, it may be useful to use the ROCOF-based methods. Among this method, two alternatives based on the mean ROCOF value and the COI ROCOF value are also discussed and compared.

### 2.4.1 Using the governor response values to calculate generation trip

In this method, the generator trip amount is calculated based on the governor response. As shown in the Fig. 2.8, in order to estimate the generator trip amount, the effect of inertial response has to reach zero. Therefore, the change in frequency needs to be calculated after the frequency has stabilized. Assuming, the governors control the real power output of the generators based on the frequency change in the system. The change in power generation with change in frequency for a single generator is shown in 2.1.

$$\Delta p^m = \Delta p^{ref} - \frac{1}{R}\Delta f \tag{2.1}$$

where $\Delta$ f is the change in frequency, $\Delta p^m$ is the change in turbine mechanical power output, and $\Delta p^{ref}$ is the change in a reference power setting. R is called the regulation constant. For an entire area, the aggregate governor response can be determined as shown in 2.2

$$\begin{aligned} \Delta p^m_{sys} &= \Delta p^{ref}_{sys} - \beta \Delta f \\ \Delta p^m_{sys} &= \textstyle\sum_{li=0}^{n} \Delta p^m_i, \Delta p^e_{sys} = \sum_{li=0}^{n} \Delta p^e_i, \beta = \sum_{li=0}^{n} \frac{1}{R_i} \end{aligned} \tag{2.2}$$

where $\beta$ is called the frequency response of the interconnection. This value is determined using past events [17]. During the period of study, if $p^{ref}$ is assumed to be constant, then the change in power can be determined based on the change in frequency. The change in frequency is calculated based on the average frequency before the event and the settled frequency after the event. The pre-event frequency is calculated by averaging 4 seconds of data before the event. The post-event frequency is calculated by averaging frequency data after 5–9 seconds after the event. This is the method that has been implemented in the FNET system. This method is computationally simple and fast to implement in real time. The averaging of frequency signal reduces the noise. Considering only the median frequency is to be determined, the large number of FDRs provides the much-needed redundancies. However, the generation loss determination based on these equations does not consider the load response or the change in inertia of the system. The frequency response of the system itself changes constantly, which does not produce the most accurate results. This method is also ineffective to determine the generation drop for the inverter-based events like momentary cessation.

### 2.4.2 Using ROCOF and total inertia

The swing equation for a synchronous machine that governs the relationship between the real power imbalance and frequency change is shown in following equation:

$$\frac{2H}{\omega_0}\frac{d\omega(t)}{dt} = P^m - P^e \tag{2.3}$$

The $H$ constant shown in the above system represents the inertia of the machine; however, an interconnection consists of several machines and loads. The aggregate model of the entire system can be constructed as follows:

$$\frac{2H_{sys}}{\omega_0}\frac{d\omega\hat{(t)}}{dt} = P^m_{sys} - P^e_{sys} \tag{2.4}$$

$H_{sys} = \sum_{li=0}^{n} H_i, P^m_{sys} = \sum_{li=0}^{n} P^m_i, P^e_{sys} = \sum_{li=0}^{n} P^e_i$

This equation is valid during the initial transition of the system before governors are activated and loads provide support. Therefore, in theory, using the ROCOF of the system during the initial stages, the amount of generation drop could be determined. This involves processing the raw data to ensure that noise and small oscillations are ignored. ROCOF-based estimation of the generation method described in [20] assumes that the entire interconnection is one large system and the frequency response of the system is found by applying a median filter on all of the FDR measurements. The ROCOF is then calculated based on the 0.5 s time difference. This method was useful in determining the low inertia events that have become more common with increased penetration of renewable energy sources. However, the actual inertial value has not been used in this method.

The inertia of the entire system constantly changes during the year as shown in Fig. 2.9. Using the same inertia value of the system for all the event analysis might introduce errors. Therefore, in this work, the inertia value as given by the NERC was used to improve the accuracy of the generation loss estimation.

There will be a change in inertia distribution as well. The generation distribution, load distribution, and even the climate of the Western Interconnection vary widely during the year. Therefore, it might be important to consider different inertia distribution based on the seasonal changes in the load. In this work, the inertia distribution based on the different areas is obtained from the NERC and used appropriately based on the timing of the event.

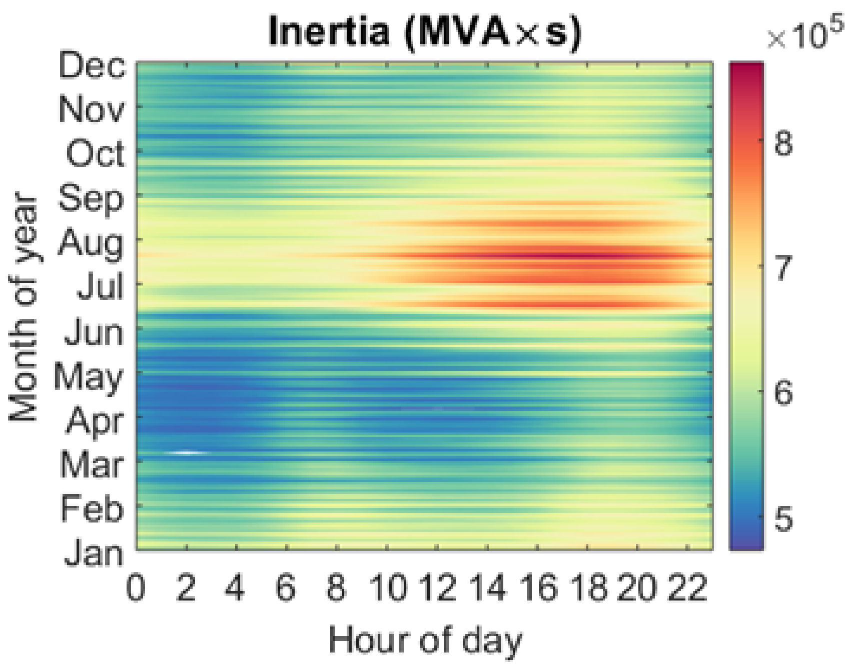


**Figure 2.9:** Inertia distribution during the year

### 2.4.3 Using ROCOF and regional inertia values

One of the shortcomings of the previous method is the assumption that the entire interconnection is a single system. This assumption is not accurate when the system is as large as the Western interconnection. As can be seen, the frequency measurements at different FDRs are quite varied. The median value ignores the regional inertia distribution of the system.

Theoretically, the most accurate method of determining the generation lost[21] is to use the frequency change measurements at all the generators and use their individual inertia to calculate the generator lost. However, for a system like WECC with over 2500 generators, this method is not practical. Therefore, a better method is to use the regional characteristics of the different control areas of the system to calculate the COI frequency. One such work was previously conducted in [24].

COI frequency of the system is determined as follows:

$$\frac{2H_1}{\omega_0}\frac{d\omega_1(t)}{dt} + \frac{2H_1}{\omega_0}\frac{d\omega_n(t)}{dt} + ... + \frac{2H_n}{\omega_0}\frac{d\omega_n(t)}{dt} = P^m - P^e \tag{2.5}$$

where $H_1$, $H_2$, $H_3$ are the inertias of the different control areas of the system. These control areas are based on the actual control areas present in the WECC system.

## 2.5 Results

The generation trip events in the Western Interconnection during 2018 are studied in detail. Around 30 generation events are analyzed in the Western Interconnection. The accuracy of the methods is checked with actual generator drop value as reported to the NERC. The inertia of the WECC system present during these events is also used to determine the actual value of the generation lost. The frequency response method is based on the governor response of the entire system and ignores the inertial change, load response of the frequency. This is the method that is currently used in the FNET system to determine the generation lost. The second method is based on using the median frequency measurement and also the ROCOF calculation based on a 0.5 s sliding window to determine the final generation drop. The

COI-based generation drop calculation is used to determine the frequency drop and finally it was seen that when the average of the COI-based generation and the FNET method is used. The accuracy of the methods is depicted in Fig. 2.10

For these generator drops, it is seen that COI-based generation estimation is the most accurate. However, the amount of data required in terms of COI-based generation is quite large. Even though there over 30 FDRs in the WECC region, their distribution is not uniform. Thus, there are cases when the FDR data is not available for the entire regions. In those cases, the effect of the area is ignored.

The ROCOF-based methods are very sensitive to oscillations. If there are a lot of oscillations, the error in calculation of the generator loss is quite high. In those cases, the traditional frequency response–based methods are more efficient. There needs to be a compromise between these situations. Thus, the average method that uses both frequency response and ROCOF method is also studied. It has been seen that even though the error for this method is higher than the seasonal COI case, it is able to handle oscillations better.

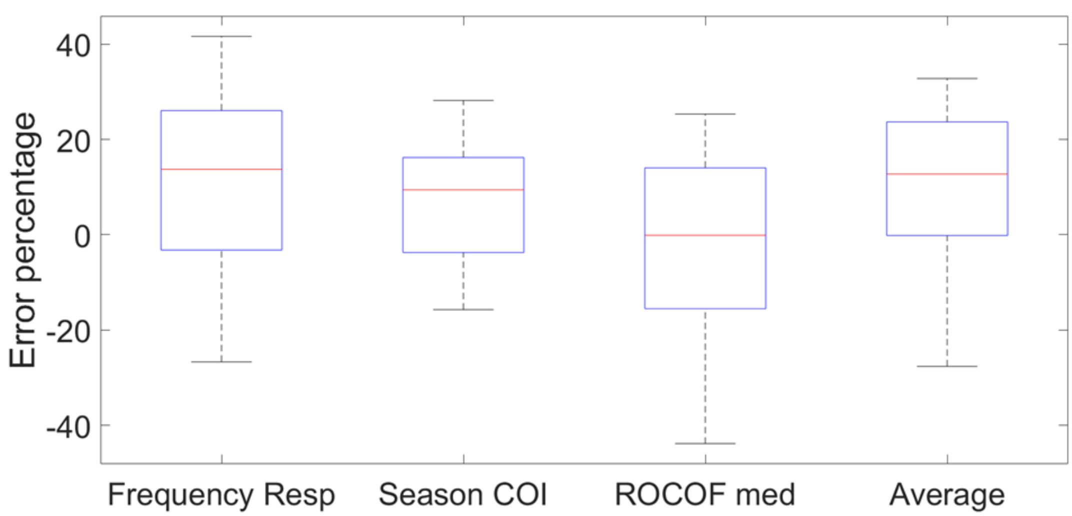


**Figure 2.10:** Comparison of the accuracy of generation loss estimation algorithms

## 2.6 Conclusion

In this chapter, the COI frequency–based method to calculate the generation trip amount has been discussed. Real data from FNET has been used to calculate the generation trip amount. This method has been compared with other methods that have been previously used. The COI-based method shows improvement over previous methods, but its accuracy also depends on obtaining accurate inertia values and ensuring that at least one FDR is active in all of the control areas. In the future, the load response of the system will also have to be taken into account in order to obtain even more accurate results.

As discussed in [26], the use of frequency and ROCOF-based methods to calculate the generator drop has quite a few drawbacks. For the most accurate determination of the generator drop, the frequency measurement from each generator will have to be obtained. The real-time information about the inertia of the system will have to be obtained. It has been our experience as well as other researchers' that the noise in the ROCOF calculation is quite high and will have an impact on the final generation estimation. In the future, methods related to machine learning will probably yield more accurate results.

# Chapter 3

# Estimating the PV Systems that Experienced Momentary Cessation

## 3.1 Introduction

The phenomenon where the inverter temporarily ceases to inject active and reactive current ("zero current injection") into the point of connection with the grid is termed momentary cessation. The inverter remains connected to the grid. An illustration of this phenomenon is shown in Fig. 3.1.

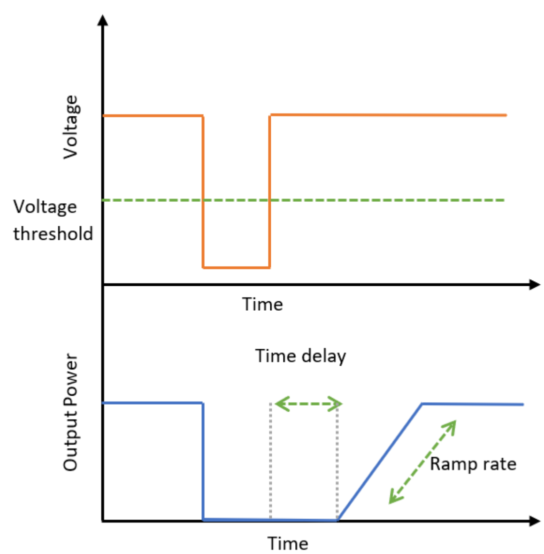


**Figure 3.1:** Momentary cessation

Momentary cessation is triggered when the terminal voltage is beyond a pre-specified bandwidth. The generator stops injecting power and, after a time delay, generator output is ramped up at a constant rate. This voltage threshold, time delay, and ramping rate vary across manufacturers [27–29]. This phenomenon was first noticed during the Blue Cut Fire in 2016 when, after a fault, a large number of PV generators entered into momentary cessation, causing a significant dip in the frequency of the entire Western Interconnection. This event was not isolated; several such events have been recorded as shown in Table 3.1.

After a thorough investigation, the reason behind momentary cessation was determined as follows:

- Incorrect frequency measurement: It has been observed that immediately following a fault, there are jumps in the phase angles. These phase angle jumps cause erroneous frequency measurements in inverters. The measurements are interpreted as being beyond the safe working region, which eventually initiates momentary cessation. This characteristic of the inverter was first identified in 2016 and the generator operators were notified to resolve this issue by either adding filters or introducing a delay in their inverters. Since then, the frequency measurement–based momentary cessation has been resolved in most of the inverters.

- Voltage dip– or spike–based trigger: The other reason the inverters undergo momentary cessation is that inverters have been built to enter momentary cessations when the voltages go beyond a predefined threshold. This has been used in many of the

**Table 3.1:** Summary of the momentary cessation events recorded

| Events | Fault | PV loss estimated SCADA | Lowest frequency |
|---|---|---|---|
| Blue cut fire (16 Aug 2016) | 13 500 kV line faults in SCE, 2 287 kV line faults in LADWP | 1200 MW | 59.867 |
| Canyon fire (9 Oct 2017) | 2 faults near Serrano | 632 MW | 58.878 |
| April 20 2018 | LL fault | 1110 | 59.85 |
| May 11 2018 | LL fault | 900 | 59.877 |

inverters primarily due to the incorrect interpretation of the standard PRC-024-12 [30]. This region was previously interpreted as a must-trip zone, but was intended to be interpreted as may-trip zone. The standard has been illustrated in Fig. 3.2 (reproduced from [31]). It has been seen that a large percentage of the inverter manufacturers cease the output.

Even though the new inverter resources that will be added will not undergo momentary cessation and it is now currently not considered as a threat, accurate modeling of these resources was important for planning studies during the time the issue was not resolved. A survey by the NERC showed that among the inverter units (as shown in Fig. 3.3, reproduced from [31]), around 11,821 units will cease output during abnormal voltages. The data suggests that in theory around 14,113 MW injection could potentially enter momentary cessation and have a large-scale impact on the bulk electric system. However, parameters like voltage threshold, ramping rate, and time delay vary across manufacturers. To study their effects on the BES, these PV generators would have to be modeled accurately.

One of the major issues is that the default parameters used in current models do not reflect specific field settings of PV plants. For that reason, momentary cessation was not noticed in generation integration studies or subsequent operation studies. Some of the recommended models like *REEC_B* and PVG1, PVE1 are not sufficient to model the momentary cessation

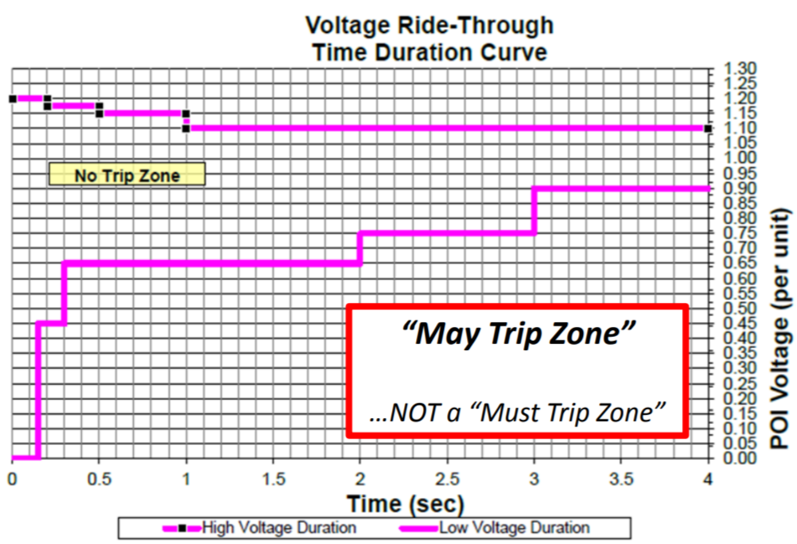


**Figure 3.2:** Revised Voltage Ride through time duration curve

| Inverter cease output during abnormal voltages? | | | |
|---|---|---|---|
| | MW | Responses | Inverter units |
| Yes | 14,113 | 119 | 11,821 |
| No | 2,657 | 31 | 2,557 |
| **Total** | **16,771** | **150** | **14,378** |

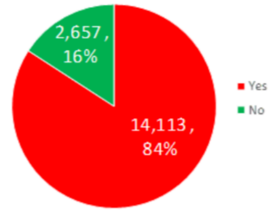


**Figure 3.3:** Survey of the inverters that cease output during abnormal voltages

accurately [32, 33]. Therefore, initially, user-defined models are included in addition to these models to simulate momentary cessation behavior. Recently, $REEC\_A$ and $REGC\_A$ have been used successfully to model momentary cessation and study its impact on the grid.

In one study [34], the impact of momentary cessation on the large-scale grid is seen to be severe for some conditions. It is shown that the transient behavior of the system changes significantly for different voltage thresholds and recovery time delays. It is seen that for a few contingencies and a time delay of 0.5s, the grid could even become unstable [34]. During one of the momentary cessation events, the power flow through the California-Oregon Interface changed drastically as shown in Fig. 3.4 (reproduced from [35]).

Another study conducted by CAISO revealed that there could be significant impact on the power flow on the California-Oregon Interface [35]. The focus of both these studies was to study the worst-case impact of momentary cessation. Hence, similar values are used across the converters. In reality, the values of the time delay and ramp rates vary significantly. In order to determine their actual impact, it is important to ensure that each of them is modeled accurately. It is of crucial importance to improve modeling of inverter-based resources (PV plants specifically) to be able to accurately evaluate impact of momentary cessation on the reliability of interconnection.

It is also a known fact that there were several solar units in the distribution system that went into momentary cessation. However, considering they were solar rooftop units, it was seen as a spike in load. Therefore, it might not be sufficient to model all the generators in the system accurately. The change in solar power generation in the distributed system will also have to be taken into account to completely understand the effects of momentary cessation on the system.

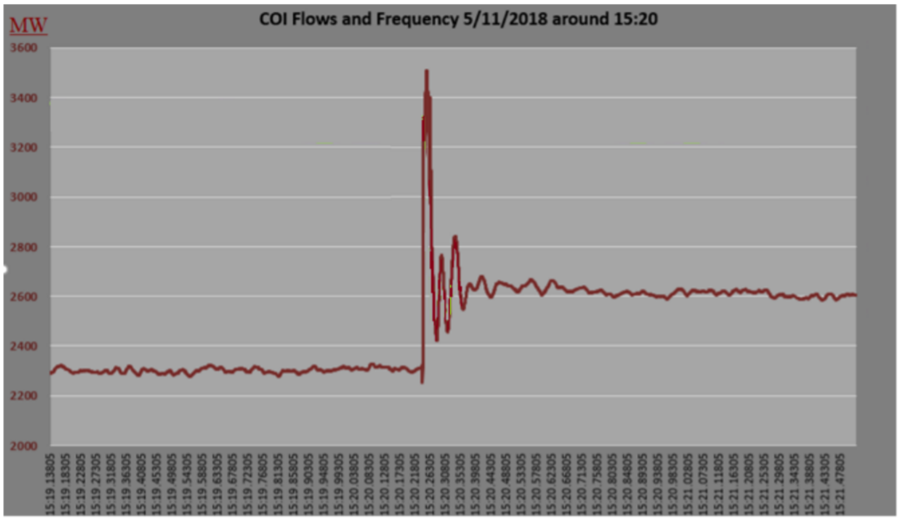


**Figure 3.4:** Effect of momentary cessation on the power flow of the California-Oregon Interface

The initial work involves tuning the models currently available to accurately represent the behavior of the PV system. Tuning is performed based on a real-life event and high-resolution measurements (Digital Fault Recorders, DFRs). Considering that recorded data from a small set of PV plants were available, multiple PV plants, including the ones at the distribution level, were particularly challenging to tune. For their tuning, we used PMUs available from transmission buses. These PMUs allowed estimation of the total MW reduction amount. Later, FNET data and the generator loss estimation methods are used to independently determine the PV generator loss that might have happened. In this work, an event from April 2018 is studied.

## 3.2 Modeling of Momentary Cessation

The PV generator model in power system simulation software must have the following properties as mentioned in [29]:

1. The model should be able to inject zero current for the specified time period when the voltage at the terminal goes beyond the user-defined threshold.

2. The model should be able to ramp up to the pre-fault levels of power injection at the ramp rate that can be specified.

3. The models should have independent real and reactive current control.

4. The model should be able to restrict the reactive power injection during the fault condition.

### 3.2.1 Basic Structure of PV Generators

Over the years, several generic models have been developed for converter-based generators that are used for transient stability, voltage stability, and frequency stability studies of the BES [29]. Specifically, for PV systems, the overall structure of the model used is shown in Fig. 3.5 (reproduced from [29]).

The three main components of the model are:

1. *REPC_A*: This is the plant controller and is responsible for the plant level control of real and reactive power output. It provides real and reactive power command to the current controller. For the purposes of the current study of momentary cessation, the *REPC_A* model is not necessary and has not been used.

2. *REEC_A* or *REEC_B*: This provides the active and reactive current command to the current injection models. This current command is determined by the reference power command, current limiters, and user-defined priority. It has the capability of injecting or restricting current during a fault condition specified by the user.

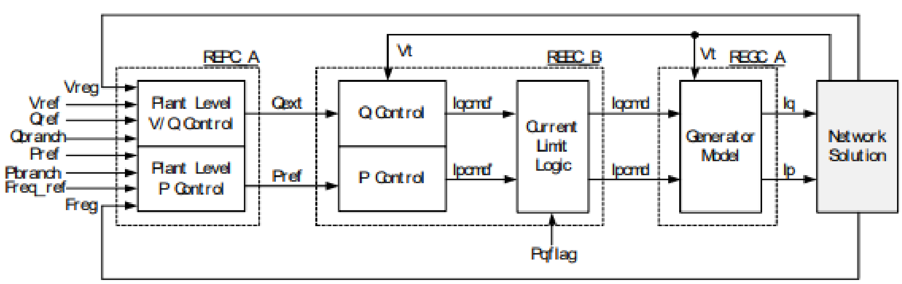


**Figure 3.5:** Basic structure of PV generator model

3. *REGC_A*: This is the interface between the grid and the controller. It is a high-bandwidth current regulator that injects real and reactive components of inverter current into the external network. It has the ability to control the ramping rates of current.

NERC recommends that the momentary cessation be modeled using the *REGC_A* and *REEC_A* models. The voltage threshold and time delay are modeled using *REEC_A* model and the ramp rate is modeled using *REGC_A* model. The parameters can be modified as follows:

1. Voltage threshold: The voltage threshold is modeled using the *REEC_A* model. Two sets of piece-wise relationship can be defined for the real and reactive current limiter using the *VDL1* and *VDL2* respectively. Four points can be defined to represent the relationship between the voltage and maximum current rating. Thus, by setting the current to zero when the voltage is lower than the threshold, triggering of momentary cessation can be simulated.

2. Time delay: The *REEC_A* model is designed such that the current output can be frozen for a time delay specified by the user given by the quantity called *thdl2*.

3. Ramp rate: The ramp rate is modeled with *REGC_A* model. Real power ramping is specified using the *rrpwr* quantity. This *rrpwr* quantity is specified in pu on the machine base.The reactive power ramping can be specified using *iqrmax* and *iqrmin*. However, in this simulation, the reactive power was kept constant.

## 3.3 System Description and Methodology

A frequency drop event that was attributed to the momentary cessation was observed on April 20, 2018. There was a line-to-line fault on a major 500 kV line in California. The fault was cleared in less than 4 cycles (Fig. 3.6). In spite of the short fault-clearing time, many of the PV plants entered into momentary cessation mode, resulting in significant frequency drop in the WECC system. The frequency dropped to almost 59.87 Hz (Fig. 3.7). This drop indicated a generation loss of about 1100 MW. CAISO and PG&E reported a drop in

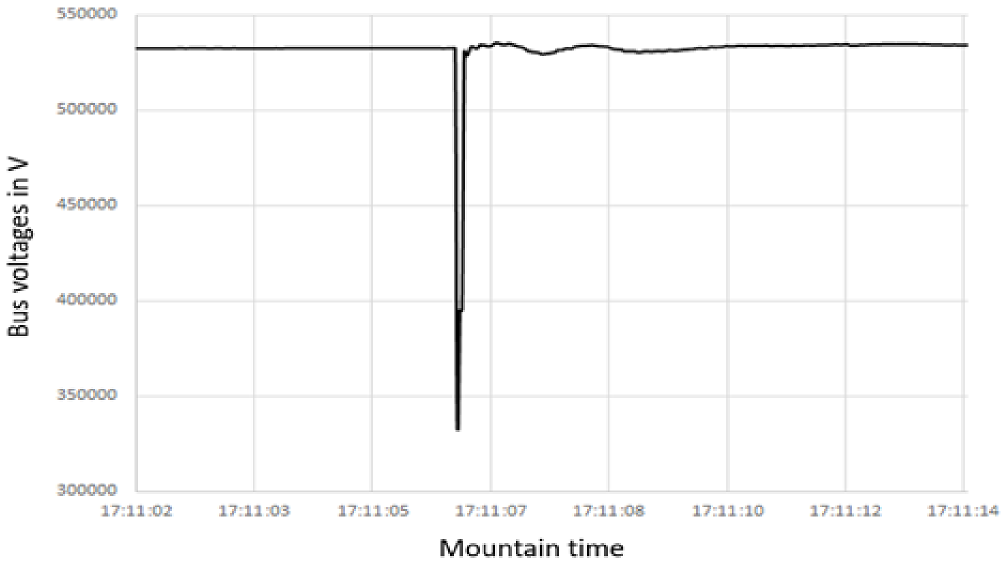


**Figure 3.6:** Voltage dip during the April 20, 2018 event

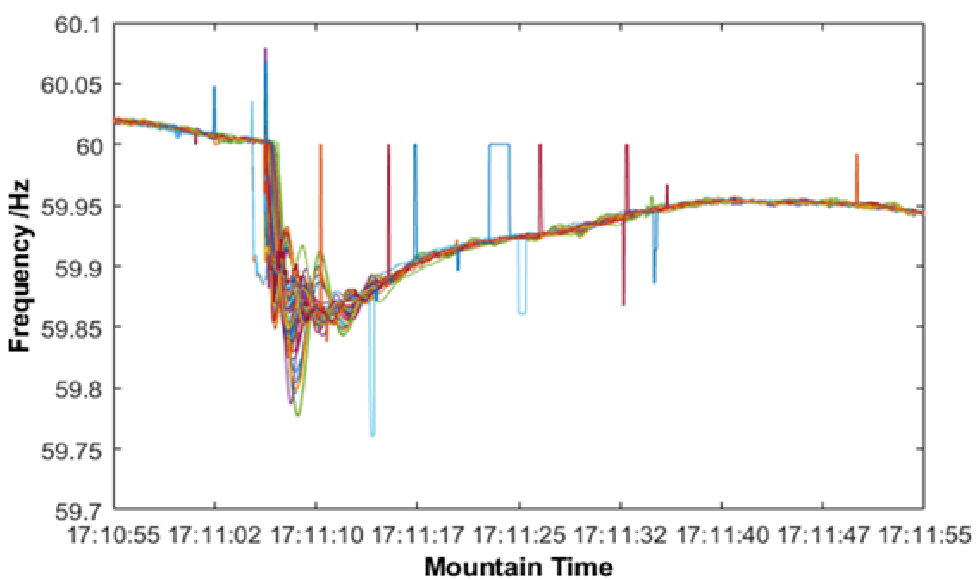


**Figure 3.7:** Frequency response during the April 20, 2018 event

PV generation. However, drop in PV generation in residential inverters was also observed, though there is no accurate method of determining the total number.

Data from SCADA, which is collected every 10 s, indicated that a total of 600 MW of PV generation dropped after the event. In order to capture momentary cessation accurately, a more precise data set was needed. The DFR recordings at several PV plants are used. The data is collected 30 times a second. This data is not available at all PV plants' points of connection. Therefore, it might not be possible to replicate the exact frequency response of the system. It is also almost impossible to accurately represent plants behind meters. Therefore, PMU data available at various locations on major transmission buses is used to further improve other PV plant models so that the measured and simulated values match as much as possible. This approach allows us to estimate the actual power drop due to PV plants entering into the momentary cessation mode, including the ones in the distribution system. The simulation is done using the TSAT software and the WSM model. The base case is a bus-branch model with 16,000 buses and 20,000 branches (dynamic) and 3,800 generating units. The PV generators are modeled using the REECA and REGCA models. The archived case used is the case recorded just prior to the event. The fault is applied using the details given in the NERC event report

## 3.4 Results

Initially, the default parameters for modeling momentary cessation that are used are as follows: voltage threshold of 0.9 pu, time delay of 0s, and ramp rate of 10 pu/s. The response is shown in Fig. 3.8 and Fig. 3.9. There is very little impact of momentary cessation on the frequency response. Another simulation with time delay of 10s is done, and the response is shown in Figs. 3.10 and 3.11. Frequency drops to 59.6 Hz. The large difference in the impact of momentary cessation between the two simulations clearly illustrates the need for accurate modeling parameters for simulation studies.

In order to accurately model momentary cessation, each PV plant is individually tuned to replicate the event recording from the DFRs. Two such generators are discussed in detail. DFR measurements are obtained from entities for several generators. The final tuned models

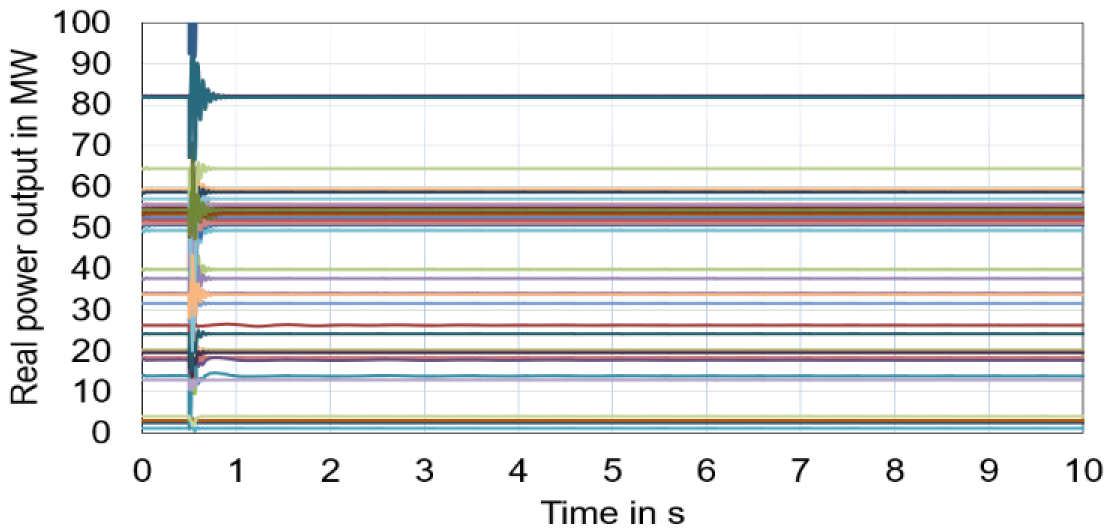


**Figure 3.8:** PV plants output in MW using default parameters during the April 20, 2018 event

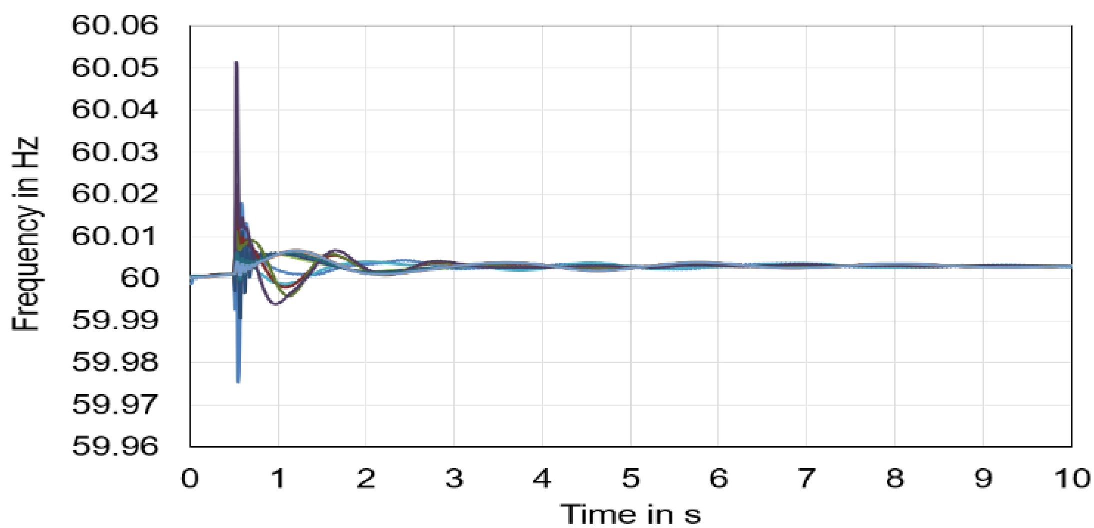


**Figure 3.9:** Frequency response using default parameters during the April 20, 2018 event

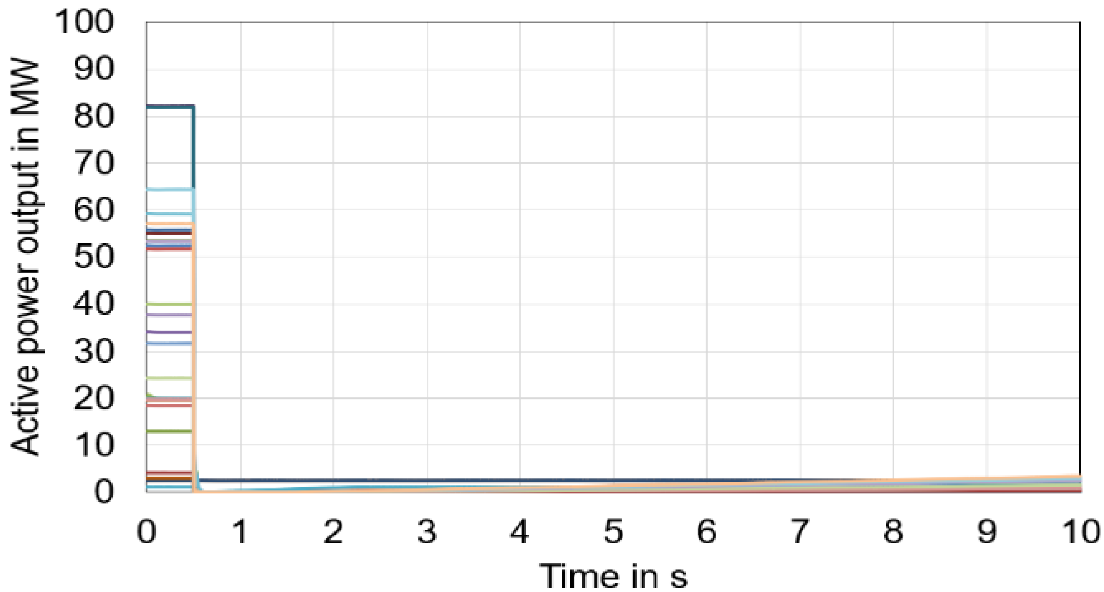


**Figure 3.10:** PV plants output in MW (simulation) using a time delay of 10 seconds during the April 20, 2018 event.

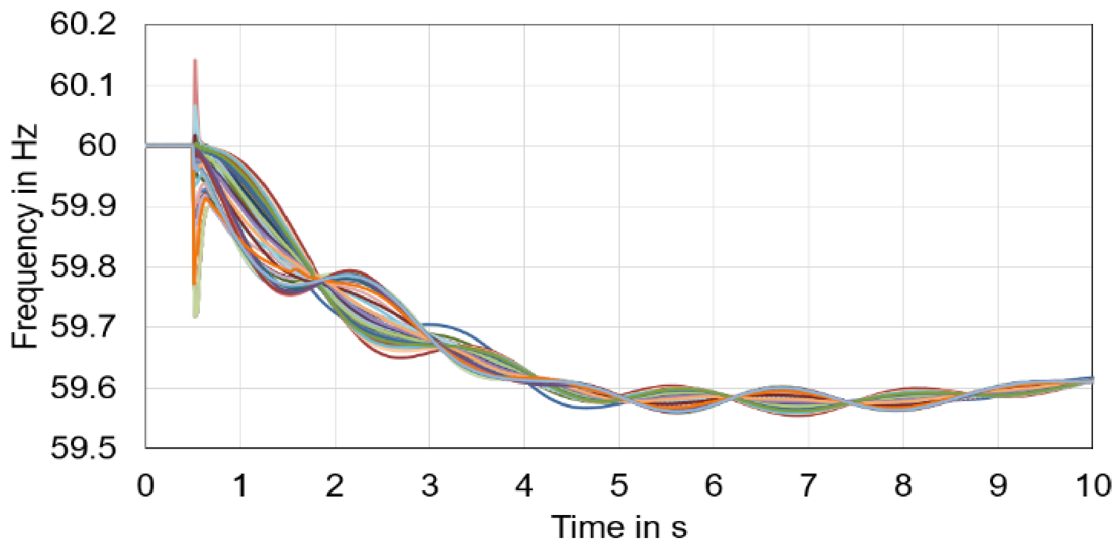


**Figure 3.11:** Frequency response using a time delay of 10 seconds during the April 20, 2018 event

of the PV generators are shown in Figs. 3.12, 3.13. Parameters used are given in Table 3.2. It is easy to see from the DFR measurements of generator 1 3.12 that there is no time delay and the ramp rate is uniform. As shown in Fig. 3.13, the response of generator 2 is not straightforward. In reality, there might have been multiple inverters with different responses. The models usually used for stability are aggregated models. Generator 2 is split into four individual generators 2a, 2b, 2c, and 2d to replicate the behavior accurately.

The power outputs of these generators 2a, 2b, 2c, and 2d are 125MW, 25 MW, 25 MW, and 100 MW respectively. Generator 2c does not undergo momentary cessation; hence, it is not switched. Generator 2d is disconnected completely after the fault to replicate the reduction in generation. The Generators 2a and 2b undergo momentary cessation, and the parameters used to replicate their behavior are given in Table 3.2. Several other PV generators whose DFR measurements were available are also tuned. The total response measured in these PV generators and their simulated values are shown in Fig. 3.14. Based on these DFR measurements, it is clear that there was a reduction of almost 1500 MW momentarily, and generators producing 500 MW of power remained disconnected.

Using these available measurements, the generators are tuned. As not all measurements were available at all PV stations and several PV generators connected to the distribution system might have entered momentary cessation and there is no method of measuring them, PMU measurements available at certain buses the event is used to determine if the total amount of PV systems that went into momentary cessation.

The comparison of the PMU measurements from a few specified buses and the simulated frequency at the same buses are compared in Figs. 3.15, 3.16, 3.17, and 3.18. It is clear that the frequency response of the simulated system is similar to the measured values. The total generation loss for this case is shown in Fig. 3.19. A total of 900 MW of generators remained disconnected even after 10s. However, there was a reduction of almost 4000 MW momentarily.

**Table 3.2:** Parameters used for tuning PV generators

| Quantity | Generator 1 | Generator 2a | Generator 2b |
|---|---|---|---|
| Power (MW) | 105 | 125 | 25 |
| Time delay (s) | 0 | 0.5 | 0.5 |
| Low voltage (pu) threshold | 0.9 | 0.9 | 0.9 |
| Real power (pu/s) ramp rate | 2.0 | 0.4 | 10.0 |

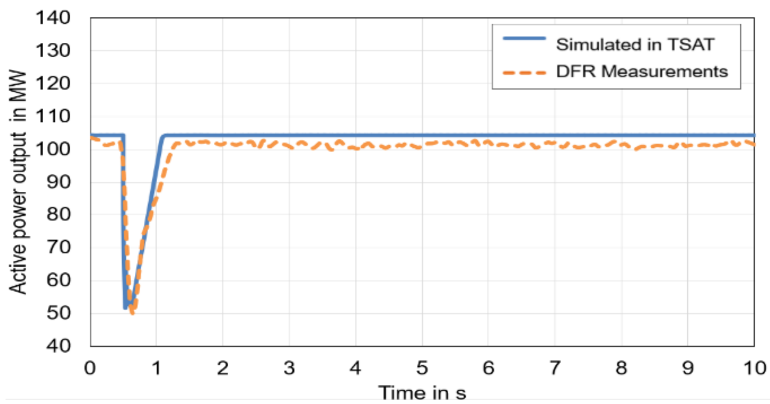


**Figure 3.12:** Comparison of real power response of PV generator 1 with DFR measurements

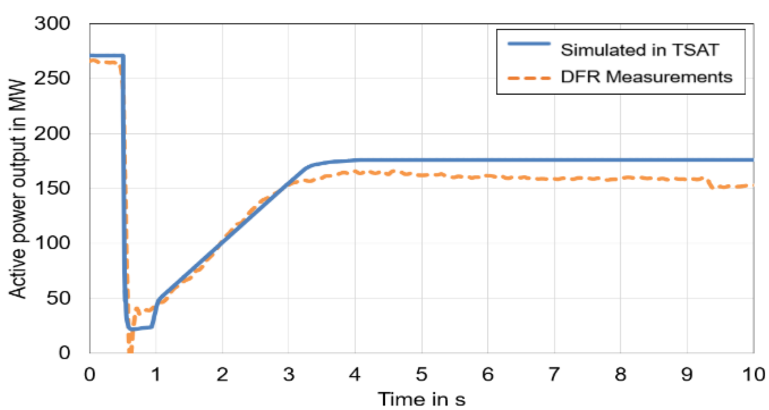


**Figure 3.13:** Comparison of real power response in PV generator 2 with DFR measurements

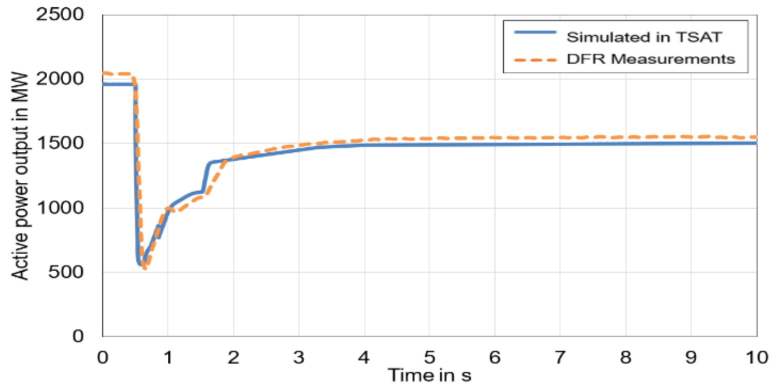


**Figure 3.14:** Comparison of real power response of all PV generators with DFR measurements

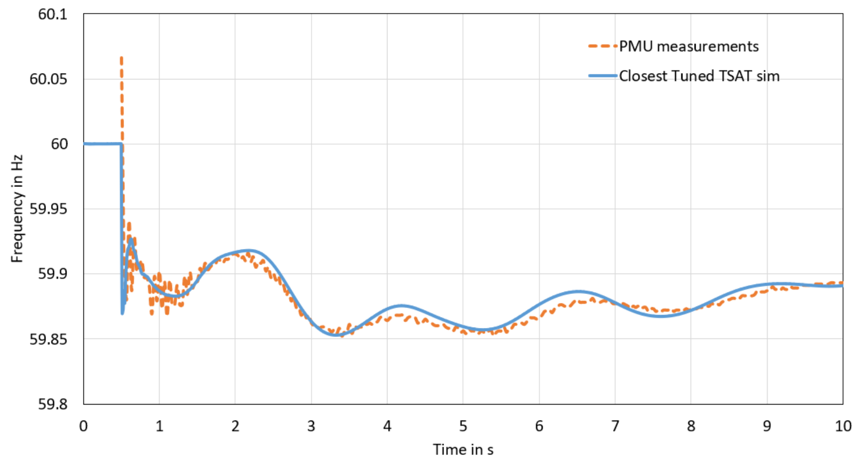


**Figure 3.15:** Comparison of PMU measurements and TSAT simulation at bus 1

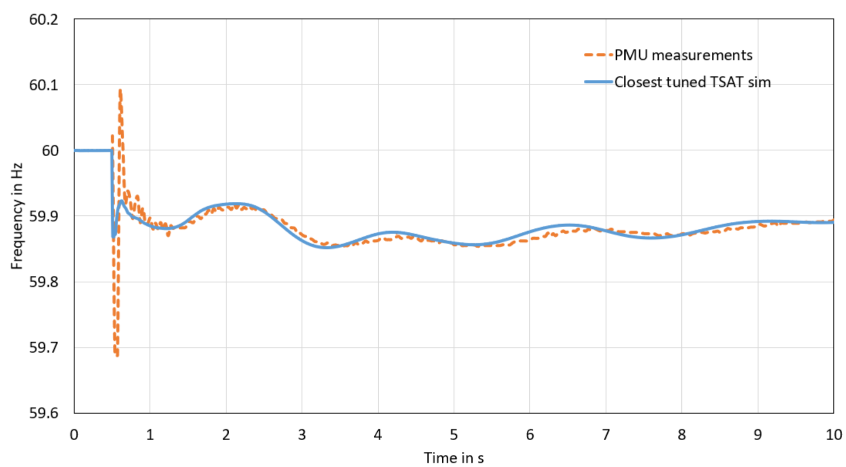


**Figure 3.16:** Comparison of PMU measurements and TSAT simulation at bus 2

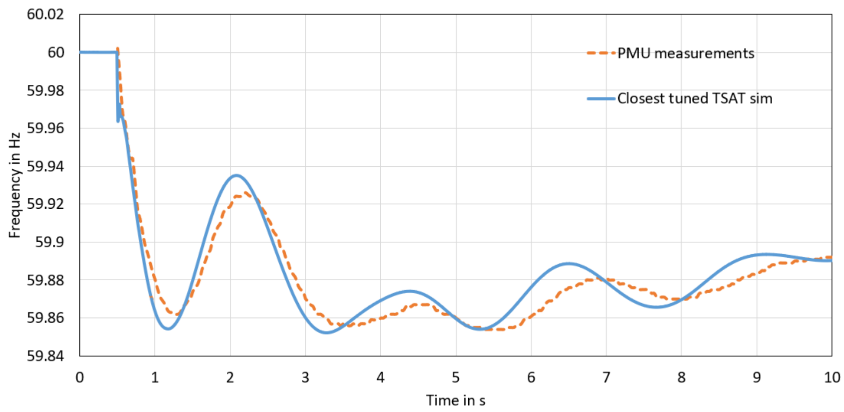


**Figure 3.17:** Comparison of PMU measurements and TSAT simulation at bus 3

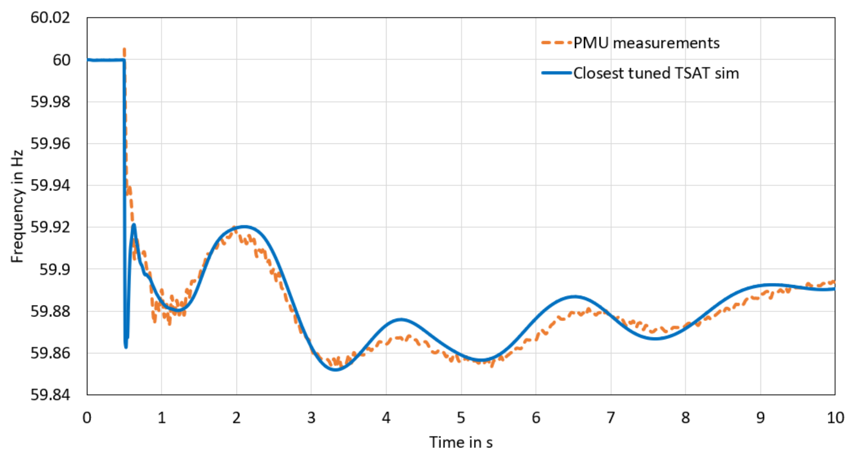


**Figure 3.18:** Comparison of PMU measurements and TSAT simulation at bus 4

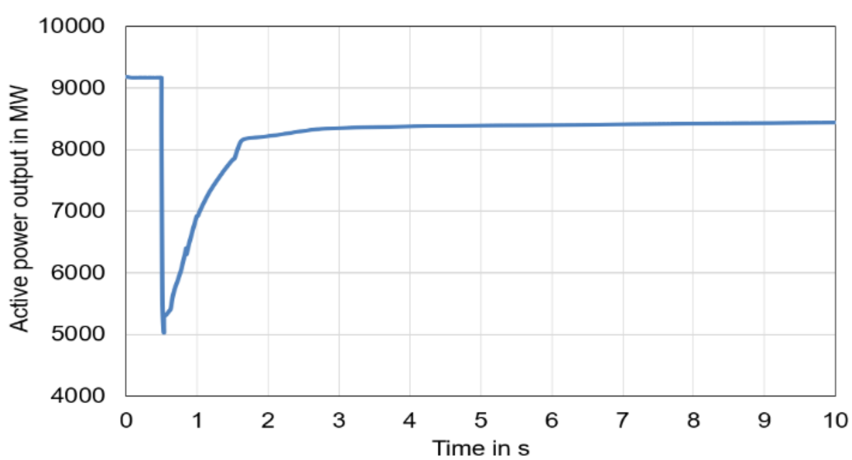


**Figure 3.19:** Total PV generation loss during momentary cessation with tuned parameters

## 3.5 Estimation of PV Generation Lost During Momentary Cessation

Several methods have been developed in the previous chapter to estimate the generation lost using FNET data. Each of these methods has some advantages and some disadvantages. The method currently used in the FNET system uses the difference in frequency value before the event, the settling frequency after the event, and the frequency response value to calculate the generation trip amount. This method is based on the assumption that the generator tripped will remain disconnected for the entire time period of this transition. However, for the specific scenario of determining the PV generators that undergo momentary cessation, a lot of PV generators are back online within a couple of seconds. Thus, this momentary loss of PV generators cannot be estimated accurately using the traditional method. This is clear from Fig. 3.20 where a momentary cessation event and another generation drop event with similar settling frequencies have been plotted together. The initial higher ROCOF clearly indicates that the PV generators experiencing momentary cessation were much more than the initial estimation of 790 MW.

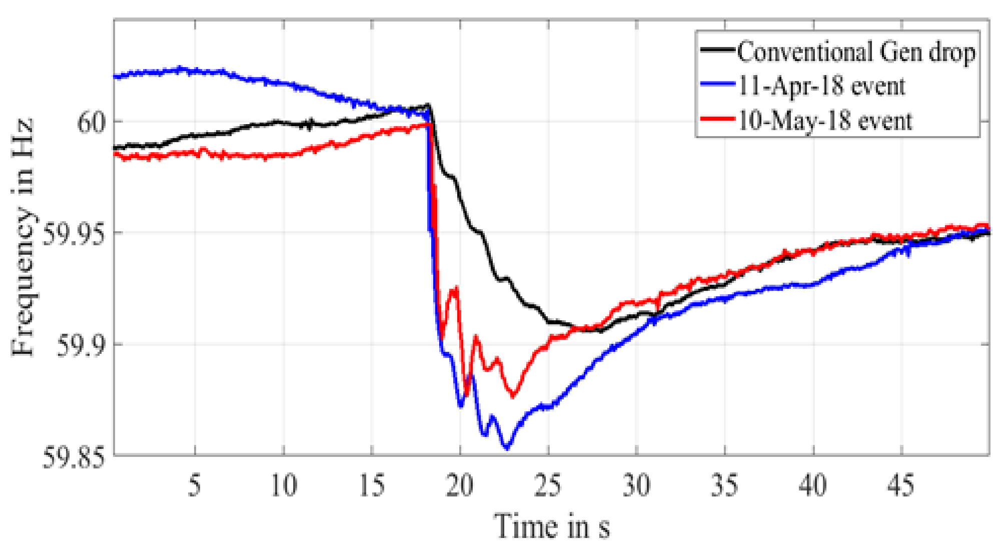


**Figure 3.20:** Comparison of frequency response of momentary cessation event and a conventional generator loss

As there is direct correlation between ROCOF and the generation lost, around 217 events are analyzed and ROCOF is calculated. For these events, the generation lost was confirmed by the NERC. These generation loss events also included two confirmed momentary cessation loss events on April 20 and May 11. Based on the the ROCOF of the other generation lost, the generation lost during momentary cessation can be estimated by using the linear fit curve function present in MATLAB toolbox. This linear fit is shown by the red curve in Fig. 3.21. This is a simplistic method that is used to calculate the generation lost during momentary cessation. From Fig. 3.21 it is clear that the generation lost as estimated by traditional method was clearly inaccurate, so the ROCOF-based method has to be used to determine the actual generation lost.

Finally, based on the methods from the previous chapter and inertia data from the NERC, the PV generation that experienced momentary cessation has also been calculated. The values calculated by all these methods are shown in Table 3.3. The estimated generation lost during momentary cessation is shown to be closer to 3671 MW.

## 3.6 Conclusion

In this work, the momentary cessation phenomenon observed in PV generators is studied in detail. The frequency response of a real-life event is replicated in the TSAT simulation

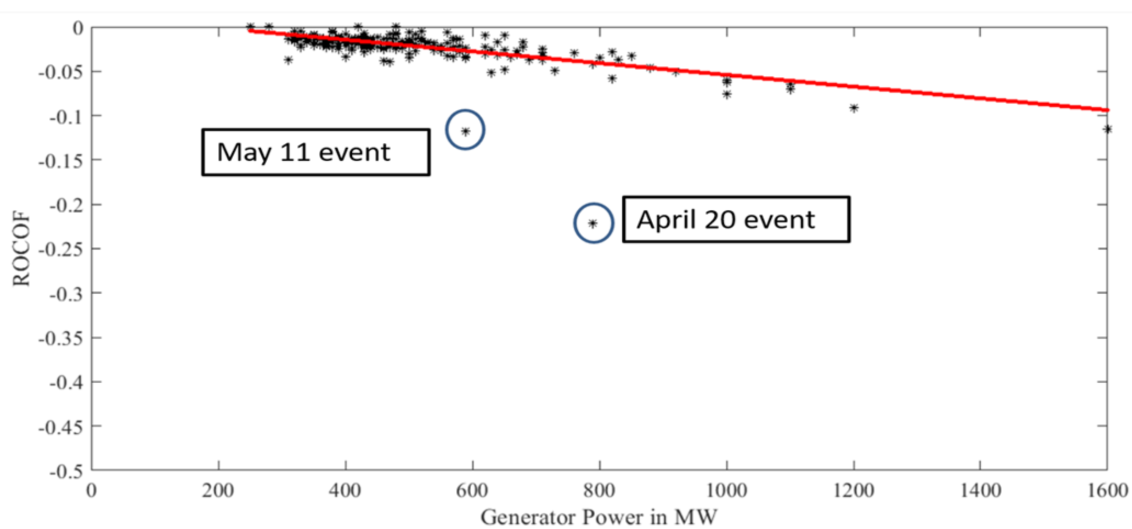


**Figure 3.21:** Comparison of ROCOF of all generation loss events

**Table 3.3:** PV momentary cessation estimation

| Method | MW estimated Apr20 |
|---|---|
| Frequency response method | 790 |
| Mean frequency method | 3130 |
| COI frequency method | 3671 |

software. DFR and SCADA data of several generators are used to tune the PV generator models in the simulation software. The simulation results showed that the total power output of the PV generators that might have entered momentary cessation was closer to 4000 MW. Algorithms developed in the previous chapter and the FNET data were used to estimate the generation lost during momentary cessation. It was estimated that the generation lost during momentary cessation was closer to 3600 MW, which came close to the values obtained using the simulation tools.

In the past year, there have been several notifications given by the NERC that specify the new standard that reduces the momentary cessation phenomenon. It has been seen that this phenomenon is probably not a threat anymore. Detailed composite models that include the distributed generation in the load are now currently being used to model the momentary cessation in solar rooftop units. Thus, even though momentary cessation was seen as a high-impact event during 2016 and 2017, steps have been taken to resolve this issue.

# Chapter 4

# Minimum Frequency Response Reserve Requirement for WECC

## 4.1 Introduction

A primary focus of power system operators around the world is ensuring continuous active power balance. The power system is constantly in flux: the load is constantly changing and thus the system generation must be changed accordingly to ensure the active power balance and maintain the frequency close to the nominal levels (60Hz in North America).[36]

There is a need to have additional resources online that can not only provide support to the system in case of contingencies but also help balance the load during normal day-to-day operations and compensate for the inherent variability of the renewable energy sources [37]. The amount of the additional resources required is determined based on the ability of the system to stabilize the frequency after an imbalance (like generation or load loss). In North America, FERC has established a frequency response and frequency bias setting reliability standard BAL-003-1-2 [38, 39] that specifies the amount of frequency response required in each interconnection.

Each of the interconnections has interconnection frequency response obligation (IFRO). This IFRO is determined based on the largest N-2 events identified in each interconnection, also known as Resources Loss Protection Criteria (RLPC)[40]. For the WECC system the criterion is N-2 Palo Verde generation trip, which amounts to a loss of 2700 MW. As specified in BAL-003-1-1, the IFRO in each interconnection should be sufficient that it should not activate under-frequency load shedding (UFLS). For the WECC system, the UFLS limit starts at 59.5 Hz. The performance of each of the interconnections is calculated based on frequency response measure. Frequency response measure specified by the NERC is based on the load of generation loss amount and the difference between average frequency calculated prior to the event and the average settling frequency calculated after the event.

The primary frequency response of a system basically consists of the following responses:

1. Inertial response due to the kinetic energy stored in the rotating masses of the generators.

2. The governor response due the action of governors, which respond to change in frequency.

3. Load response, which is due to the reduction in load due to a reduction in frequency.

Basically inertial response of the system is determined by the number of generators synchronized to the system that can provide inertial support. This is determined by the type of generators and the number of generators online. In the future, with many generators retiring, the loss of inertial response is of concern. One such study conducted by [41] showed that there was a deteriorating trend in their frequency response during 2012–2016. They identified the main cause of this trend as increased renewable penetration.

The load response is due to the nature and the amount of load connected to the system. Currently, when there is an active power imbalance, the load responds to support the system frequency. This is also due to the dependence of the load on the frequency value. However, in the future with more inverter interfaced controls, the load response could decline.

Both of the above responses are inherent characteristics of the system and in most systems cannot be actively controlled. The basic control for the operator to ensure frequency stability is the governor response. The governors should respond to provide enough frequency response that the frequency stabilizes before the secondary control like AGC responds. Thus, it is important to study the minimum frequency response required when the other two conditions vary. In this chapter, the effect of inertia, load response, and governor response on the WECC interconnection is studied. The minimum frequency responses for different inertial and load conditions are presented.

In several studies conducted on the three interconnections [4, 5], future scenarios with large amounts of renewable energy have been developed and analyzed to determine the frequency response. The focus of these studies was studying the effect of reduction on the inertia. The impact of load damping has not been studied because the focus of this work was to determine the worst-case scenario, and assuming no load response usually provides the most pessimistic response.

In this work, the effect of inertial response, governor response, and load response on the frequency response is studied. Then the variation of minimum frequency response with inertia is determined for the high summer case after the base case is validated using FNET measurements.

## 4.2 Factors that Affect the Frequency Response

### 4.2.1 Governor Response

The governors are responsible for changing the mechanical power input of the generators when there is a deviation in the frequency. Every interconnection must have sufficient governor response to ensure that the UFLS limit is not reached for RLPC. Depending on the type of generator and available headroom the governor response is varied among the models. The active power generation headroom data from the model provides some insight regarding the available headroom for increasing the power output of the system. The generators with governors that respond to frequency change are modeled in the power flow with the base load flag as zero. Other generators have governors but do not have their frequency response reserve enabled. Thus, only the frequency-responsive generators provide the additional support to stabilize frequency.

In this work, the effect of governor response on frequency stability is studied by changing the amount of frequency response reserves.

### 4.2.2 Load Response

The dynamic response of load has a significant impact on the overall response of the entire system. It is essential to model them accurately. However, there are many challenges to modeling load including lack of information regarding load composition, variability in load composition, and lack of parameters [42]. Over the years several load models have been developed based on measurements or components. Load models are classified into three broad categories: static load, dynamic load, and composite load.

- Static load model: Static loads are dependent on the magnitude of voltage and frequency of the bus. They are usually resistive loads or a simplification of other loads like motor loads. They have been extensively used in the past as they are simpler to model and the effect of change in voltage and frequency in the load can be represented. Among the static loads, the most commonly used model is the ZIP model, which represents basically the constant impedance, constant current, and constant power portion of the model. These coefficients are determined based on the measurements.

- Dynamic load model: Dynamic load models depend on both voltage and time. These models are usually comprised of detailed motor loads that are able to model the dynamic behavior of the motor in detail. This is particularly important in voltage stability studies where the voltage recovery may be affected by the motor characteristics.

- Composite load model: The composite load model consists of a combination of the static load and the motor loads. These provide the most accurate response to disturbances in the system. Several versions of these models have been developed over the years. One of the most intricate models currently being in used in the WECC system is the WECC composite load model. Here the WECC composite model is described in detail.

This composite load model was developed after the 1996 Western North America blackouts. Insufficient load modeling was determined as the primary reason for not identifying the reliability issue. The current model has 132 constants that need to be defined based on the composition of the load. This model is available from all the major dynamic power system studies software. The basic components of this model are shown in Fig. 4.1 (reproduced from [43]). There are four different motors in the model to represent four kinds of motors:

- Motor A: three-phase, constant-torque compressors used in air conditioning and refrigeration
- Motor B: three-phase higher inertia fans whose torque is proportional to speed squared
- Motor C: three-phase lower inertia pumps whose torque is proportional to speed squared
- Motor D: single-phase compressors, often used in residential air conditioning

With California's decision to meet 50% of its energy requirements with renewable resources by 2030, the rate of penetration of inverter-based generators is expected to continuously increase for the next decade. This year, CAISO reported that utility-scale solar generation reached 10,521 MW [44] and this data does include at least 5000 MW of solar generation behind the meters in distribution systems. It is therefore obvious that the

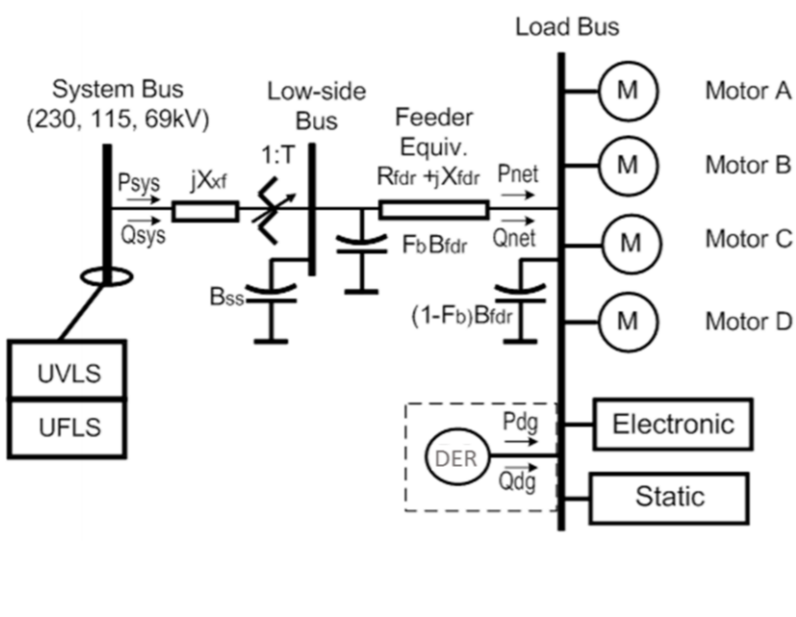


**Figure 4.1:** Composite load model

dynamics of these inverter-based generators will significantly impact BES. The distributed energy resources including rooftop PV are also being represented in the system after the momentary cessation events in 2016. Static load models present in the system represent the characteristics of the aggregate loads. Step-down transformers, feeders, and shunts are also represented in this model.

### 4.2.3 Inertial response

Inertial response of the system is due to the kinetic energy stored in the rotating masses of the synchronous machine. When there is a power imbalance, the inertial response of the system is the first to respond and directly affects the rate of change of frequency and nadir. This inertial response depends on the total number of conventional synchronous machines online. In the future, with a large number of replacements of conventional generators with inverter-based resources, the reduction in inertial response will affect the frequency response of the system. There are two methods of creating the scenarios with reduced inertia. The first method is straightforward. The inertia of the entire system is synthetically reduced by changing the inertia constant of the machines. The other, more realistic scenario is the replacement of generators with PV generators. This scenario will involve developing new dynamic cases with PV models instead of the conventional generator models. Currently, in this work, inertia of the generators has been reduced synthetically by a factor.

## 4.3 Development of Models with Different Inertias in PSLF

This study is conducted using the 2019 high summer case of the WECC model. This case represents the conditions with heavy flows from Northwest to California and also peak loads. Some salient details of the model relevant to the studies are given in the Table 4.1.

In this simulation, the composite load models present in the base case have all been retained. As the purpose of this study is not to study the worst-case scenario, the contribution of the composite models to frequency response of the system is also taken

**Table 4.1:** Significant details of 2019 model

| | |
|---|---|
| No. of buses | 22503 |
| No. generators | 4280 |
| Total P gen (MW) | 178780 |
| No of load loads | 14271 |
| Total P load (MW) | 172835 |
| Total frequency responsive real power headroom present | 14 931 MW |
| Total Inertia base case | 1,137,000 MVA-s |

into consideration. The inertia levels of the synchronous generators are changed to represent the change in inertia. The headroom present in the generators is also varied to study the frequency response of the system with curtailed headroom. According to the interconnection criteria, the largest N-2 contingency is the loss of two generators at the Palo Verde plant, resulting in a total loss of 2750 MW. The UFLS limit in WECC is considered to be 59.5 Hz.

- Inertia change: The effect of change of inertia is studied by reducing the inertia constant at all the online generators.

- Governor response: The effect of change of governor response is done by disabling the governors at all the generators that are online, have active power headroom, and respond to change in frequency

- Load response: Apart from the composite load model already present in the base case, another scenario with 80% constant P and 20% constant Y is created to demonstrate the behavior of the system with non-responsive loads

- Finally, the minimum frequency response reserve is determined by first tuning the base case using FNET measurements and then varying the inertia and calculating the minimum FRR.

## 4.4 Results

Initially, the effect of governor headroom is studied. The inertia and the load response are not changed from the base case. Five cases with different levels of headroom are studied. These are the five cases:

- Case 1: 100% headroom intact (Base case)
- Case 2: 75% headroom intact
- Case 3: 50% headroom intact
- Case 4: 25% headroom intact
- Case 5: 0% headroom intact (No governor response)

The frequency response with inertia level of 100 is shown in Fig. 4.2. It is seen that with increasing headroom the settling frequency and nadir increase. However, ROCOF remained the same. The change in settling frequency is primarily due to the change in governor response of the generators as shown in Fig. 4.3. Simultaneously, as shown in Fig. 4.4, the loads present in the system also respond to change in frequency to stabilize the system.

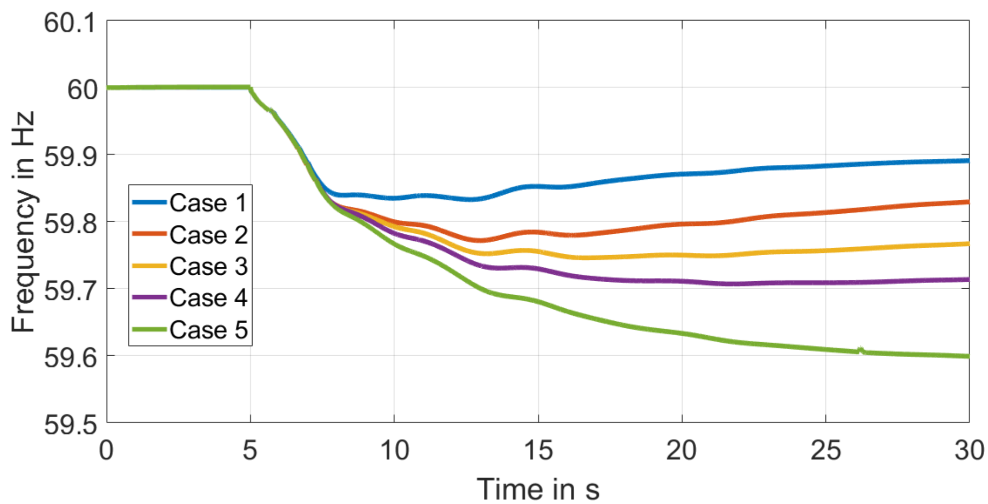


**Figure 4.2:** Change in frequency response of the system with generator headroom

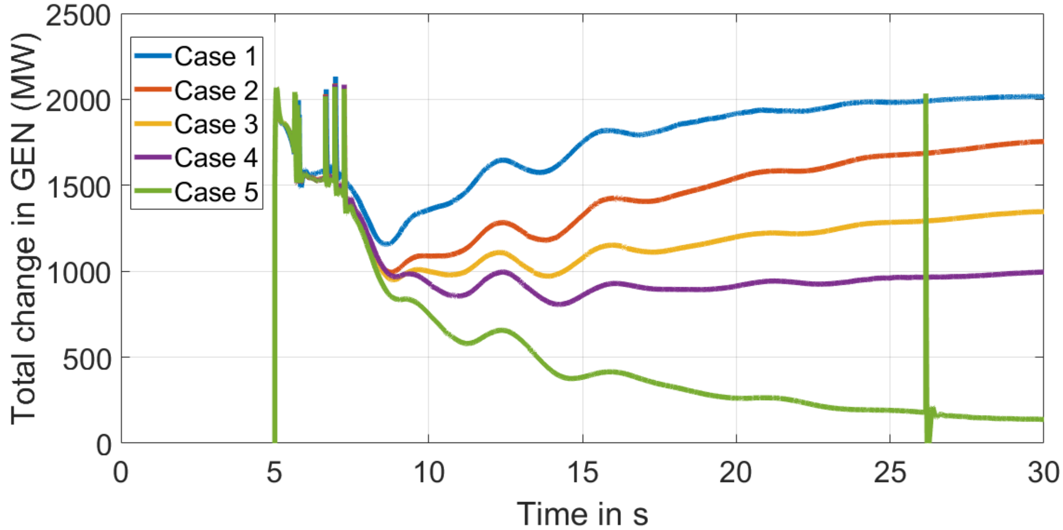


**Figure 4.3:** Change in generation with generator headroom

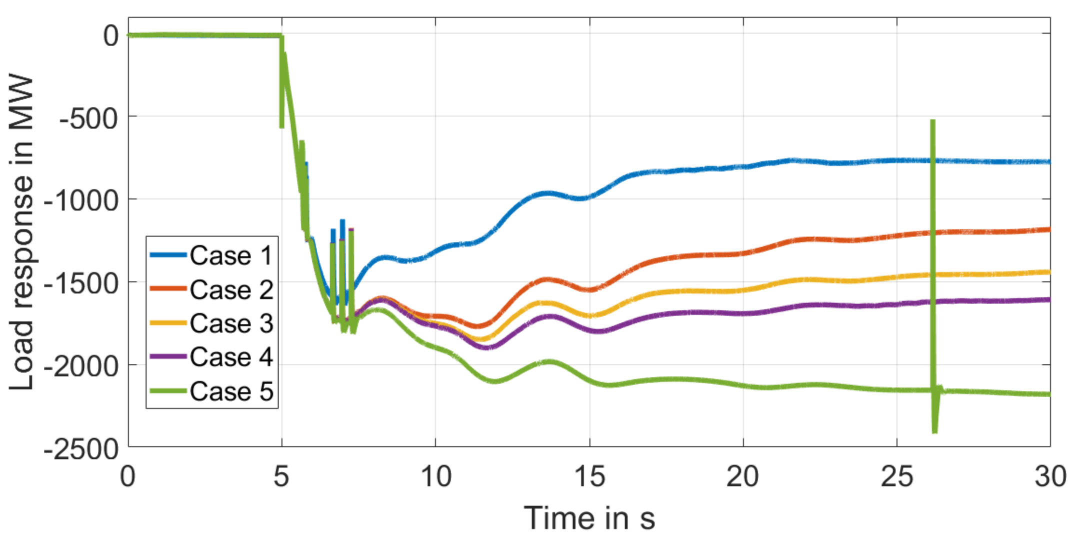


**Figure 4.4:** Change in load response with generator headroom

In the base case, the generators are able to increase their power generation by almost 2000 MW and the load reduces by 700 MW, thus stabilizing the frequency at 59.9 Hz. However, with decreasing governor response, the settling frequency keeps decreasing, thus leading to increased load response.

In Case 5, with no governor response, the total active power in load reduces by almost 2100 MW, thus stabilizing the frequency at 59.6Hz. Considering the UFLS limit of the WECC system is 59.5 Hz, theoretically speaking, the system does not require additional frequency support under these conditions. However, the load response constantly changes and cannot be relied on completely.

In the next set of simulation studies, the effect of inertia change on the frequency response is studied. In these studies, the governor response is not changed from the base case and the load models are also unchanged. The inertia is reduced to 80%, 60%, and 40% of the base case.

The frequency response of these cases is shown in Fig. 4.5. It can be seen that even with the loss of two large generators, the minimum frequency reached is around 59.83 Hz. When the inertia of the system is reduced, the ROCOF increases and the frequency nadir also reduces. However, the settling frequency remains the same. This is expected as the settling frequency is primarily determined by the governor response. The response of the generators is shown in Fig. 4.6. The initial change in generation is due to the inertial response. With reduced inertia, the initial power quickly reduces and the governors eventually start contributing. As shown in Fig. 4.7, the load also responds initially to the drop in voltage and then eventually to the change in frequency. As the composite load models have been used in this simulation, the reduction in frequency affects the final power of the load.

In the other extreme case, all governors are disconnected and the frequency response of the system is studied to determine the minimum FRR. The frequency response of the system is shown in Fig. 4.8. It is seen that in this case, the settling frequency reached 59.6 Hz, which is higher than the UFLS level considered (59.5 Hz). The change in generation is shown in Fig. 4.9. The change in power in the load is shown in Fig. 4.10. The composite load response compensated for the loss of generation and thus stabilized the frequency of

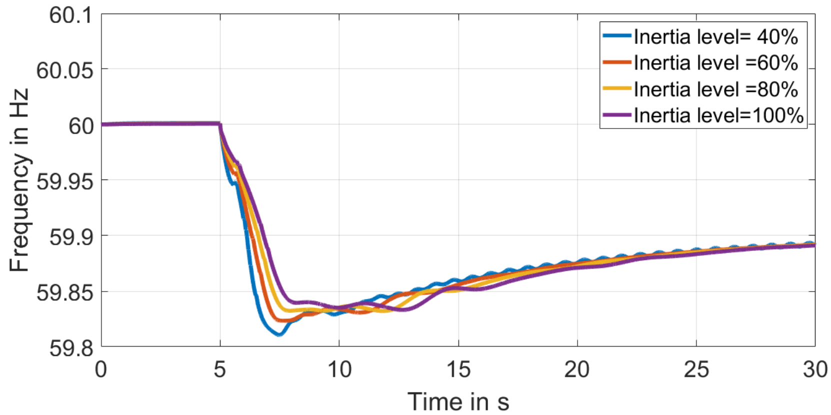


**Figure 4.5:** Change in frequency response of the system with inertia with all governors

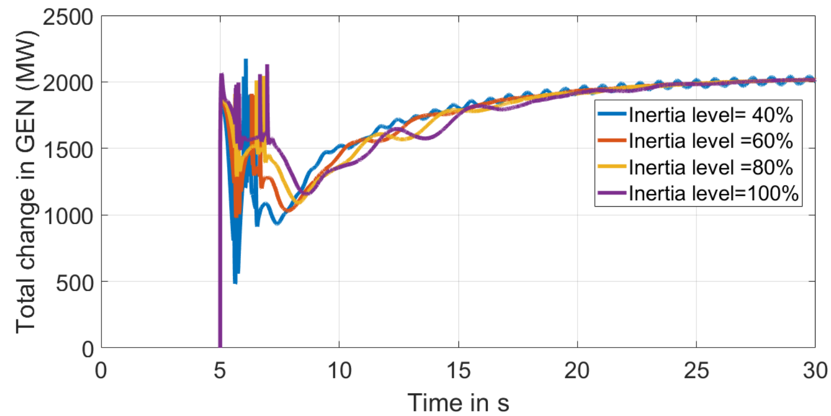


**Figure 4.6:** Total change in generation with inertia with all governors

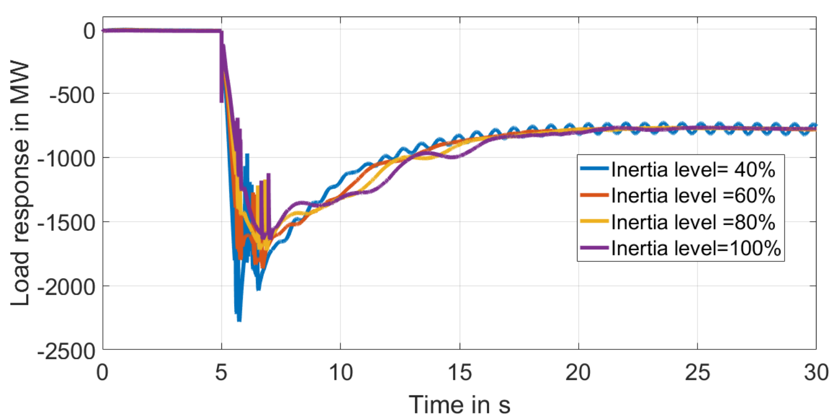


**Figure 4.7:** Total change in load with inertia with all governors

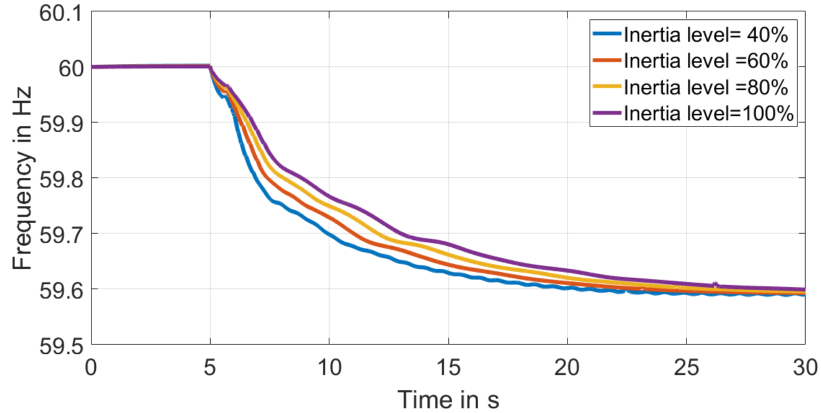


**Figure 4.8:** Change in frequency response of the system with inertia with no governors

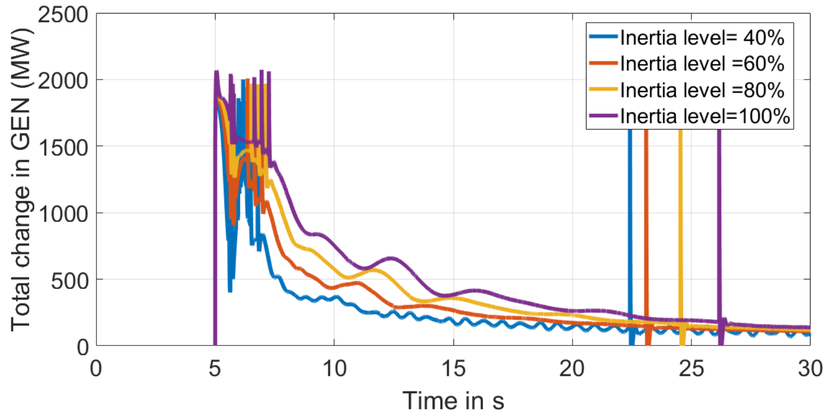


**Figure 4.9:** Total change in generation with inertia with no governors present

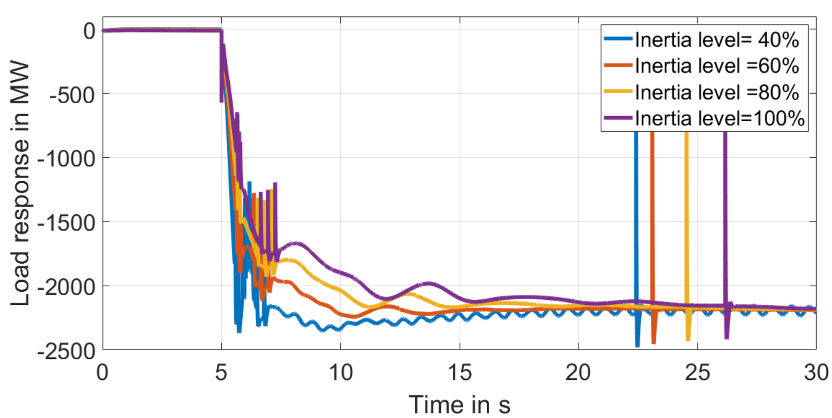


**Figure 4.10:** Total change in load with inertia with no governors present

the system. Considering this is the peak load case and the contribution of load response is significant, the frequency response of this scenario might be the best case scenario.

Finally, the effect of load response is reduced by ignoring the composite load model and replacing it with an 80% constant P and 20% constant Y model. For this case, the governor response is unchanged from the base case. However, the inertia levels are changed. The frequency response is shown in Fig. 4.11. It is clear that without the load response, the nadir of the base case has reduced to 59.74 Hz.

When the inertia is further reduced to 40% of the base case, the nadir reduces to 59.7Hz. The governor response is almost uniform and the change in generation is shown in Fig. 4.12. The load response is shown in Fig. 4.13: there is an initial reduction in load as the load is also composed to 20% constant Y, which is voltage dependent. However, the load response quickly reduces to zero.

In order to find minimum response limits for different inertias, the model is first validated based on FNET measurements. As seen in the previous simulation study, with composite loads enabled, the load response is quite high. Therefore, it is seen that the frequency response of the model is better than the measurements.

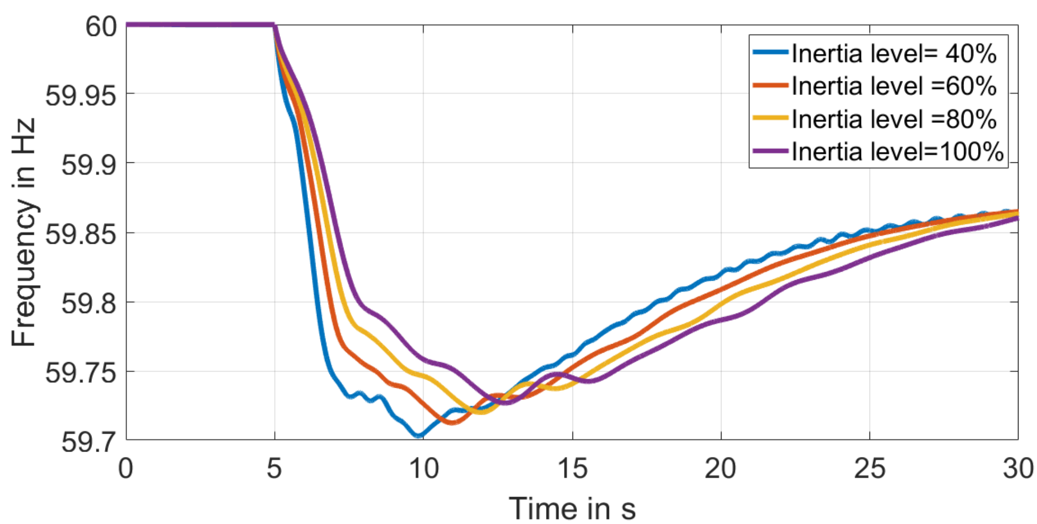


**Figure 4.11:** Change in frequency response of the system with inertia with 80% const P and 20% const Y load

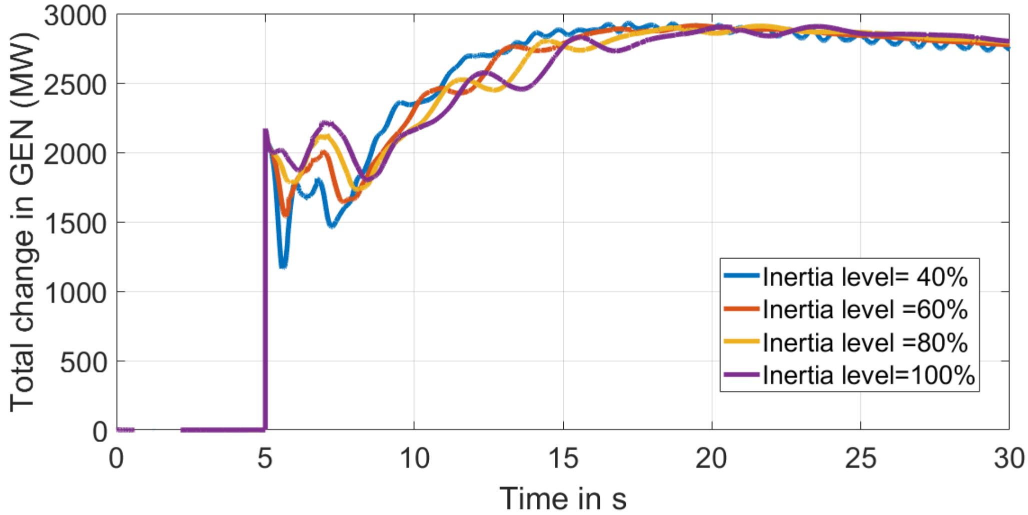


**Figure 4.12:** Total change in generation with inertia with 80% const P and 20% const Y load

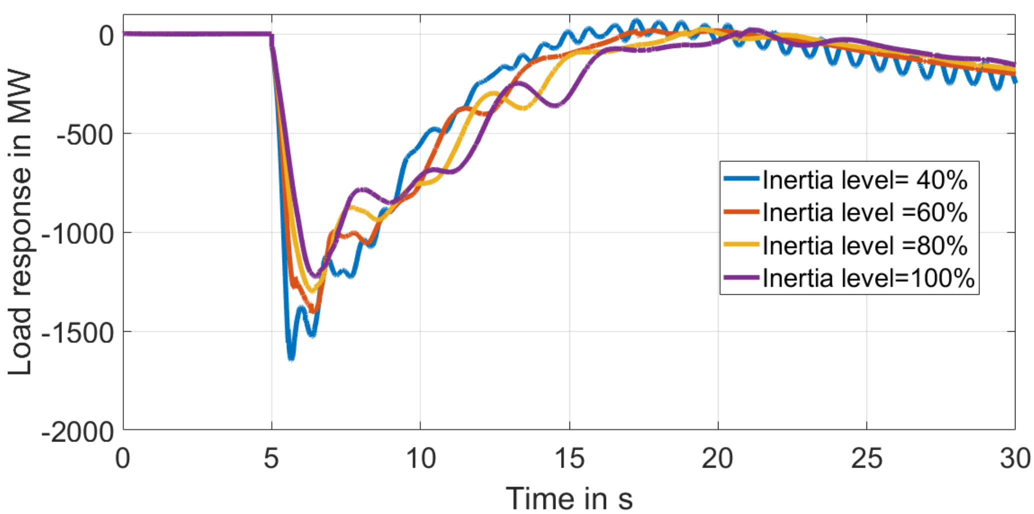


**Figure 4.13:** Total change in load with inertia with 80% const P and 20% const Y load

Some of the dynamic load models are disconnected and the model is tuned. The comparison of the frequency response of the tuned model and the FNET measurements is shown in 4.14. Using the tuned model, the inertia of the system is changed to various levels and the governor response is varied until the UFLS limit is reached. Then a plot of the variation of the minimum FRR with inertia is plotted in the curve shown in 4.15. The governor headroom required increases with decreasing inertia. However, in this scenario the minimum inertia level could only be reduced to 40% of the initial value. Even in this scenario, the amount of governor response required was less than the value in the base case.

## 4.5 Conclusion and Future Work

A frequency response study is done on the WECC system. This frequency response study considers both change in inertia and the load characteristics to assess performance of the system. The simulations were done on the 2019 PSLF model. It is observed that the load response to change in frequency is significant and the UFLS limit could not be reached with the base case. However, when the composite load model is disconnected, the UFLS limit is reached with reduced generator headroom. With reduction in inertia, the minimum frequency response reserve required increases.

In the future, models in which the conventional generators are replaced with PV models will be studied. The effect of seasonal and daily variation in inertia and load response will also play an important role in determining the minimum frequency response reserve.

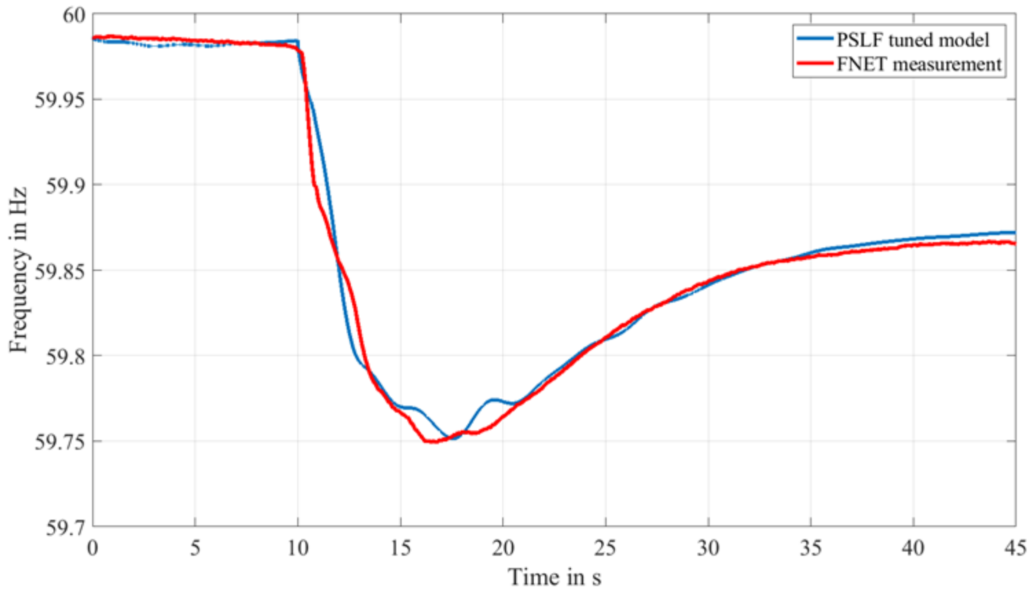


**Figure 4.14:** Comparison of the model and measurement

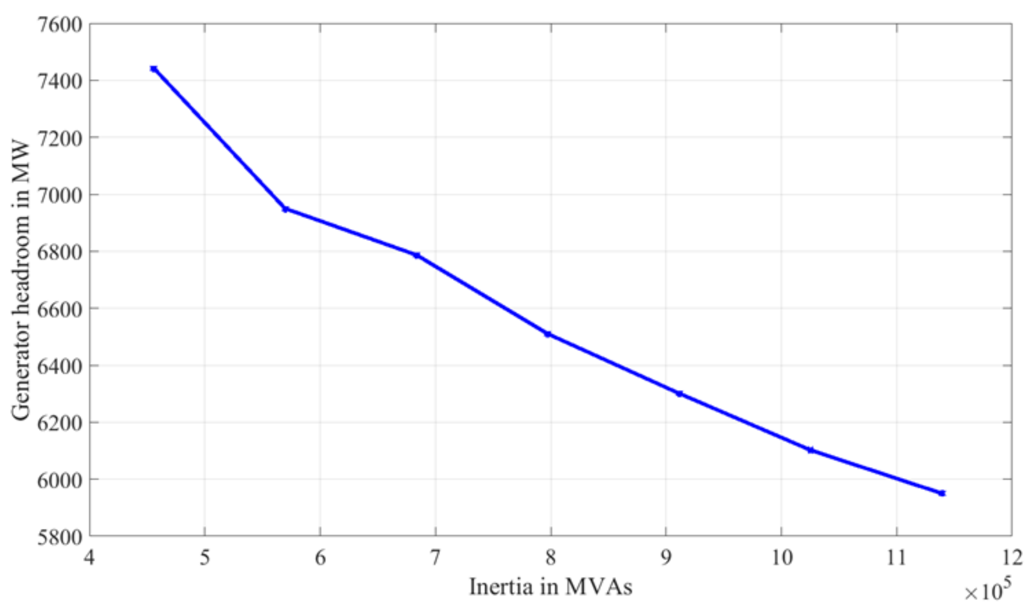


**Figure 4.15:** Change in minimum frequency reserves with inertia

# Chapter 5

# Improving Transient Stability of the Western Interconnection using HVDC

## 5.1 Introduction

A system is said to be transiently stable if all the generators maintain synchronism after a large disturbance in the system [45]. The instability can be explained as follows: During a large disturbance, a synchronous machine is unable to transfer electrical energy to the grid. The mechanical energy input remains constant due to slower controls. The kinetic energy in the rotor builds up, and the machine accelerates and eventually will lose synchronism with the rest of the system. This is generally depicted using the equal area criterion. In these cases, the system can become unstable in a matter of seconds.

The ability of a HVDC system to improve stability was first shown in [46] using a simple system. The improvement in stability was explained using the equal area criterion. It was experimentally shown that amount of initial DC power has a significant impact on transient stability. With the development of digital simulation, additional tests were conducted to determine the factors that affect the improvement in stability using HVDC [47]. Factors like duration of DC current, rate of increase of DC current, location of DC link, and in some cases power flow reversibility seem to affect the ability of HVDC to influence the stability of the system.

In the 1970s, the power in the Pacific DC Intertie (PDCI) was increased in steps after a detection of a fault. A feed-forward control scheme was used to ensure stability of the system [48]. However, in subsequent years, the focus of HVDC auxiliary control was more on small signal stability rather than first swing stability. A system can become first swing unstable in a matter of seconds. Therefore a fast controller is crucial. Recently, a PD controller was proposed to improve the first swing stability [49]. The controller was tested using a simple 9-bus system. The input to the controller was the speed of the generators. The controller proved to be effective for this system, but the PD controllers are susceptible to noise.

The number of HVDC lines in China is increasing. Therefore, there has been a lot of focus in utilizing the auxiliary control of HVDC to improve stability of the AC-DC corridor. In an earlier work [50], a bang–bang auxiliary controller was proposed to improve the transient stability of the system. Depending on the rate of change of voltage phase angles at the terminal, the power in HVDC would be either increased or decreased to a pre-selected level. In another work [51], there was a proposal to use the power flow in the parallel AC line as an input to modulate the power in HVDC. The main aim of this paper was to suppress the peak value during large oscillation in the parallel AC line. They have experimentally tested this controller.

With improvement in wide area measurements, there have been several attempts to develop a WAMS-based HVDC controller. WAMS-based HVDC auxiliary controls are also effective in improving the small signal stability of the system. The effectiveness of these controllers has been demonstrated for both the WECC system[52] and the Chinese system [53]. In the context of transient stability improvement, a study was conducted on the simple GB system to use wide area measurements to control the power output of the HVDC line [54]. The researchers have tested both event-based trigger and response-based trigger. They were able to show that a system that was previously unstable became stable with the help of auxiliary control.I n [55], optimal control of an HVDC system have been proposed. All of these controllers have their own advantages and disadvantages [56–58].

In most of these cases, the simulation tests were conducted on simple systems. There is a need to study the effect of using the auxiliary controller on a detailed system not only to prove its effectiveness but also to ensure it does not have any adverse effects on the power system. In this work, phase angle and frequency measurements–based transient stability control is proposed and compared with the frequency measurement–based control. Furthermore, integrated emergency power control that includes post-contingency corrective power flow control is also proposed. The controller is tested on the detailed WECC system, improving the transient stability limit on the AC-DC corridor present in the WECC system.

## 5.2 Emergency Power Control of HVDC System

The auxiliary controller of an HVDC system for emergency power control (EPC) under grid disturbances is shown in Fig. 5.1 (reproduced from [59]). The integrated emergency EPC controller includes the following functions:

1. Transient stability control function to provide timely synchronizing torque to the AC network and prevent the risk of instability caused by critical swing
2. Corrective power flow control to mitigate post-contingency stress of AC network
3. Power oscillation damping control function to provide sufficient damping torque to the AC network and prevent the risk of instability caused by poor damping.

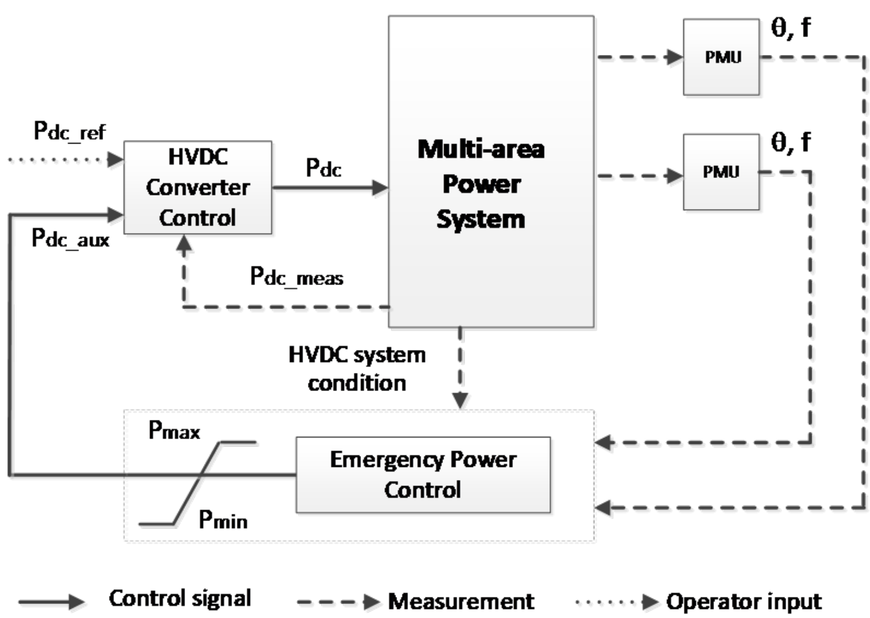


**Figure 5.1:** Schematic of integrated EPC scheme

Power oscillation damping strategies using HVDC for the WECC system have been investigated in detail[52, 53]. The focus of this work is on the transient stability control and the post-contingency corrective power flow control strategies.

### 5.2.1 Transient Stability Control

There are two types of triggering criteria that can be used for the control systems:

1. Event-based controls: If certain critical contingencies can be determined that cause instability in the system, the auxiliary control can be triggered when these contingencies happen. This control is similar to a Remedial Action Scheme. They are simpler to implement. However, they are insensitive to the level of instability.

2. Response-based controls: These are controls which are based on the continuous measurements of certain quantities like frequency, phase angle, and power flow in the AC lines. The response-based controls provide additional information regarding the level of instability and help take appropriate mitigation steps. In this work, a response-based control scheme has been implemented.

The two measurements that are used for the transient stability control schemes are the following:

1. The first control scheme is based on frequency input. In this control, the power flow through the HVDC system is varied according to the frequency difference of the converter terminals. The power can be increased or decreased based on detected frequency difference:
$$\Delta P_{dc} = K_p * \Delta f \tag{5.1}$$

2. The second control scheme is based on phase angle input. This control is also a response-based control. In this control, the power flow through the HVDC system is varied according to the phase angle difference of the converter terminals. The power can also be increased or decreased based on the detected phase angle difference:

$$\Delta P_{dc} = K_p * (\Delta\theta - \delta\theta_{ref}) \tag{5.2}$$

Unlike the frequency difference, which is zero in pre-disturbance and post-disturbance steady states, the phase angle difference during pre-disturbance and post-disturbance steady states may be quite different due to possible line trips. Hence, a reference angle difference needs to be considered such that the control acts only when the phase angle difference changes dramatically from the pre-disturbance reference value. A proportionality constant ($K_p$) is to be chosen such that the HVDC system provides sufficient response. The control is triggered only after the frequency difference or phase angle difference is higher than a preset value. This preset value is to ensure that small disturbances do not trigger the auxiliary controller. The control diagram is shown in Fig. 5.2

The complete proposed controller for transient stability is shown in Fig. 5.3. The first step involves collecting local or wide area measurements. A large disturbance in the power system is detected using these measurements, and the transient stability controller is activated. Depending on the control algorithm, the controller provides an auxiliary signal to increase or decrease the HVDC current or power orders. The HVDC system might not be able to provide the additional support if it is not in normal operation condition; for example, if the fault is close to the converter station. Therefore, the power change is activated only after the DC system reaches the normal conditions. The controller continues to function until it detects that the system has become stable or critical power swing has been effectively mitigated. In most cases, the first swing is considered to be critical. Hence, the controller would be switched off after the system is seen to be stable.

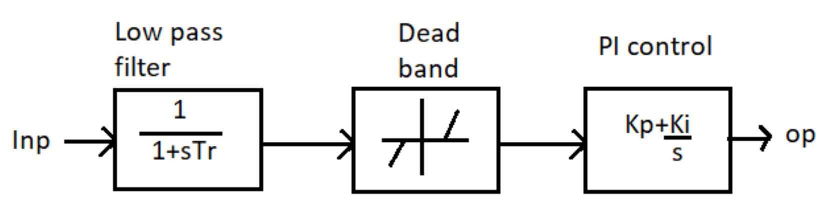


**Figure 5.2:** Proposed controller

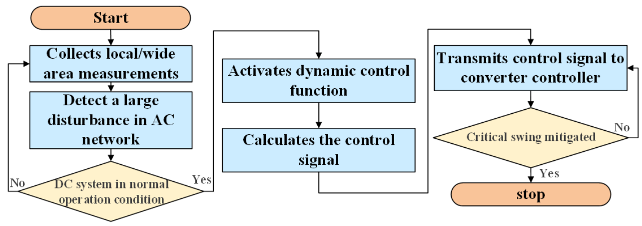


**Figure 5.3:** Illustration of the control algorithm

### 5.2.2 Corrective Power Flow Control

The corrective power flow control function is dispatched if there is sufficient

automatically redispatches the post-contingency power flow of the HVDC system by emulating the power flow response of an AC transmission line. The power flow on an AC transmission line can be expressed in terms of the power angle relationship as follows:

$$P = \frac{U_1 U_2}{X} sin(\theta_1 - \theta_2) \tag{5.3}$$

In terms of the HVDC system, the power P can be modulated by the converter station, while U1 and U2, and can be measured at the converter terminal AC buses. Thus, the AC line impedance emulated by the HVDC system by modulating the power P is

$$X = \frac{P_{DC}}{U_1 U_2 sin(\theta_1 - \theta_2)} \tag{5.4}$$

Following a network contingency, the HVDC system can modulate power flow according to this target impedance as

$$P_{DC} = \frac{U_1 U_2}{X_{ac-emulated}} sin(\theta_1 - \theta_2) \tag{5.5}$$

## 5.3 Study System Discussion

The auxiliary control is tested on the PDCI in the Western Interconnection. The PDCI currently transfers around 3220 MW from the northwestern region to California. When the power transfer in the parallel AC transmission path called the California-Oregon Intertie (COI) is also included, the total power flow in the AC-DC corridor is above 8000 MW

(Fig. 5.4, reproduced from [60]). COI consists of three 500 kV lines: One line from Olinda to Captain Jack and the double circuit lines from Round Mountain to Malin. As a result, this is also one of the most congested paths. Improving the transient stability of this parallel AC-DC system using auxiliary control could lead to additional power transfer from the northwestern region to California.

The simulation study is performed using the PSLF (Positive Sequence Load Flow) software. The detailed dynamic WECC model consisting of over 21,000 buses is used to test the controller. The DC system is modeled in the system using the EPCDC model available in the standard library. A user-defined model is developed to model the auxiliary controller. The inputs to the controller are the measurements taken at the rectifier (Celilo Station) and the inverter station (Sylmar). The overloading capability is initially assumed to be 20% for a few seconds. The threshold for the frequency-based controller is triggered at 0.1 Hz and the threshold for the angle-based controller is 40 degrees.

The controller is initiated after the converter is operating under normal conditions. In this simulation, the voltage at the converter terminals must be above 0.9 pu to enable the control action. The controller gain and the time constants are tuned to optimally control the power flow in the DC system. The controller is switched off after the system becomes stable to avoid unnecessary control actions.

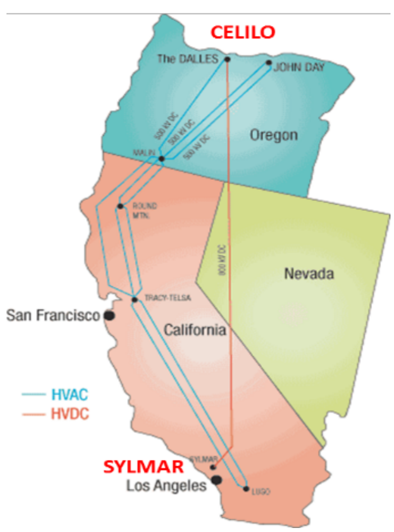


**Figure 5.4:** PDCI with parallel AC lines

## 5.4 Simulation Results

### 5.4.1 Case Descriptions

After large number of simulations, it is seen that the base case of the test system is very stable with respect to first swing stability. In order to test the controller under stressed conditions, with large power flow from north to south, a new case is developed. The power flow from north to south is increased to around 4500 MW [61, 62].

After testing many cases, the first swing instability is seen when a three-phase-to-ground fault is applied at the Malin substation and the fault is cleared after 300 ms. This condition is made severe by opening two AC transmission lines of COI (Round Mountain–Malin) after the fault is cleared. Thus the power flow in from the north to south will primarily flow through PDCI and the AC transmission line connecting Olinda and Captain Jack.

The performance of the controller is shown through the simulation results in Figs. 5.5, 5.6, 5.7, and 5.8. It is clear from the phase angle plot 5.6 that the system becomes transiently unstable when the controller is not present. Both frequency- and phase angle–based controls make the system transiently stable.

The frequency-based control is triggered when there is a large frequency difference between the two regions. Frequency difference between the regions is indicative of a difference in active power imbalance. Considering that the WECC system is synchronously connected, the system settles after the disturbance and the frequency of the entire interconnection is very close. The frequency control gets deactivated.

However, the phase angle–based control is triggered when there is a large difference in phase angles. Depending on the conditions of the system, the steady state settling value of the phase angle measurements will be different. In this controller, an additional control scheme to ramp down the power after mitigating the first swing instability is implemented. It is also feasible to ramp down the DC power to a value higher than the pre-disturbance scheduled power. This post-disturbance corrective power flow control will help reduce the stress of parallel AC lines during post-disturbance operating conditions.

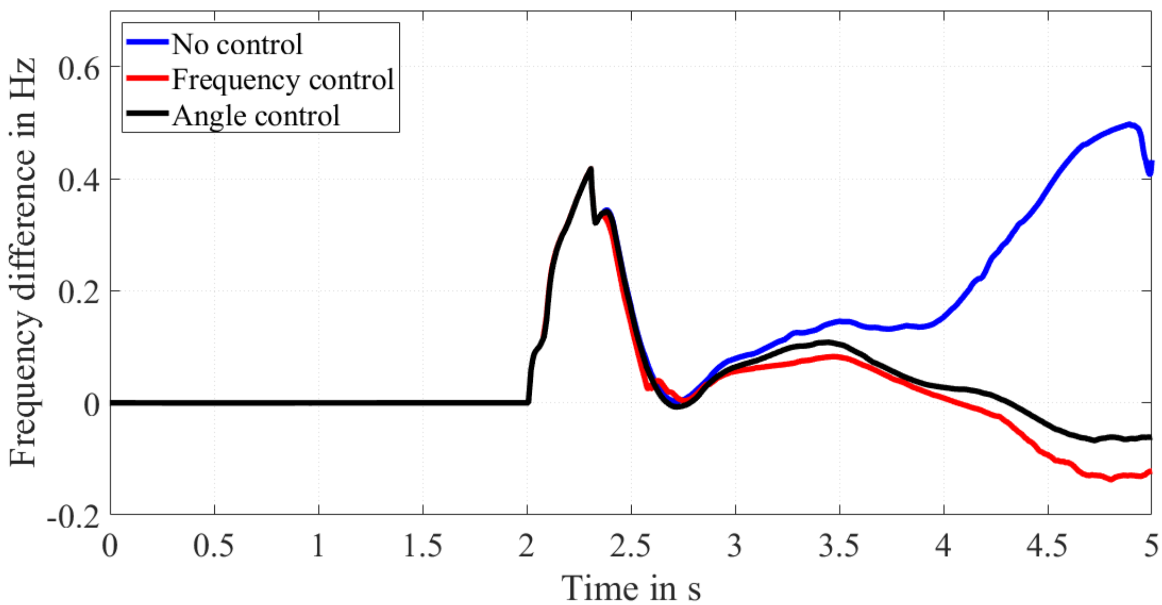


**Figure 5.5:** Frequency difference with different controls

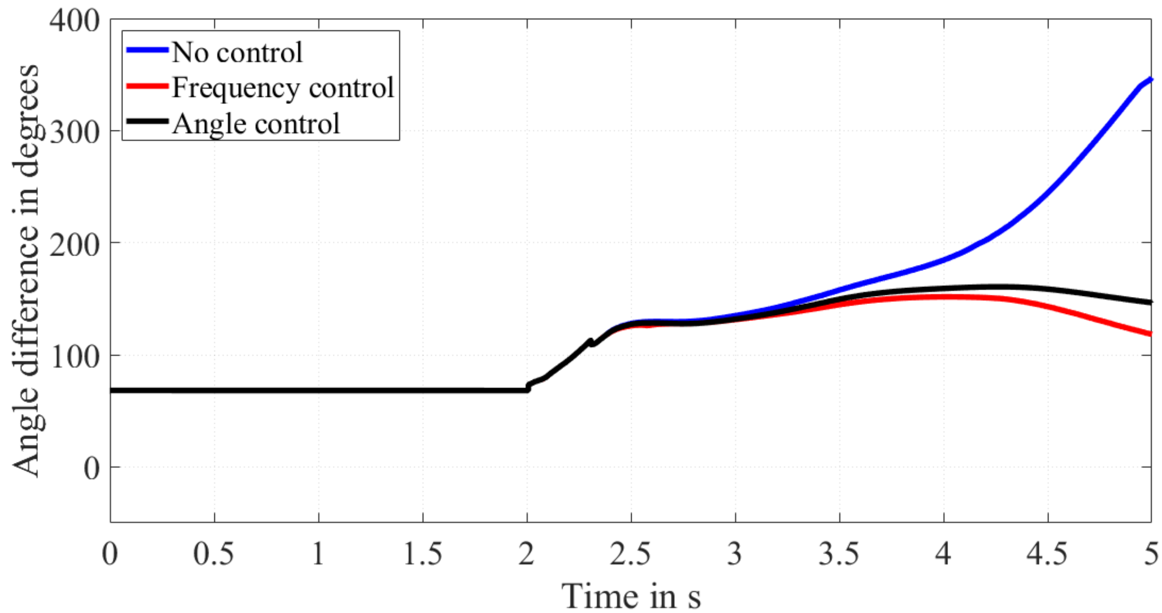


**Figure 5.6:** Phase angle difference with different controls

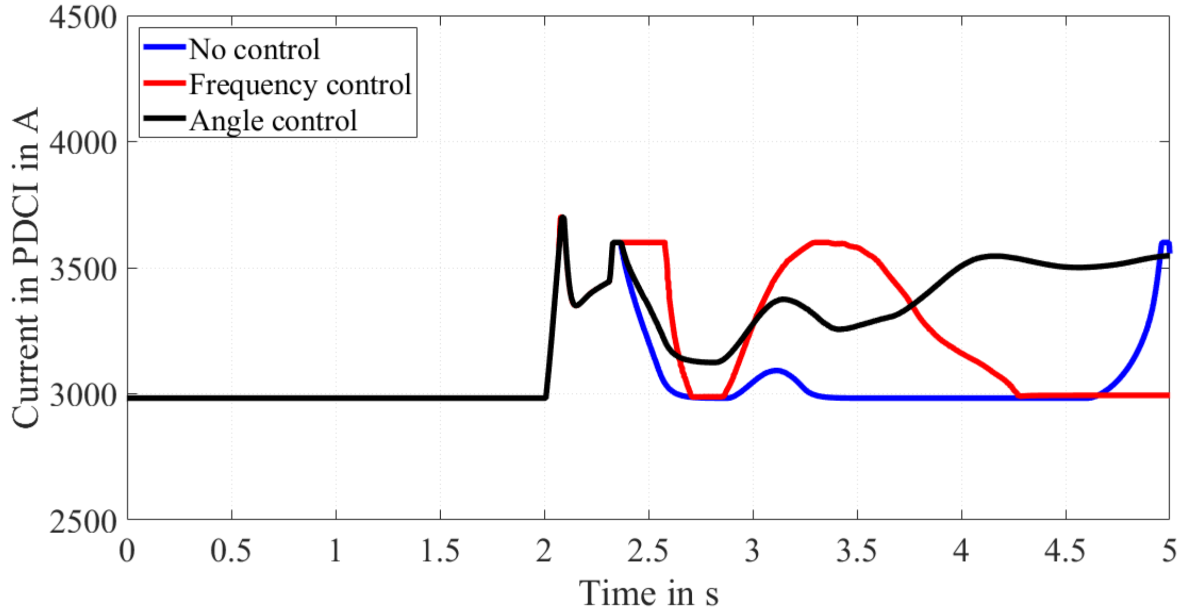


**Figure 5.7:** DC current in PDCI with different controls

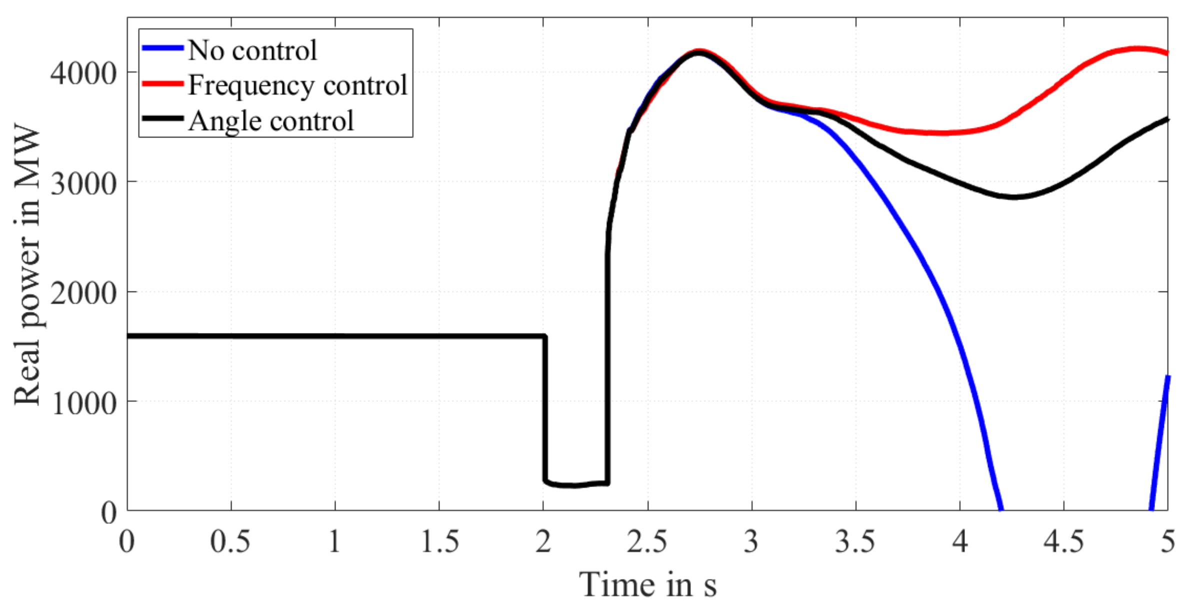


**Figure 5.8:** Power flow in Olinda–Cap-Jack line with different controls

## 5.5 Effect of Overloading Capability

One of the advantages of the LCC (line-commutated converter-based) system is that it inherently has overloading capability. Depending on the duration of operation, the LCC system can be overloaded to different levels 5.9. For the purpose of improving first swing stability, the overloading capability is needed only for a couple of seconds. However, it is important to know the minimum amount of overloading capability needed to ensure the system stability. Therefore, the following simulation studies are conducted to study the effect of overloading capability. The simulation results are presented in Fig. 5.10, Fig. 5.11, Fig. 5.12, and Fig. 5.13. It is seen that with both 5% and 10% overloading capability, the system becomes unstable. Thus, 20% overloading capability seems to be the appropriate amount to improve the transient stability of the system.

## 5.6 Corrective Power Flow Control

As shown in Fig. 5.9, the system can have different transient overloading capabilities based on the duration. After the first swing instability is mitigated, the power flow of the HVDC system could be changed to long-term overloading capability level to alleviate some of the stress on the AC system during contingency.

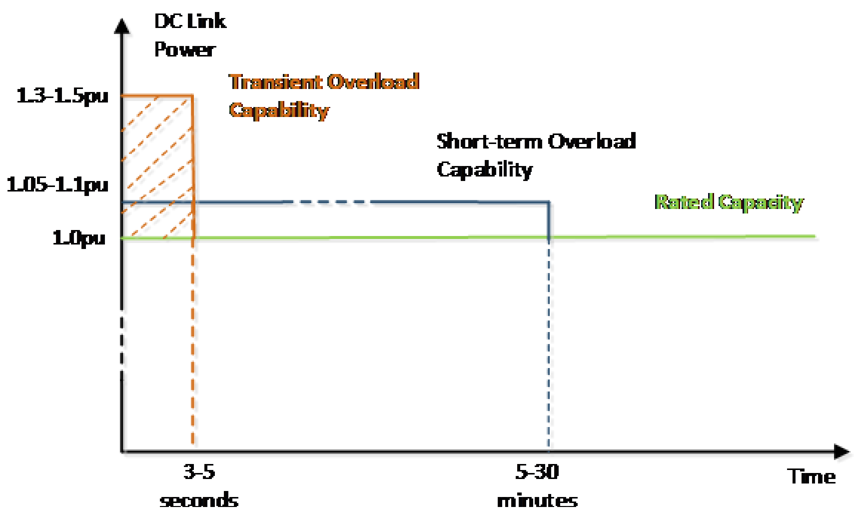


**Figure 5.9:** Overloading capability of LCC HVDC system

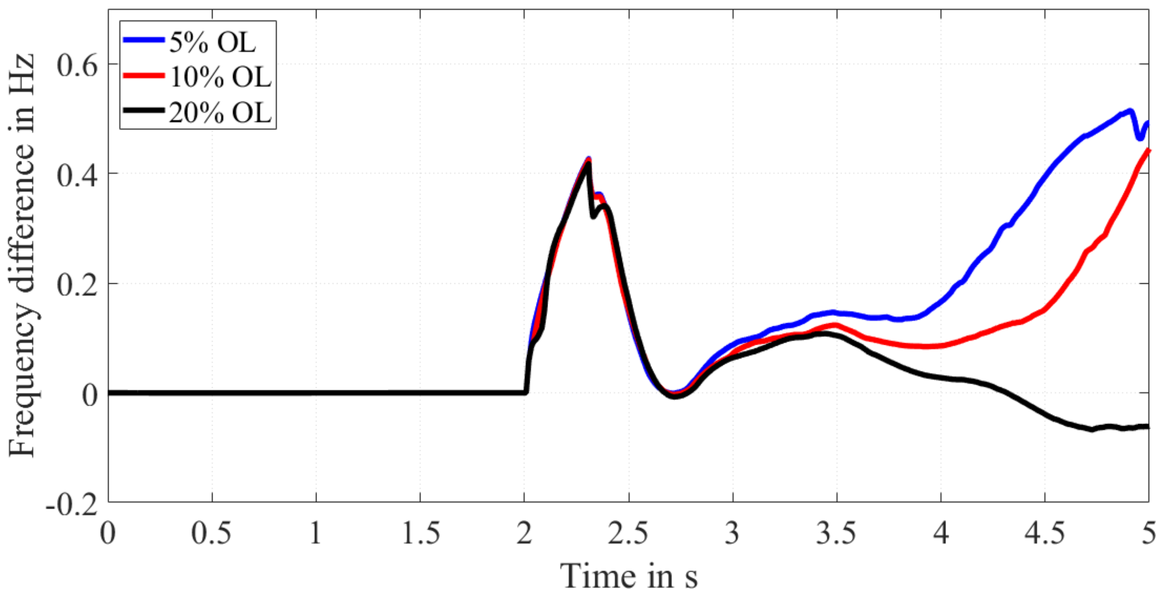


**Figure 5.10:** Frequency difference with different overloading capability

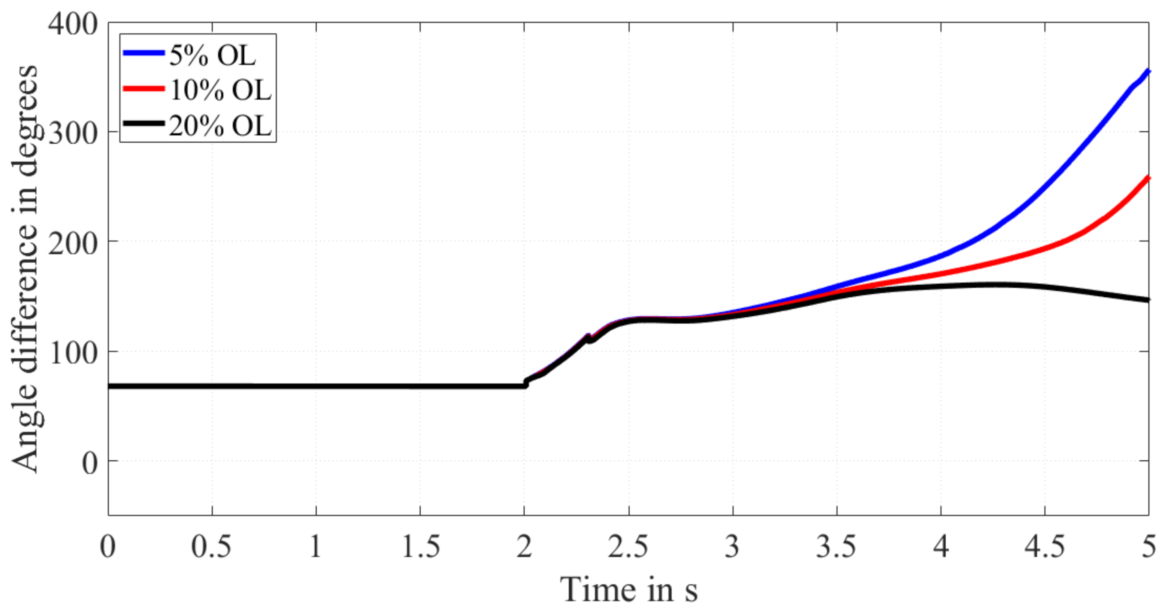


**Figure 5.11:** Phase angle difference with different overloading capability

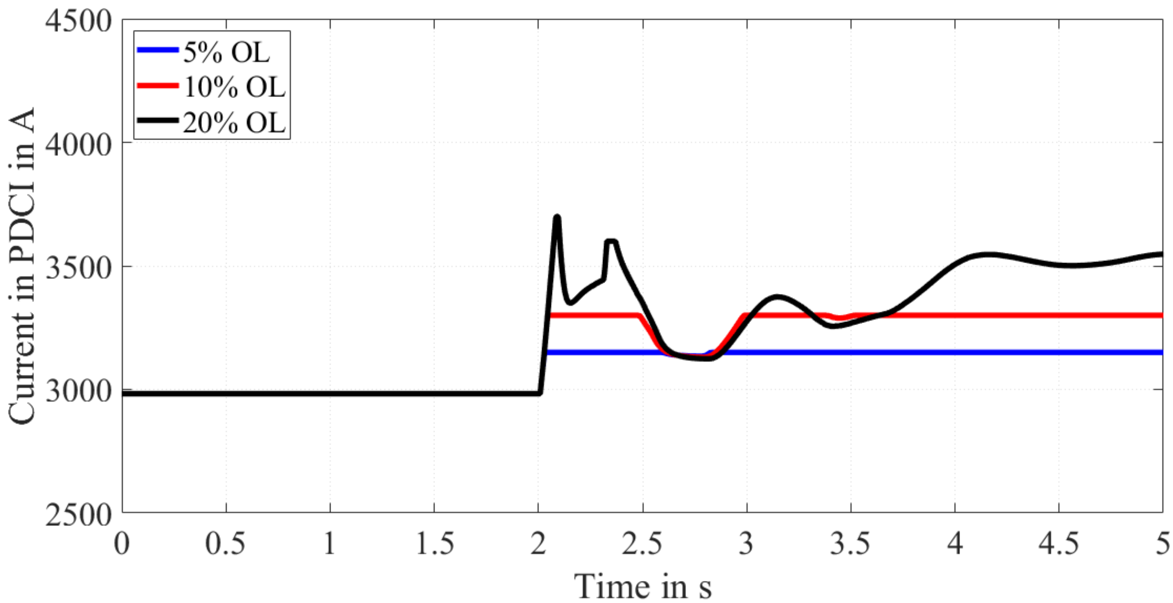


**Figure 5.12:** Power in PDCI with different overloading capability

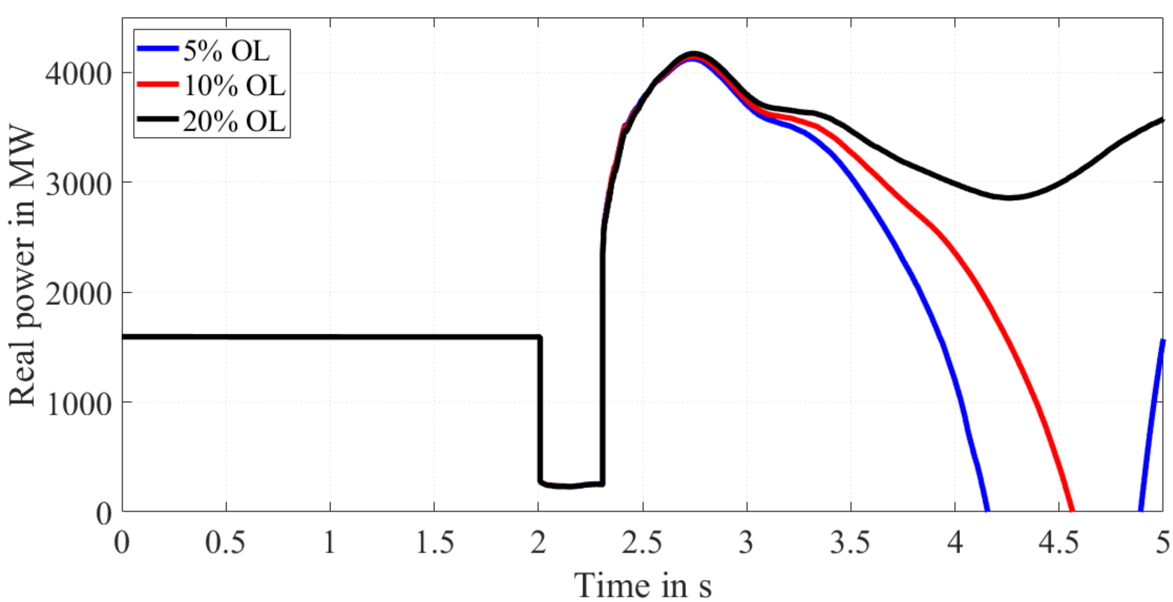


**Figure 5.13:** Power in Olinda-Cap-Jack line with different overloading capability

The DC current flowing through the HVDC line is shown in Figs. 5.14 and 5.15 The increased power flow in the HVDC system causes a reduction in the power flow of the parallel AC system, thus reducing the stress on the AC line. The current in the PDCI is ramped down to around 3250 A. Assuming the rating of the PDCI is at 3220 MW at 520kV, this corrective control is set at 5% overloading capability.

## 5.7 Conclusions

With increasing load, transmission systems are being operated closer to their limits. Apart from upgrading the transmission lines, which involves a lot of planning and investment, there is a need to find innovative control schemes to also operate the existing system more efficiently. Therefore, in this chapter, an auxiliary controller that utilizes the overloading capability and the precise and fast power control of HVDC system to improve transient stability is proposed. The effectiveness of this controller is demonstrated by simulation studies conducted on the detailed WECC system model.

Considering the wide range of possible controls, in the future it would also be beneficial to study a hierarchical control. This would be able to take necessary control actions according to the prevailing conditions. Hence, instead of using HVDC to provide a single functional control, it might be able to provide a wide range of controls that improves the stability in all the areas. This hierarchical control would be able to receive wide area information and analyze the situation and take the necessary control actions. It might be providing additional damping or reactive power support or power reversal etc. Power system control would be a lot more definite when HVDC is used. Hence, this would enable the increased power flow across congested corridor, increasing the rate of inclusion of renewable energy sources and also providing much-needed ancillary services. HVDC could eventually play a vital role in power markets. The adverse effects of HVDC would also have to be studied in detail as they depend on the system characteristics and conditions.

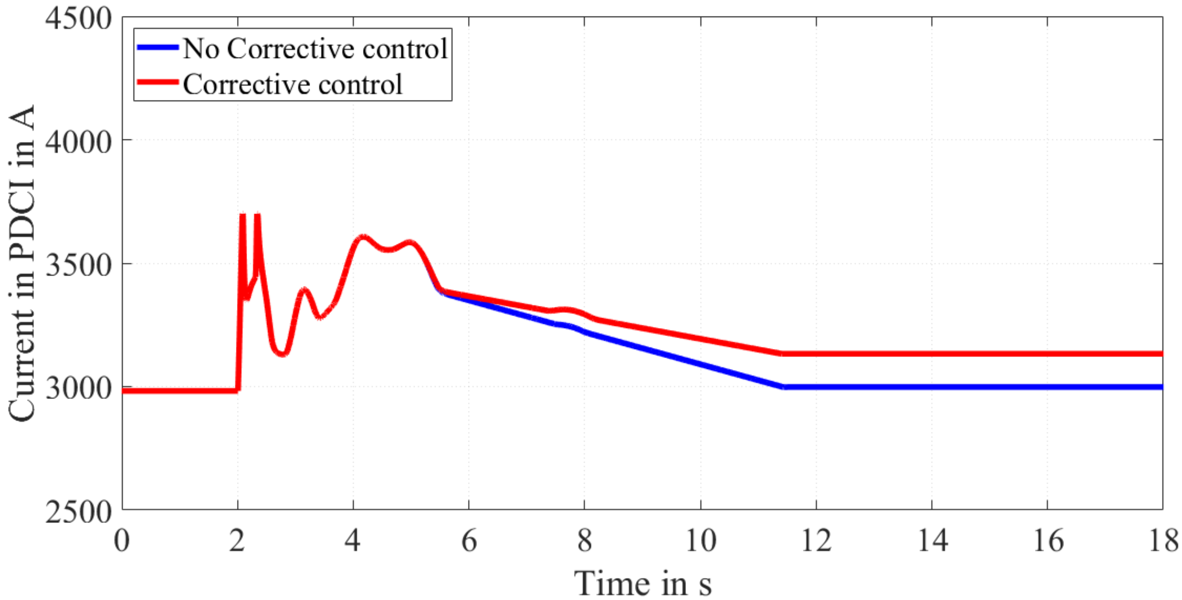


**Figure 5.14:** DC current in PDCI (Corrective power flow control)

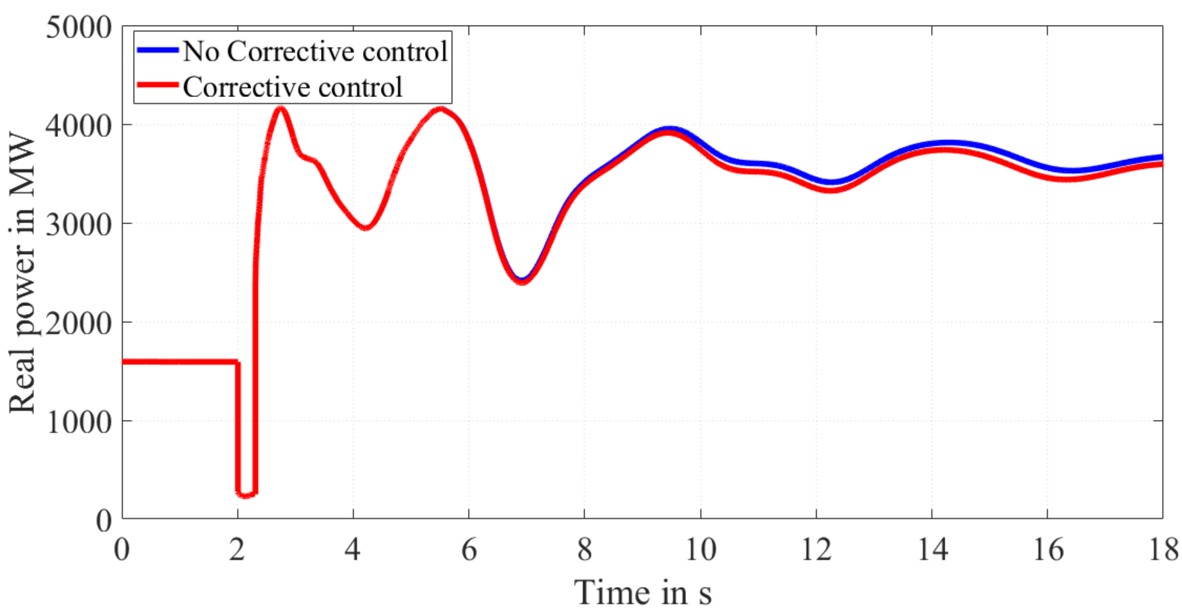


**Figure 5.15:** Power flow in Olinda–Cap-Jack line (Corrective power flow control)

# Chapter 6

# Developing a North American Large-Scale Simulation Model

## 6.1 Introduction

The four major interconnections in North America (excluding Alaska and Mexico) are the Eastern Interconnection, Western Interconnection, Quebec Interconnection, and Texas Interconnection. The Eastern Interconnection is connected to the Western Interconnection with six DC ties, to the Texas Interconnection with two DC ties, and to the Quebec Interconnection with four DC ties and a variable frequency transformer. The interconnection diagram is shown in Fig. 6.1 (reproduced from [63]).

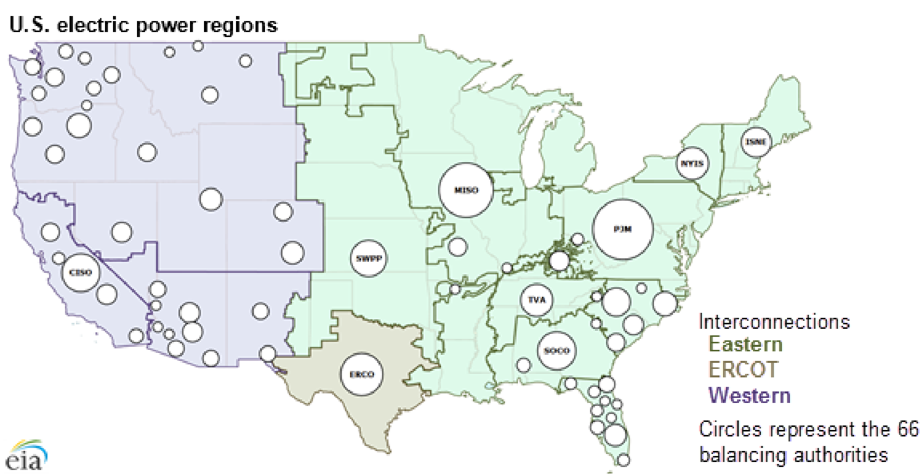


**Figure 6.1:** Interconnections in USA

As they are connected to each other through DC system, these interconnections are not synchronously connected. Therefore, the power system stability of each of these interconnections is not dependent on the others and can be studied in isolation. Thus, over the years, the reliability of each of these interconnections has been studied by themselves. Apart from the electrical reliability and stability issues, there are other factors like lack of natural gas, extreme weather patterns, or security threats like EMP or cyber attacks that have to be analyzed that may affect multiple interconnections at the same time.

With major improvements in communication technology, computation technology, and the push toward renewable energy, the advantages of connecting the grids are becoming undeniable. The advantages of connecting the grid with HVDC lines has been studied in [64]. It is seen that the operation of the entire grid can become more economical by connecting the interconnections and sharing the ancillary services like frequency response. As there are four different time zones in the United States, the load diversity in the system will be higher and also utilization of renewable energy will be more efficient. One of the first steps is to build a North American model that consists of the four interconnections.

There are detailed models of each of the interconnection; however, developing one model with all the interconnections has its own challenges. Over the years, each interconnection model has been developed in a software that suits the needs of that region. The utilities and the interconnection have also preferred certain software and developed accurate large-scale models of their territory or interconnection in those software. For example, PSLF software is more commonly used in the Western Interconnection and PSS/E (Power System Simulator for Engineering) software is more commonly used in the Eastern Interconnection. As a result, user-defined models that are not present in the standard libraries have also been developed, which are difficult to convert. Therefore, conversion of dynamic models from one software to another is not a straightforward process. These software also had memory limitations so that such a large model could not be developed.

In this work, PSS/E-33 software is chosen to conduct the simulation as the EI and ERCOT models have already been developed in this software. The WECC model is primarily developed in PSLF-19 software. Thus, to develop an intercontinental model, the first step is to convert the WECC model from PSLF software to PSS/E software. In this chapter, the process of developing a WECC PSS/E model is described and the accuracy of the models is compared. In the last section of this chapter, the detailed North American model is described.

## 6.2 Power System Model Conversion from PSLF to PSS/E

### 6.2.1 Literature Review

Transient stability simulation studies are conducted to study the behavior of a power system when a disturbance occurs. These studies determine if the system will return to a steady state operating point after the disturbance. One of the most common dynamic studies is the time domain simulation. In these simulation studies, both algebraic and differential equations are used to model the response of different elements.

Over the years, several pieces of commercial software have been developed that are used to model large power systems. In North America, the most commonly used programs are PSS/E, PSLF, PowerWorld, TSAT, etc. Basically, all these programs are able to solve power flow equations and also perform transient stability simulations. They all have inbuilt libraries of models that are populated with the power system components like generators, exciters, HVDC, FACTS, etc.

However, over the years many discrepancies have been found among the software [65–67]. Even though in theory they all solve the same set of equations, the differences in their proprietary algorithms cause the final solutions to be different. The models that are present in the different tools, though similar, have not been validated completely. Therefore, there will be differences in the final solution.

### 6.2.2 Power Flow Conversion

There is a tool available with the PSLF software that converts the power flow data into the PSS/E format. The epti.p program exports the load flow data in memory into the PTI PSS/E compatible load flow data. The program is able to convert it into power flow for the following versions: 23, 24, 25, 26, 27, 28, 29, 30, 31, and 32. The power flow in PSS/E can be read while ensuring the same version option is chosen during the import process. Then a comparison of all the components present is done to check if there are any major components missing. The details of the comparison are shown in Table 6.1.

- Buses:In PSLF there are 586 three-winding transformers that all have a dummy bus included in them. This dummy bus is not present in PSS/E. In PSS/E there are 354 additional dummy buses added in multi-sectional lines not included in PSLF. That still leaves PSS/E 232 buses short. In the conversion there are 232 buses. Hence all of the buses have been converted.

- Shunts: Switched Shunts in PSS/E are limited to one per bus with no ID. The WECC Siemens converter changes multiple switched shunts from the epc format to single switched shunts with no ID connected to dummy buses with low impedance branch to original bus.

The load flow solution is found in the PSS/E software. The WECC converted model reached the solution when the number of iterations was increased to 30. The fixed Newton Raphson method is used. The comparison of the load flow solution is shown in Table 6.2

The generation power is also compared and shown in Table 6.3 It is seen that in the case of the real power generation, the maximum difference is observed on the swing bus generator.

**Table 6.1:** Basic comparison of the power flow models.

| | PSLF | pss/e |
|---|---|---|
| No. of buses | 20910 | 20678 |
| No. of branches | 16769 | 16788 |
| No. of Transformers | 8401 | 8402 |
| No. generators | 4063 | 4063 |
| Total P gen (MW) | 178703 | 178742 |
| Total Q gen (MVaR) | 21422 | 21873 |
| No of load loads | 10717 | 10717 |
| Total P load (MW) | 172577 | 172577 |
| Total Q load (MVaR) | 31363 | 31363 |

**Table 6.2:** Load flow solution comparison

| Comparison | Voltage | Phase Angles |
|---|---|---|
| Average difference | 0.0028 | 0.95 |
| Maximum difference | 0.0062 | 1.08 |
| Standard deviation | 0.00953 | 0.5470524 |

**Table 6.3:** Power generation comparison

| Quantity | Maximum difference | Average difference | Standard deviation |
|---|---|---|---|
| P generation | 38.1121 | 9.35E-07 | 1.69E-05 |
| Q generation | 20 | 0.601496 | 3.056204 |

The maximum difference is around 38 MW. The maximum difference in Q generation is seen where there are slight mismatches in the voltage of the buses connected to the generation.

### 6.2.3 Dynamic Model Comparison

The following issues related to the conversion of the models are as follows:

### 6.2.4 Generator Models

Detailed and accurate modeling of generators is one of the most crucial parts of transient simulation. The generator model in its most basic form is a Norton current source in parallel with a complex impedance.

The model that has been considered in this work is the PSLF 2016 high summer model.

One of the differences between the two simulators is in the data input for machine base. In both PSLF and PSS/E, the machine base can be specified in the power flow file. In PSLF, in addition to the power flow file, the machine base for the dynamic model can also be specified in its dynamic document. In PSLF, the dynamic file machine base is the final value that is considered. Therefore, the change in machine base after the dynamic file is loaded is recorded and changed.

In PSLF, the generators that do not have dynamic model specified are automatically converted to negative loads in the dynamic file. However, this automatic conversion is not possible in PSS/E. In PSS/E-33, the simulation cannot be initiated if all of the generators do not have a dynamic model associated with it. Therefore, in order to ensure consistency, the generator whose dynamic models are not specified are also converted to negative load models.

The machine impedance parameters had to be changed in between these models in order to ensure that the value is similar across the software.

In this version 33 of the PSS/E used, another feature is that renewable models have to be explicitly specified in the power flow file. Therefore, the data entry for the generators that are modeled as the renewable energy models is changed to ensure that the wind models could be added.

### 6.2.5 Governor Models

Frequency response study is the primary focus of the studies to be conducted using this model. Therefore, the governor response between the models has to be accurate. In this conversion process, additional attention is paid to ensure that the governor models are converted as precisely as possible. A list of the approved models by WECC [68] and the similarity between them is shown in Table 6.4

In most cases, each of the models will have to be modified to ensure similar responses from both the cases. These are the issues found during the conversion of the governor models that prevent the complete conversion between the two software.

1. There is a base load flag in the PSLF power flow model that indicates if the governor is frequency responsive. When this load flag is equal to 1, the governor is not allowed to increase the power in the generator. Thus, initially based on the base load flag, the corresponding governors are disconnected to ensure similar frequency response.

2. As shown in Table 6.4, there are some models like HYG3 and HYGOV4 that do not have an equivalent model in PSS/E. The model that is used in the converted PSS/E models have some similarities, but the final responses of the governors are quite different.

**Table 6.4:** WECC approved governor dynamic model

| PSLF model | PSS/E model | Equivalent model similarity |
|---|---|---|
| TGOV1 | TGOV1 | Exact |
| GAST | USGS3T | Exact |
| GGOV1 | GGOV1 | Almost |
| HYGOV | HYGOV | Exact |
| HYGOVR | HYGOVR | Exact |
| HYGOV4 | IEEEG3 | None |
| PIDGOV | PIDGOV | Exact |
| G2WSCC | WSHYDD | Almost |
| GPWSCC | WSHYGP | Almost |
| HYG3 | WSHYGP | None |
| IEEEG1 | WSIEG1 | Almost |
| IEEEG3 | IEEEG3 | Exact |

3. In the PSLF governor models, there is a provision to specify a different machine base for the governor module other than the machine base specified the generator. This is not possible in PSS/E. In some models like WHSYGPP and WSHYDD, a TRATE constant can be specified that changes the output of the governors by a factor to ensure the same output. However, this multiplication factor is not available in all models. In some models, the PMAX or a linear piecewise function is modified to account for the different base. However, this method is found to have some differences.

4. In generator models like GPWSCC and WSHYGP, IEEEG1 and WSIEG1, and HYG3 there is a linear piecewise function (LPF) block that controls the relationship between the gate position and the power. In the PSLF model, in some models, the function can be described with 6 points apart from the the assumed 0,0 and 1,1 as shown in Fig. 6.2. In case of PSS/E, only four points can be given, which should also include 0,0 and 1,1. Therefore, in one of the examples shown here when the power output is in the region where the functions are the same, the output is the same. In the portions with difference, the output can be different. This is illustrated in the Figs. 6.2, 6.3, and 6.4.

There are two generators in the simulation model that have the same governor dynamic models including the piecewise relationship function as shown in Fig. 6.2. However, the difference is in their total power output as shown in Figs. 6.3 and 6.4. The power output in the first case is around 19 MW, which is around 0.633 pu, and in the second case the power output is around 12 MW, which is around 0.4 pu. There is a difference in the LPF below 0.6 pu. Thus, the response is the same for case 1 shown in Fig. 6.3. However, there are small changes in the value for case 2 as shown in Fig. 6.4.

5. In PSLF, there are governor models like HYGOV that have additional blocks like linear piecewise relationship block and a phase shifter block, which are absent in the corresponding HYGOVP PSS/E block. They have the exact same response when these blocks are deactivated by making the time constants zero. However, in the cases when they are activated, there are differences in the final response

6. In some of the models there are deadband blocks. The value of the deadband blocks when converted are different. These differences also cause the response of the modules to be different.

In most cases, the response of the governors models is very similar. Therefore, the final outputs of the simulations are so close. However, there will certainly be scenarios when there are differences between the modules. It is important to be aware of these differences while conducting a study.

### 6.2.6 Other Plant-Related Models

The exciters and stabilizers are also tuned to ensure that performance of the two-simulation software is similar. The aim of this work was not to test each and every model present in the system. It is to develop a WECC model that could be used for frequency response studies. Therefore, an exhaustive model validation has not been done.

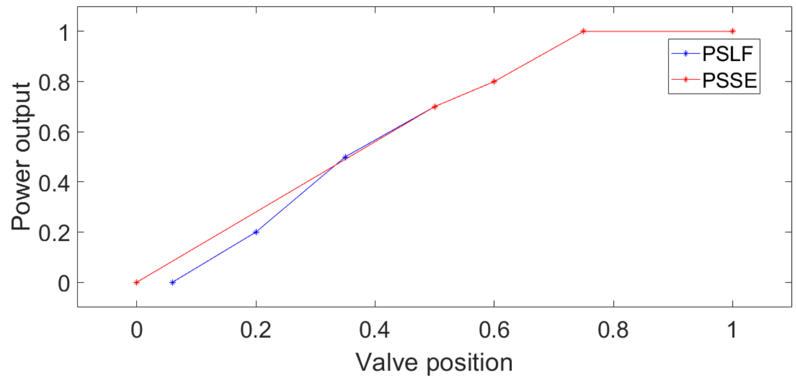


**Figure 6.2:** Piecewise linear relationship between gate and power output

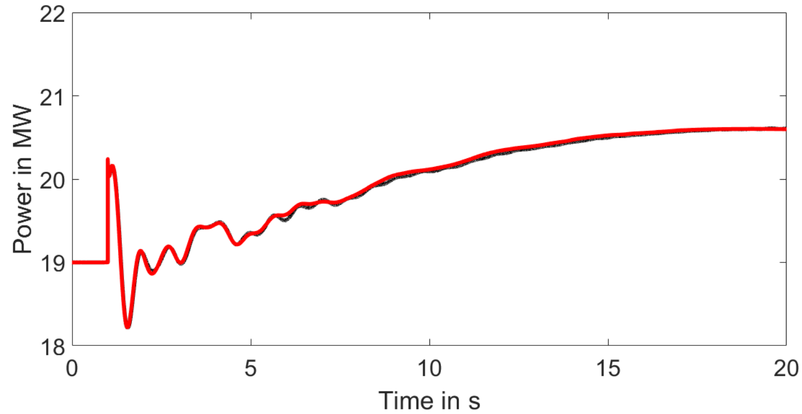


**Figure 6.3:** Generator power output when the output is in the similar region

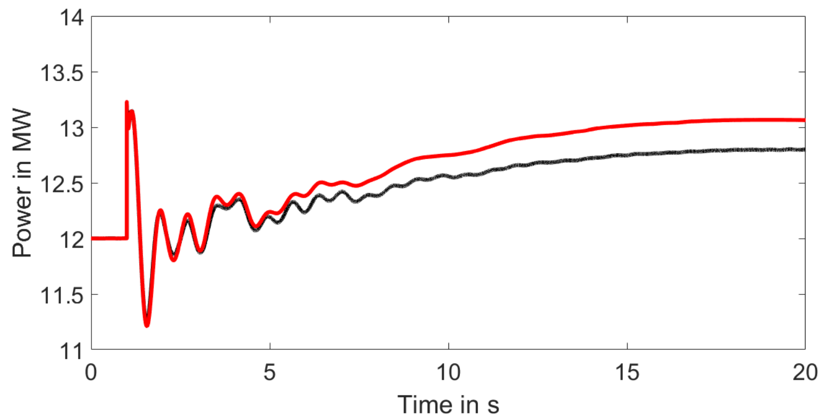


**Figure 6.4:** Generator power output when the output is in the different region

### 6.2.7 FACTS and DC Models

The data entry record for each of the FACTS and DC models had to be added manually in the dynamic file of the PSSE software.There are four DC systems present in the WECC model. These four DC models are shown in Table 6.5.

*dcmt* is a multi terminal DC model that has been developed for the IPP DC Line in the PSLF software. The control of the DC line is implemented as an EPCL program (user-defined program). As building of a user-defined model is a very cumbersome, the generic CDC6T model and its inherent control functions available in the PSS/E software have been used. The difference between the models is obvious when one of the generators close to the DC model is tripped. The frequency response and the response of the entire model is quite different.

### 6.2.8 Load Models

In the WECC case, around 6000 composite load models have been used to represent the load buses in the WECC system in detail. This is one of the most complex dynamic models that has been developed. The load models can be converted to their PSS/E equivalent using the software. However, when the models were loaded on the system they were found to make the simulation unstable. Therefore, in this case static load models are used instead.

**Table 6.5:** DC models present in the WECC system

| DC model name | Number of DC lines | Dynamic model |
|---|---|---|
| Pacific DC Intertie | 2 | epcdc |
| IPP DC Line | 2 | dcmt |
| Eastern Alberta Transmission Line | 1 | epcdc |
| Western Alberta Transmission Line | 1 | epcdc |

### 6.2.9 Relay Models

Several relay models are used in the WECC system. Considering the restrictions on the total number of constants and variables, relay models are not included as part of the dynamic model developed.

## 6.3 Simulation Results of the Conversion of WECC Model

The main purpose of developing this model is to study the frequency response of the WECC system. Therefore, several generation drop cases have been studied to ensure that the differences are acceptable. The frequency responses for generation drop cases are shown in the following figures. Considering that the focus of this work is to study the frequency response of the system, several generator drop events from different areas are simulated to assess the accuracy of the model. The results from each of the generator drops is shown here.

For the Gen 1 drop shown in Fig. 6.5, the frequency responses of the two models are very similar to each other. The nadir and frequency oscillations are almost equivalent. There is a small difference in the frequency at 20s.

In the Gen 2 drop case shown in Fig. 6.6 and Gen3 shown in Fig. 6.7, the frequency responses are very similar as well.

However, for some Gen 4 drop as shown in Fig. 6.8, the frequency response is noticeably different. This difference is basically due to the inherent differences in the modeling of the DC line. This generator drop was very close to one of the DC lines, so there is significant difference in the DC line output. As one of the DC line outputs is modeled using a user-defined model and the other is a generic model, this difference is expected.

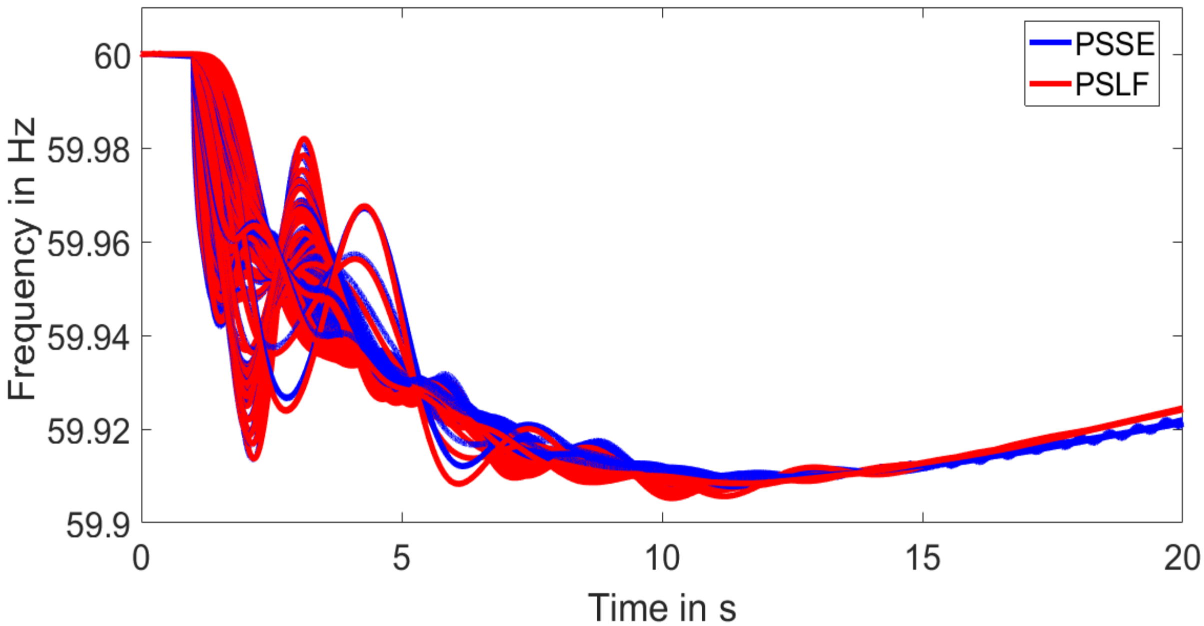


**Figure 6.5:** Comparison of the frequency response for Gen 1

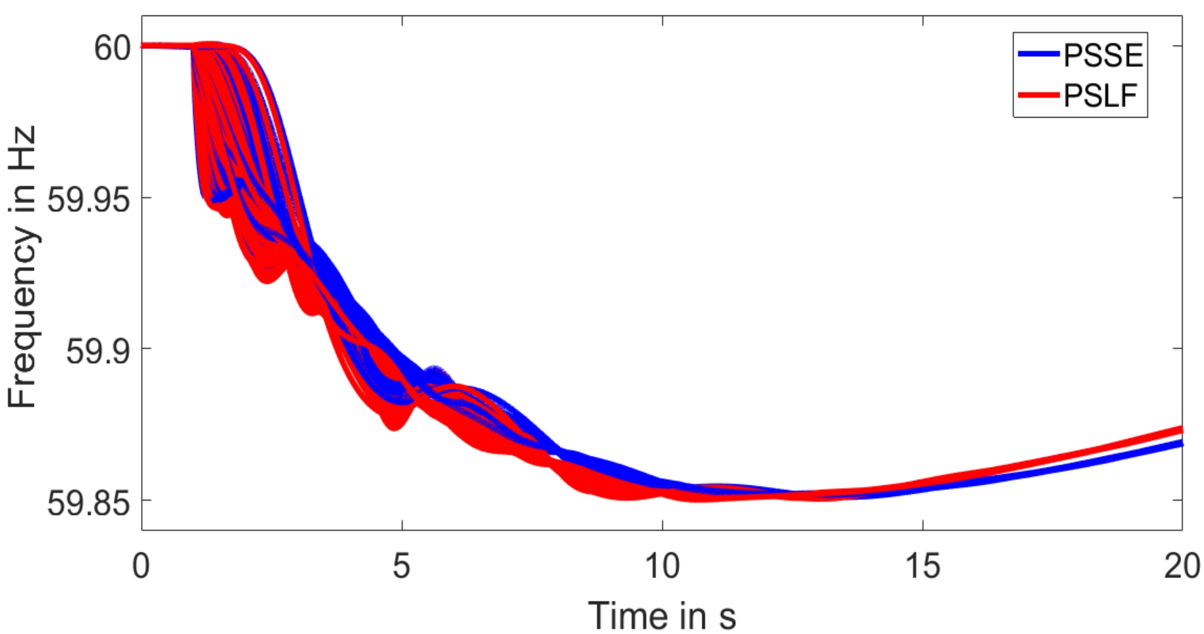


**Figure 6.6:** Comparison of the frequency response for Gen 2

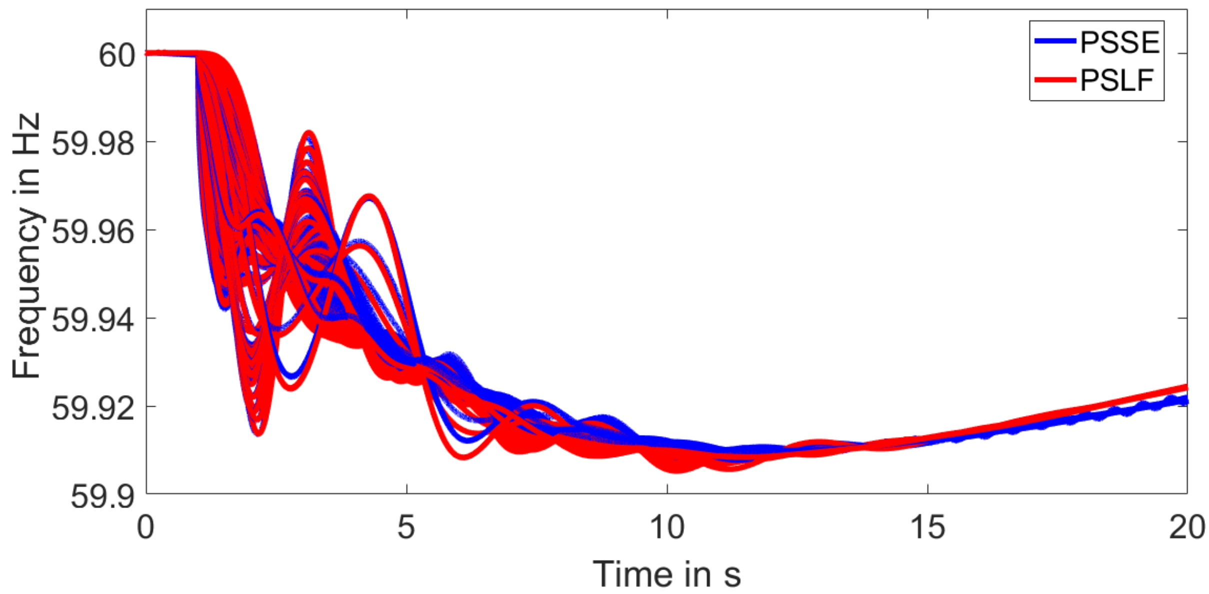


**Figure 6.7:** Comparison of the frequency response for Gen 3

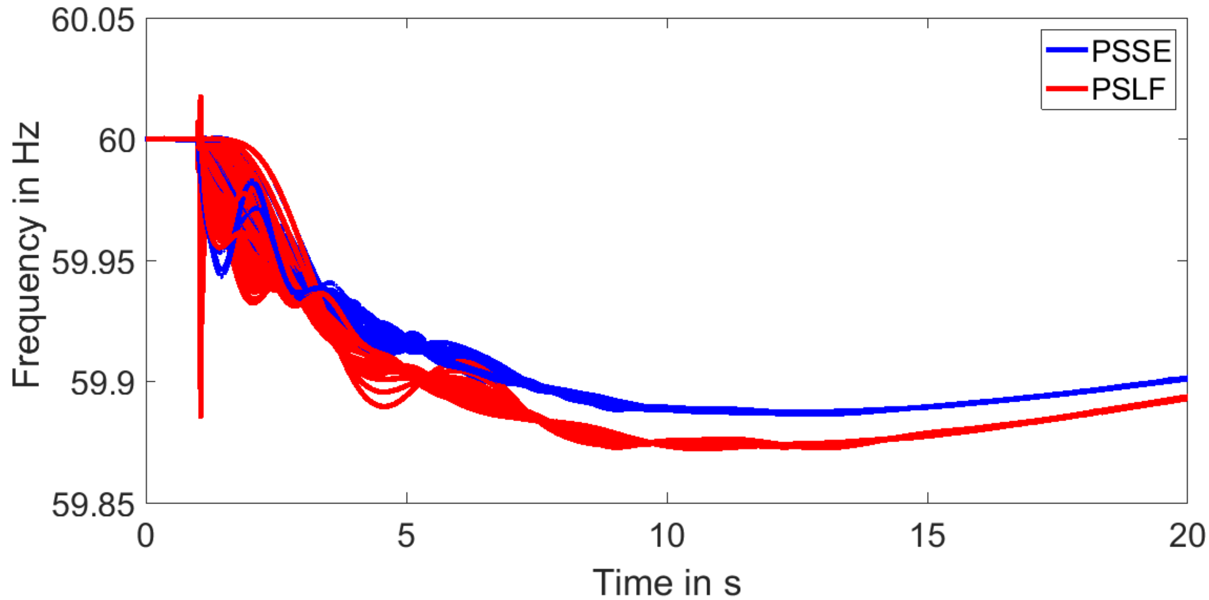


**Figure 6.8:** Comparison of the frequency response for Gen 4

## 6.4 Developing the Large-Scale Model

After the WECC PSS/E model was built, the building of the large-scale model was quite straightforward. The miscellaneous issues faced during the process of building this model are as follows:

- Renumbering the buses to ensure that no two buses are same. PSS/E has the ability to renumber the buses. Therefore, the buses, areas, zone numbers, and load adjustment data had to be modified to ensure that the values are not the same.
- Due to the limitations of the total number of variables, the relay models present in the system were disconnected.
- The back-to-back DC connections between the interconnection were previously represented as negative loads and generators. These have been replaced by generic DC models.

The details regarding the total model are shown in Table 6.6

## 6.5 Conclusions

The procedure of converting the detailed WECC PSLF model to a PSS/E model has been described in detail. The frequency response of both models for several generator drops has been shown. This model is still in development and will need additional tuning. A large-scale model with all three interconnections has been developed. This model could be used to study future scenarios and newer control schemes. The process of conversion of the WECC model

**Table 6.6:** Details of the complete model

| Detailed models | Buses | Load buses | Gen buses | Branches | Pgen (GW) |
|---|---|---|---|---|---|
| EI model | 70,117 | 38,462 | 6,746 | 83,860 | 560.12 |
| WECC model | 21,265 | 10,717 | 3247 | 26,363, | 178.74 |
| ERCOT model | 6,236 | 3636 | 626 | 7771 | 76.18 |
| Complete model | 97,618 | 52,815 | 10,619 | 117,994 | 815 |

from PSLF is discussed in the initial portion of this chapter. The accuracy of the converted static model is demonstrated. The process involved in the conversion of the dynamic model involved understanding the different component models present in the system.

# Chapter 7

# Sharing Frequency Response between Interconnections

## 7.1 Introduction

One of the threats identified to the resiliency of the system is the changing generation composition. The conventional synchronous generators are being replaced by inverter-connected resources. The impact of this change will significantly affect the inertia of the power systems and consequently the frequency stability of the entire system [36]. Therefore, the effect of increased renewables on the frequency stability of the system has received a lot of attention.

In the previous Chapter 4, the effect of reduction in inertia and load response on the frequency of the WECC system has been studied. It is obvious that with reduction in inertia, the minimum frequency reserves required will increase. Increased frequency reserve is basically the generation that cannot be utilized unless there is a contingency. The opportunity costs associated with frequency reserves will only keep increasing.

Currently in the North American system, the frequency response obligation in each of the interconnections is dependent on the resource loss protection criteria (RLPC). This is usually the largest N-2 contingency in the system. Based on the RLPC for each of the interconnection and other factors like credit for load resources, maximum allowable delta frequency the frequency response for each interconnection is decided. Currently the IFRO for each of the system is as follows [69]: Eastern Interconnection, -1,015; Western Interconnection, -858; Texas Interconnection, -381; and Quebec Interconnection, -179 MW/0.1 Hz. These obligations are fulfilled by ensuring sufficient frequency response generator headroom, appropriate governor droop and deadband values, and load shedding schemes.

However, in some areas like California that have a very high level of renewable energy penetration, they are not able to meet the FRO and need to purchase it from a neighboring balancing authority. With increased renewable energy penetration, there is a good chance this situation may be faced by entire interconnections. One of the economical and efficient possibilities is sharing frequency response between interconnections. Due to the difference in time of load peak time, and the reduced probability that all interconnections will face contingency at the same time, it is prudent to find techniques of sharing frequency response between interconnections.

Frequency response can be shared by HVDC links in cases where they are connected to asynchronous systems, large generators, AC-DC corridors, or even offshore wind resources. The extent of frequency response will depend on the nature of the interconnected systems, the additional power flow capability of the HVDC system, and the overall stability of the system [70, 71]. There are already instances like SACOI HVDC in Italy, which connects the mainland of Italy with Corsica, the additional power capability of the HVDC is utilized to ensure frequency stability of the island. In another case, in Africa, the Caprivi link (VSC HVDC) interconnects Namibian and Zambian AC systems and is used to provide additional frequency support as well. [70]. There already have been several HVDC projects that investigated frequency control functions in maintaining power grid frequency stability [71–74].

Similar studies have been conducted in North America as well. In [64], it is shown that an HVDC overlay connecting the major interconnections will be economical if the ancillary services can be shared between interconnections. Frequency control capability of VSC-HVDC links for sharing the frequency response reserves between the interconnections was investigated in [75]. In this work, only the primary frequency response sharing was studied. However, the frequency response of an interconnection has multiple stages. Primary frequency response is automatic and is responsible for stabilizing the frequency of the system after a power imbalance event. This response usually consists of the inertia response, governor response, and load response [76]. In recent years, using HVDC in primary frequency control has received much attention, and various primary frequency controllers have been proposed to increase the capability of the inertial response of HVDC links [77–80]. In some power companies, HVDC systems have actively participated in the power system primary frequency control [81–83].

Once the frequency is stabilized, there are certain governors that start withdrawing, and the primary response might not be sustained [36, 84]. If the load response or governor response is not sufficient, the frequency might have settled at a lower level, which will not change until the secondary control is activated. There is a need to ensure that after the primary control there is a correctional control that ensures the settled frequency reaches secure limits. Finally, secondary controls could be activated to restore the frequency to its nominal values. In the literature, control schemes of HVDC systems participating in AGC schemes have been discussed [85–88]. However, frequency control strategies of HVDC systems contributing to both system frequency stabilization and restoration have not received attention.

In this chapter, a multistage frequency sharing control algorithm is introduced and tested. The effectiveness of this algorithm is tested initially on the 900-bus system and later on the large-scale detailed North American model.

## 7.2 Frequency Control Strategies

In this section, the frequency control strategies of the HVDC link are presented. Fig. 7.1 shows the typical frequency response of the power system following a generator trip and the proposed HVDC frequency control functions. The three stages of frequency control in this work are as follows:

1. Primary frequency control

2. Corrective frequency control

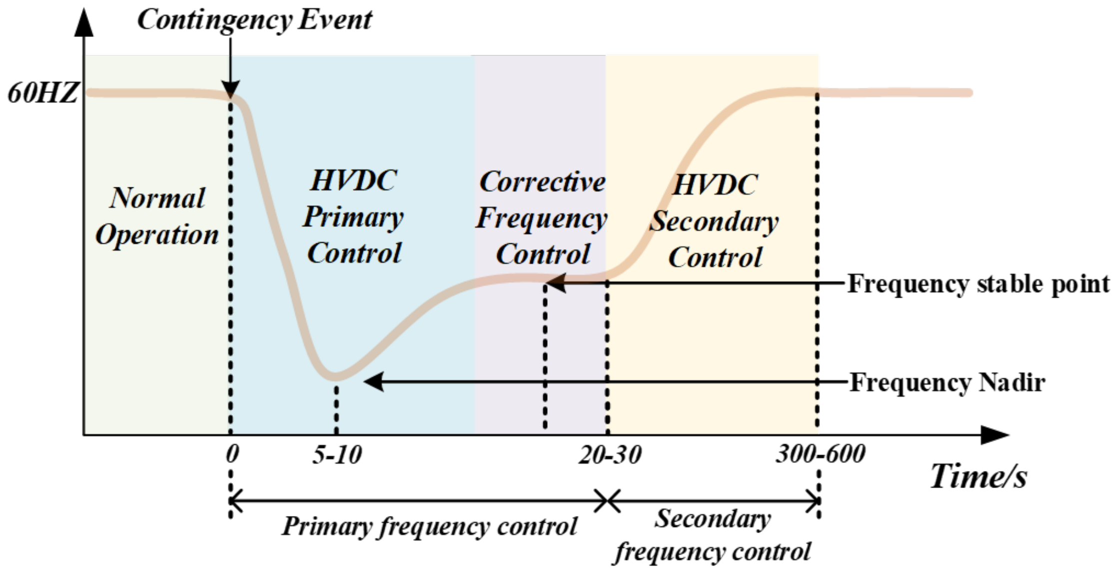


**Figure 7.1:** Typical frequency response following a generator trip

3. Secondary frequency control

The detailed description of the each of the controls is as follows:

### 7.2.1 HVDC Primary Control

HVDC primary control logic is shown in Fig. 7.2. In Fig. 7.2, $f_{ref}$ is system nominal frequency, f is system operating frequency, $f_{db}$ is frequency deviation deadband, $G_1$ is the time constant of frequency response, and $P_{max}, P_{min}$ is power transfer limit of the HVDC primary control. HVDC primary control responds to frequency deviations on either side of the HVDC link. The values of controller gains, time constants, deadbands, and power transfer limits can be specified independently for the two interconnected systems. Thus, the HVDC link could provide the desired frequency response to the AC system on one side while taking into account the emergency power support capability of the other side. This means fast frequency response is provided to the target system when a disturbance occurs, in the meantime avoiding unacceptable frequency variations in the supporting system.

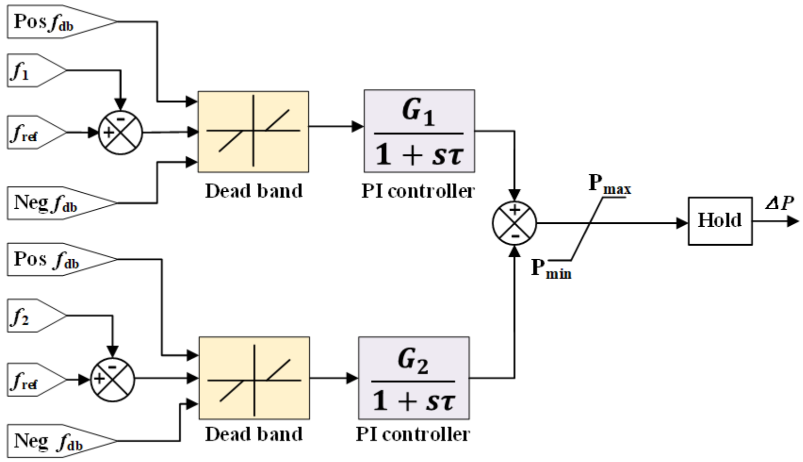


**Figure 7.2:** Primary frequency control function

### 7.2.2 Corrective Frequency Control

Fig. 7.3 shows the control logic of the corrective frequency control where $f$ and Threshold are the system operating frequency and the frequency variation targets of frequency derivative, respectively.

As shown in the upper portion of Fig. 7.3, the HVDC frequency control has a function to monitor frequency variations of the AC systems.

When the frequency variations are settled below a predefined value, the frequency control generates a signal to hold the power transfer determined by the primary control function and activates the corrective frequency control function. The corrective frequency control checks the settling frequency to see if the settling frequency is within the secure operation frequency bounds.

If the settling frequency on either side of the HVDC link is not within the secure frequency bounds, the controller adds additional corrective power $P_{safe}$ to the HVDC link control system. The corrective power $P_{safe}$ is expressed as follows:

$$\Delta P_{safe} = K_{12} * (\Delta f_1 - F_{safe1}) + K_{34} * (\Delta f_2 - F_{safe2}) \tag{7.1}$$

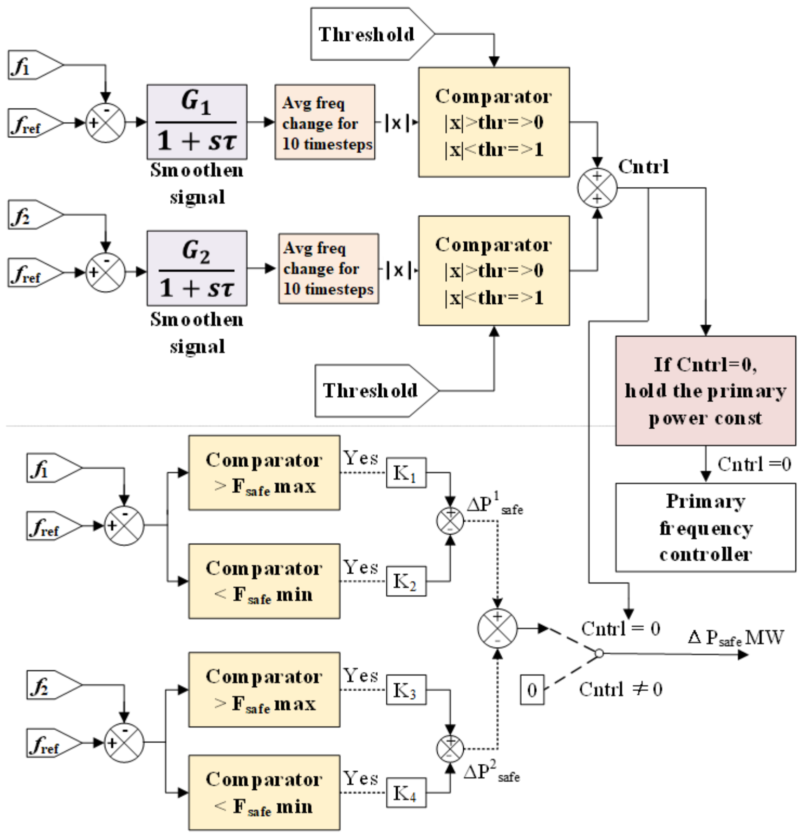


**Figure 7.3:** Corrective frequency control function

### 7.2.3 HVDC Secondary Control

The restoration of system operation frequency to its nominal frequency with the AGC process might take several minutes. During this timeframe, the system operates under off-nominal frequency conditions. In addition to the primary and corrective frequency control functions, the HVDC links between the interconnections could also participate in the AGC or the secondary frequency control for fast restoration of system nominal operating frequency.

### 7.2.4 Complete Frequency Response Controller

The flow chart of the complete frequency response controller is shown in Fig. 7.4. The frequency controller monitors the system frequencies measured at the converter stations. When a disturbance occurs in one system, abnormal frequency is detected. The primary control is activated to provide fast frequency response support if the frequency deviation is higher than the preset bandwidth. After the frequency of the disturbed system is stabilized,

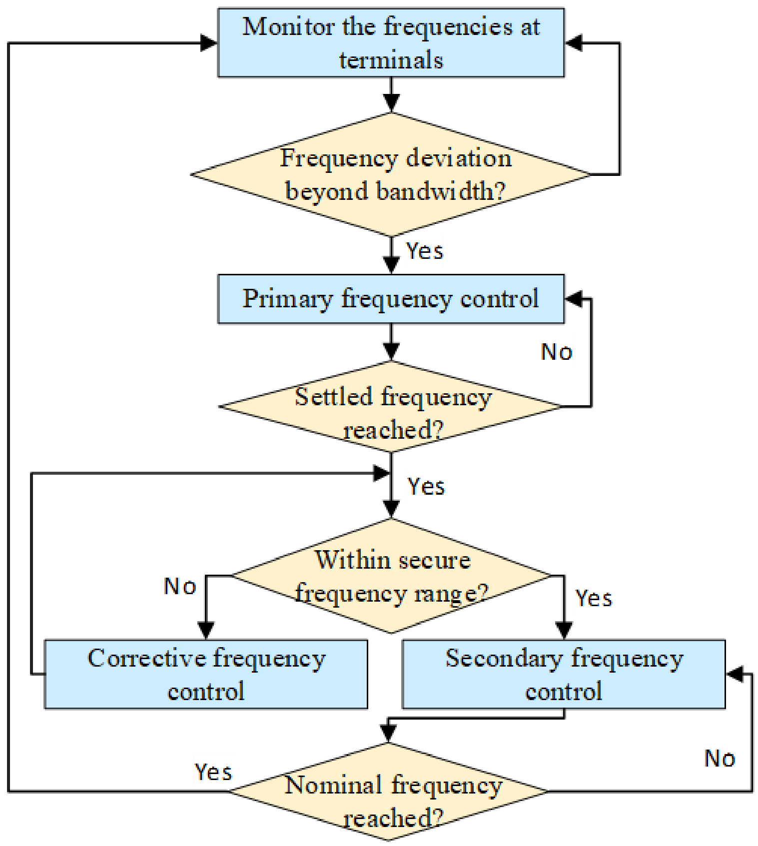


**Figure 7.4:** The flowchart of the frequency response control

the settling frequency is examined. If the settling frequency is not within the bounds of a secure system operating frequency, the corrective frequency control is activated to provide additional support to establish a secure system operating frequency. If the HVDC link participates in the secondary frequency control, it adjusts the power flow according to the pre-defined adjustment coefficients.

## 7.3 Study System and Model Description

This study is initially conducted on a smaller power system of the North American system. The details of the model are discussed first. A more detailed model with a 90,000-bus system developed in Chapter 6 has been modified to facilitate the sharing of frequency response between the interconnections using HVDC.

### 7.3.1 900-Bus Power System Model

#### Power System Model

Initially, the study system used is a reduced model of the North American system [89]. The reduced EI system has 459 buses, and the reduced WECC and the ERCOT systems have 191 buses and 280 buses respectively. In the reduced system model, the frequency responses of the systems are preserved, and the power flows in major transmission corridors are maintained [89]. In this study, three VSC-HVDC links are included for connecting the three asynchronous systems. The capacity of the VSC-HVDC link is rated at 1200 MW each, and the operating DC voltage of the HVDC link is 320 kV.

#### VSC-HVDC Model Description

The HVDC Light model as shown in Fig. 7.5 (reproduced from [90]) is used for modeling the HVDC systems in the PSS/E software [90]. The HVDC Light model is a user-defined model for power system planning study. The necessary control functions are configured and have been validated against detailed VSC-HVDC system models. In the HVDC Light model, each HVDC station is represented by four components: the AC transformer, the filters, the phase reactor, and the converter.

As shown in Fig. 7.5 (reproduced from [90]), the control functions of the HVDC Light converter include AC and DC voltage control, active and reactive power control, and inner current control. The control system recognizes current output limitation and internal converter voltage limitations. Fig. 7.5 also shows the reference inputs and the corrective inputs. For a two-terminal VSC-HVDC link, one of the converters controls DC voltage ($U_{dcref}$) and the other active power ($P_{ref}$). Each of the converters can be independently set as an AC voltage control mode ($U_{acref}$) or reactive power control mode ($Q_{ref}$). In normal operations, the power order and voltage setting points of the HVDC converters are determined by the system operator. The auxiliary inputs come from application-level controllers and can be used for active and reactive power modulation to achieve desired frequency response control, power oscillation damping control, and voltage stability enhancement.

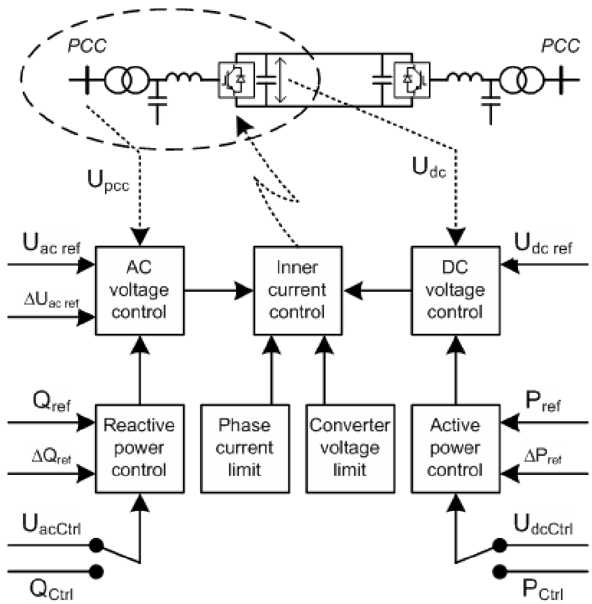


**Figure 7.5:** The principal control scheme of HVDC Light

### Frequency Response Control Model Description

The frequency control strategies described are implemented as a user-defined model that provides auxiliary active power control signals to the HVDC Light controller. Fig. 7.4 shows the flowchart of the frequency response control.

Table 7.1shows the main parameters of the frequency controller, including control gains, deadbands, and power limits in both directions for the three HVDC links. The time constant of the primary frequency response is 2ms.

**Table 7.1:** Parameters of the frequency response control

| HVDC link | Terminal | Control gain | Deadband (Hz) | Power limit (MW) |
|---|---|---|---|---|
| WECC to ERCOT | WECC | 2500 | 0.05 | 600 |
| WECC to ERCOT | ERCOT | 2500 | 0.1 | 500 |
| WECC to EI | WECC | 12000 | 0.05 | 500 |
| WECC to EI | EI | 12000 | 0.05 | 700 |
| EI to ERCOT | EI | 4000 | 0.05 | 500 |
| EI to ERCOT | ERCOT | 4000 | 0.1 | 750 |

### 7.3.2 Detailed Model Description

The detailed dynamic model of each interconnection is updated every year to ensure that it represents the real system accurately. The Eastern Interconnection model is developed and maintained by the multi-regional modeling working group (MMWG) of the Eastern Interconnection Reliability Assessment Group (ERAG).

The WECC System Review Work Group (SRWG) consolidates and updates the WECC planning models. This model is reviewed and approved by all of its utility members. It is the second largest interconnection. Apart from the 3000 detailed generator plant models and the detailed HVDC models, around 6000 load models present in the WECC system are represented by using the detailed composite load model. ERCOT is responsible for over 85% of Texas. They develop and update the Texas model, which consists of over 6000 buses.

These interconnections are connected to each other through back-to-back DC connections. In order to test the frequency response sharing between the interconnections, VSC-HVDC models have been added between the interconnections as shown in Fig. 7.6. The power transfer in any interconnection is represented by either a generator or a negative load.

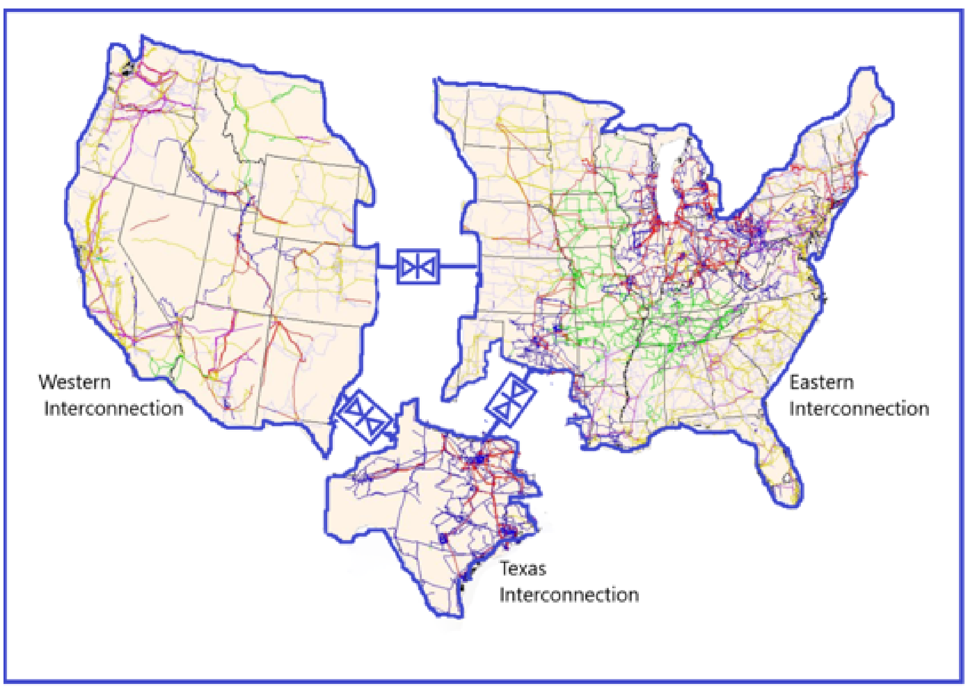


**Figure 7.6:** Detailed North American model with VSC HVDC

There are multiple difficulties in developing a large-scale model. The first difficulty was that the sheer size of this intercontinental model would be over 90,000 buses. Though the software could model larger bus sizes in a static model, with the full dynamic model included, the size of the constants and variables and other parameters would exceed the limits.

Several user-defined models have been developed specifically for each interconnection in a particular software and have to be represented by generic models, as developing user-defined models is difficult. For this work, the detailed North American model has been developed to demonstrate the frequency sharing across interconnections accurately.

The initial part of the work involved converting the WECC PSLF model into a PSS/E model. Owing to the limitation on the size of arrays, the WECC load models are changed to be static models. They have been validated for frequency response considering many scenarios. The results of one of the tests of the frequency response of the system is shown in Fig. The other two models were already available in PSS/E software and the same models have been used. The details of the continental model are shown as follows:

The VSC model used is the generic VSC-HVDC model that is present in the PSS/E software. A user-defined auxiliary control model has been developed using the USRVSW model present in the PSS/E model that controls the additional power that needs to be transferred between the system. The parameters for this frequency response controller are shown in Table 7.2. The parameters are tuned for this model.

**Table 7.2:** Parameters of the frequency response control (Detailed system)

| HVDC link | Terminal | Control gain | Deadband (Hz) | Power limit (MW) |
|---|---|---|---|---|
| WECC to ERCOT | WECC | 4000 | 0.05 | 600 |
| WECC to ERCOT | ERCOT | 3000 | 0.075 | 600 |
| WECC to EI | WECC | 12000 | 0.05 | 500 |
| WECC to EI | EI | 12000 | 0.05 | 700 |
| EI to ERCOT | EI | 5000 | 0.05 | 400 |
| EI to ERCOT | ERCOT | 5000 | 0.1 | 1200 |

## 7.4 Simulation Results and Discussion

Initially, frequency sharing among interconnections is demonstrated using the simplified model of the North American system. Scenarios with generator outages in both the ERCOT and WECC systems are developed. Apart from the primary and critical frequency control, the possibility of secondary frequency control (AGC control) is demonstrated using the 900-bus system. Next, the performance of the frequency controller is investigated for critical generator outages using the detailed model.

### 7.4.1 Simulation Results using the 900-Bus Model

#### One Generator Trip in the ERCOT System

In this case, a large generator (1928 MW) is tripped in ERCOT. Fig. 7.7 shows the frequency responses of the three interconnections. In the base case, the frequency nadir in ERCOT is 59.6 Hz. With the primary frequency response support from EI and WECC, the nadir is improved by almost 0.15 Hz. The frequency deviations in EI and WECC remain above 59.5 Hz. After the frequency in ERCOT is settled, it is observed that the settling frequency in ERCOT is not within the secure frequency bounds (determined as 9.9 Hz). Thus, the corrective frequency control function is activated, and the system operates at improved settling frequency.

Fig. 7.8 shows the active power flows through the HVDC links. It can be seen that the directions of the power flows are reversed almost instantly with the fast primary frequency control in the two HVDC links connecting ERCOT to EI and ERCOT to WECC. During primary frequency control, the power flow from EI to ERCOT is increased by 800 MW and the power flow from WECC to ERCOT is increased by 380 MW. The increased HVDC power flows will not ramp down after the initial settling frequency established. Since the initial settling frequency is not within the secure system frequency bound, 59.9 Hz for this study, the corrective frequency control is activated, and the power flows of the HVDC links are further increased, moving more power from EI and WECC into the ERCOT system until secure settling frequency is established in the ERCOT system.

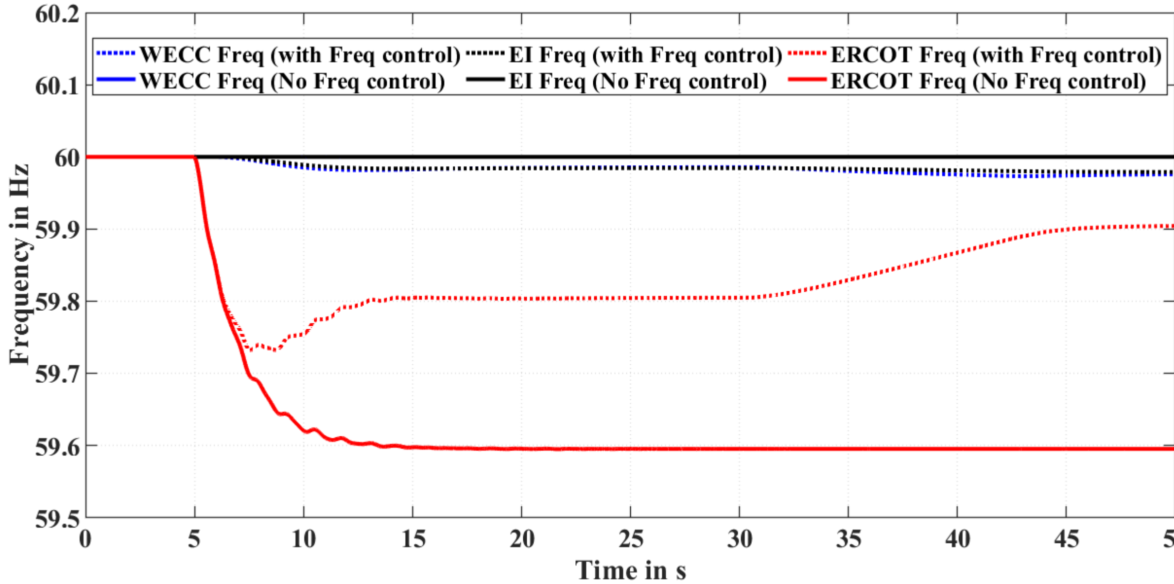


**Figure 7.7:** Frequency responses of WECC, ERCOT, and EI (ERCOT one gen trip using simple model)

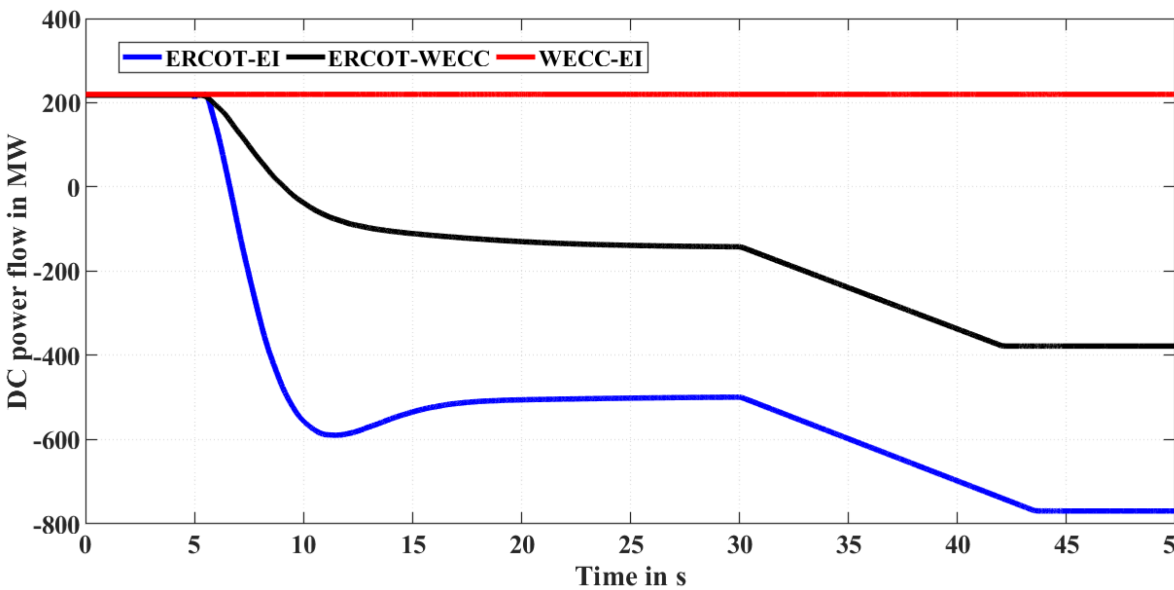


**Figure 7.8:** Power flows in HVDC links (ERCOT one gen trip using simple model)

### One Generator Trip in the WECC System

In this case, a large power plant (2640 MW) is tripped in the WECC system. The frequency responses of the three interconnects are shown in Fig. 7.9. With the primary frequency control, the frequency nadir of WECC is improved by 0.03 Hz. The frequency in the ERCOT system is more affected than the EI system due to its relatively small size. However, the frequency controller is tuned to ensure that the contribution from ERCOT would much lesser than from the EI system.

The power flows in the HVDC links are shown in Fig. 7.10. The power flow from ERCOT to WECC is increased from 200MW to 400MW, and the power flow from WECC to EI is reversed from 200MW (WECC to EI) to 500MW (EI to WECC). In this case, the corrective frequency control is not needed. To demonstrate the effectiveness of the control, a higher secure frequency is set for the WECC system. Thus, the power flow from EI to WECC is further increased to 750 MW by the corrective frequency control. There is no further contribution from ERCOT as the power transfer limit is set at 500MW (ERCOT to WECC) for the frequency response support.

### Two generators trip in the ERCOT system

In this case, two generators (3055 MW in total) are tripped in the ERCOT system. As shown in Fig. 7.11, the settling frequency is quite low without frequency response support of the HVDC links. With the frequency response support of the HVDC links, the frequency nadir of ERCOT is improved by 0.3 Hz, and the settling frequency (59.7 Hz) is reached. Fig. 7.12 shows the power flows of the HVDC links. The power flow directions of the WECC-EI and ERCOT-WECC HVDC links are both reversed. Due to the pre-set transfer limits for frequency support, the power flows of WECC-ERCOT and EI-ERCOT are capped at 500MW and 750MW respectively. It should be pointed out that the power transfer limits for the provision of frequency support could be increased up to the rated HVDC link capacity.

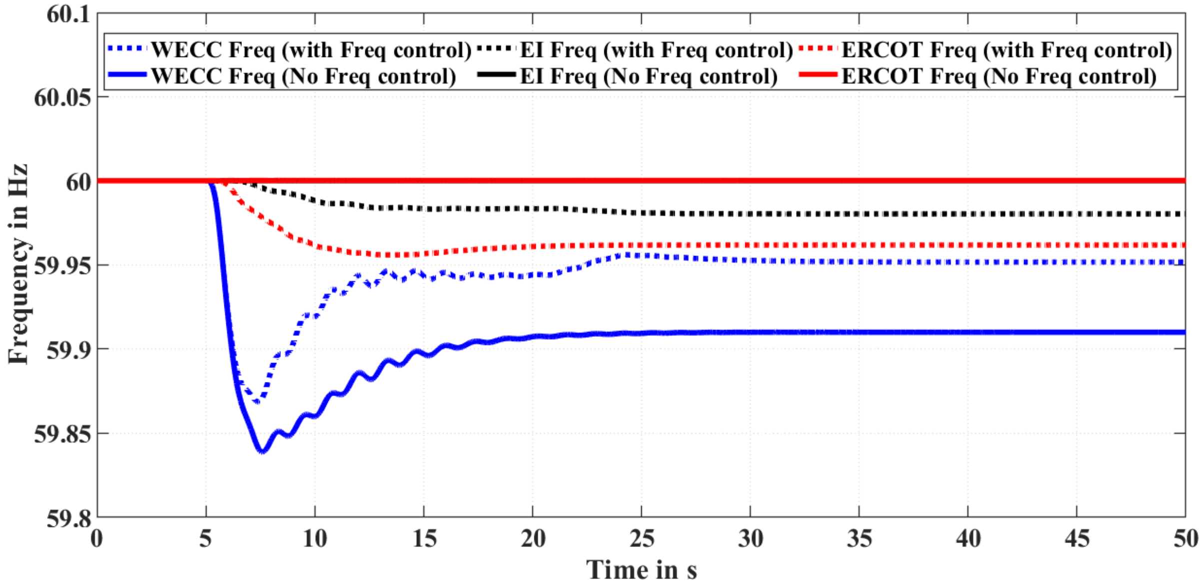


**Figure 7.9:** Frequency response of WECC, ERCOT, and EI (WECC one gen trip using simple model)

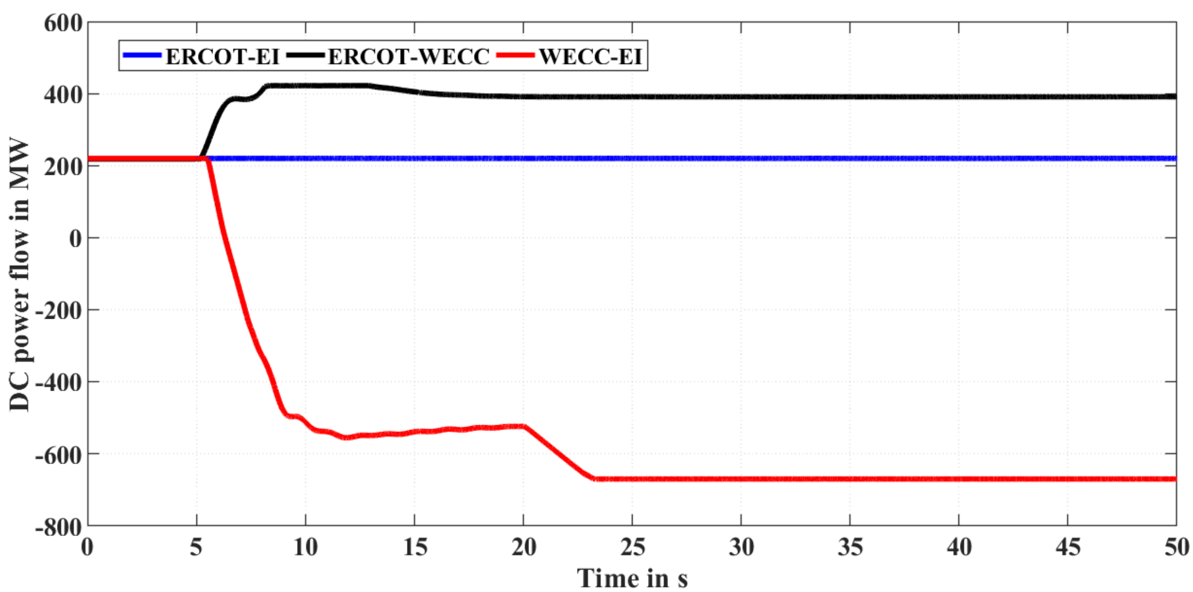


**Figure 7.10:** Power flow in HVDC links (WECC one gen trip using simple model)

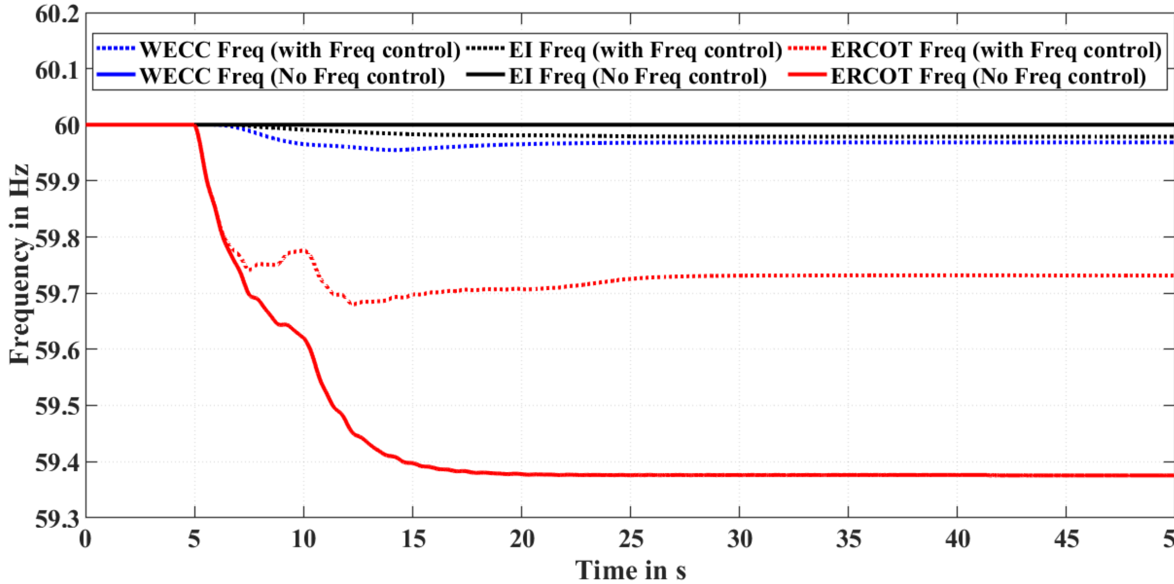


**Figure 7.11:** Frequency responses of WECC, ERCOT, and EI (ERCOT two gen trip using simple model)

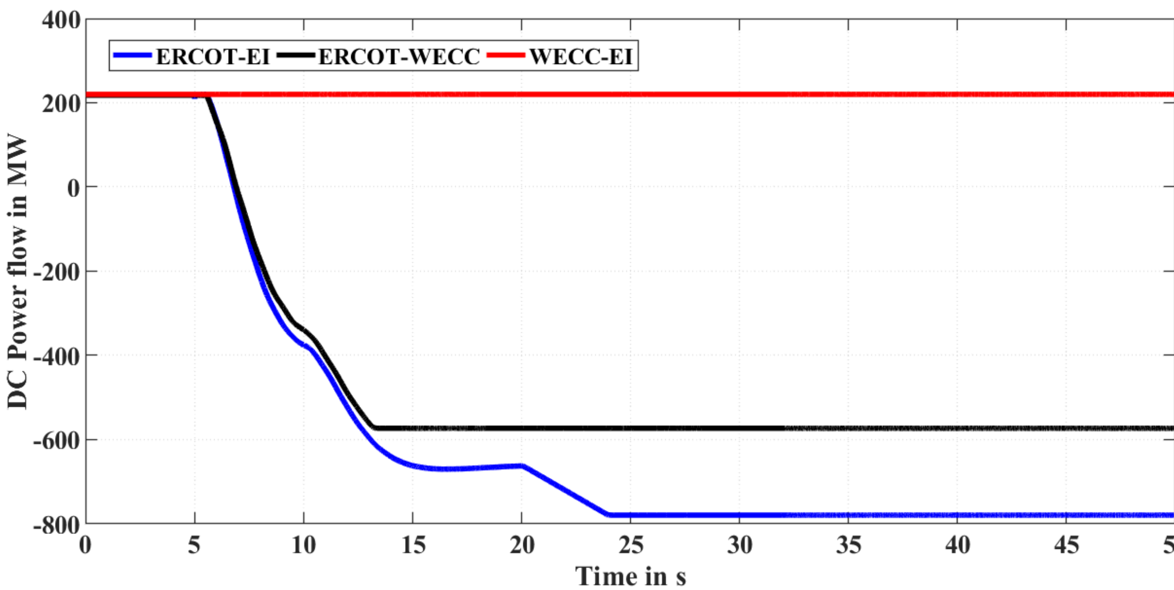


**Figure 7.12:** Power flows in HVDC links (ERCOT two gen trip using simple model)

### Secondary frequency response of HVDC Links

In the case, the HVDC links participate the power system secondary frequency control. Apart from the primary frequency control, the power flows of the HVDC links can re-dispatched together with the frequency regulating generators by the AGC system of the grid control center based on the pre-determined adjustment coefficients. A large generator (1928 MW) is tripped in ERCOT. Fig. 7.13 shows the three different stages of frequency responses of the ERCOT with the frequency support of HVDC links. Fig. 7.14 shows the power flows in the HVDC links.

As expected, the frequency response of ERCOT and the power flow changes of HVDC links during the power system primary frequency response timeframe are the same as the simulation results shown in Figs. 7.7 and 7.8. After the AGC control is activated, the HVDC link will be re-dispatched for further increased power support to the disturbed system.

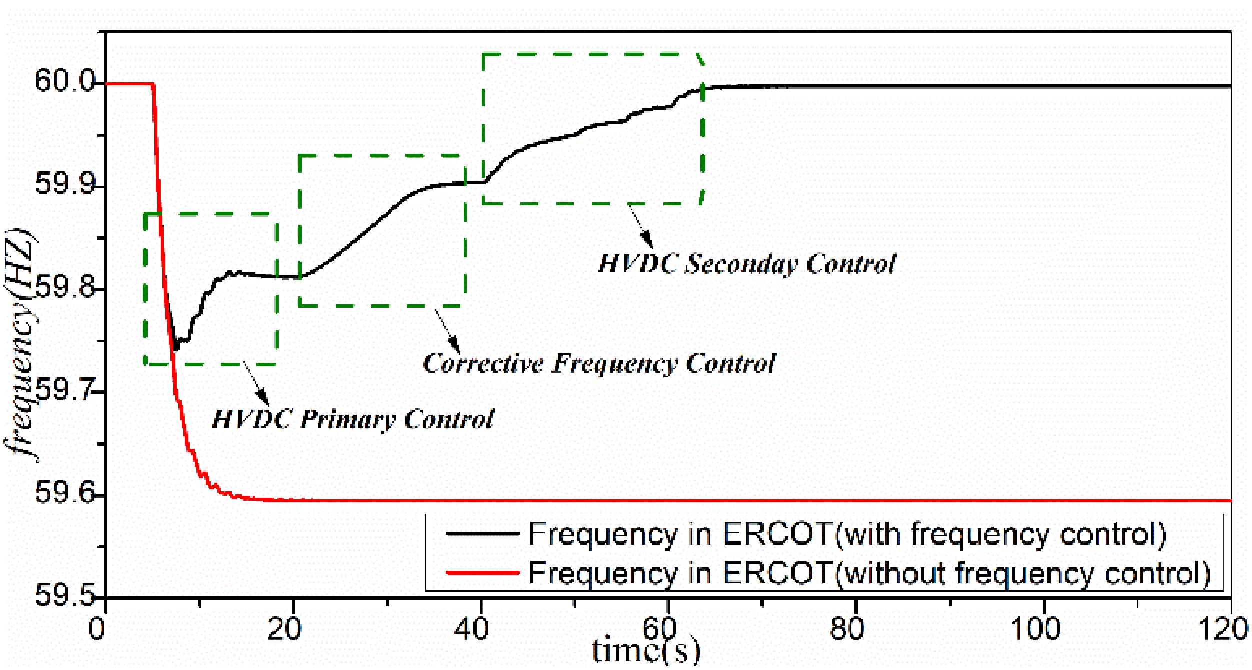


**Figure 7.13:** Multi-step frequency response (simple model)

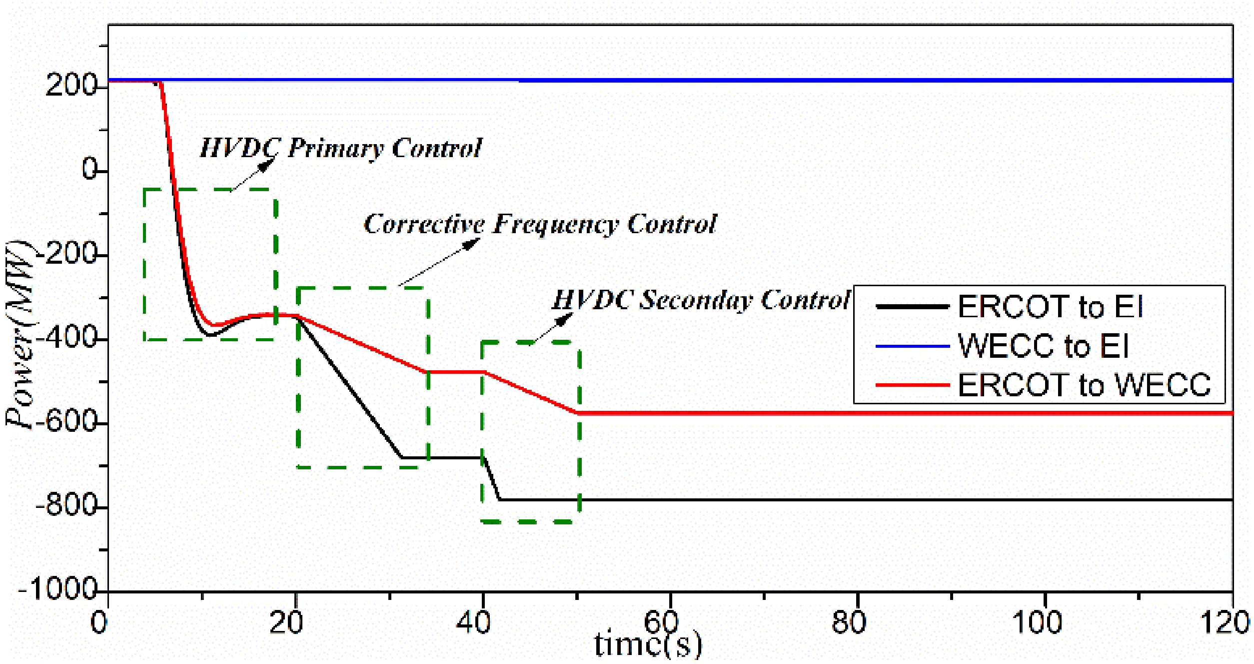


**Figure 7.14:** The multi-step power increase in HVDC power (simple model)

In this study, the frequency response support to ERCOT from EI and WECC are limited to 750 MW and 600 MW. After that, the frequency regulating generators in ERCOT will eventually restore the operating frequency to the nominal system frequency. It is definitely feasible to increase the frequency response support up to the rated HVDC link power capacity.

### 7.4.2 Simulation Results with Detailed Model

The following scenarios have been developed to demonstrate the performance of the frequency response controller using the detailed model. Even though the simplified 900-bus model preserves power flow and generation profile, there might be some other issues that might arise when the detailed model is used. Therefore the following simulations are conducted to test the controller. Initially the effectiveness of frequency primary control is demonstrated with the following scenarios.

### One Generation Trip in the ERCOT System

A generator supplying 724 MW of generation is disconnected in ERCOT. The three frequency response–sharing cases are compared. This scenario demonstrates the difference in frequency response of the ERCOT system when frequency response is provided by both interconnections. As can be seen from Fig. 7.15, without any additional frequency support, the nadir is around 59.84 Hz. When both WECC and EI provide frequency support to the system, the frequency response of ERCOT improves slightly and the nadir is around 59.94 Hz. However, in this scenario, the frequency of EI and WECC interconnections settles above 59.98 Hz.

The power flow between the EI and ERCOT interconnection is shown in Fig. 7.16. When both EI and WECC respond to the generator drop in ERCOT, the maximum power flowing from EI is around 500 MW and the maximum power from WECC is around 400 MW of power flow.

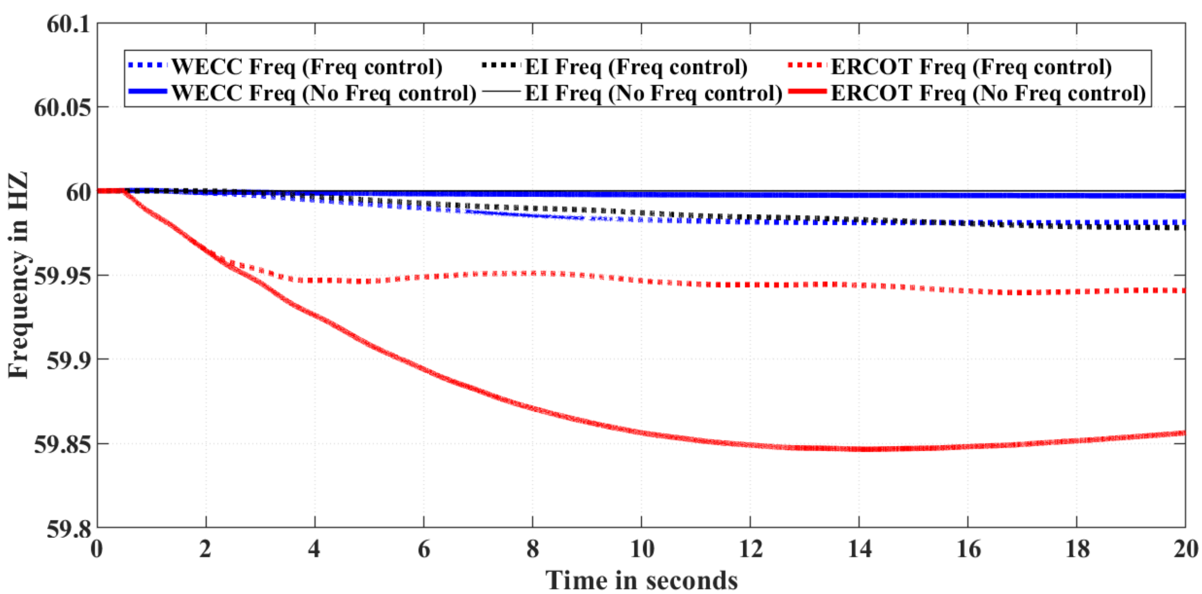


**Figure 7.15:** Frequency responses of WECC, ERCOT, and EI (ERCOT one gen trip using detailed model)

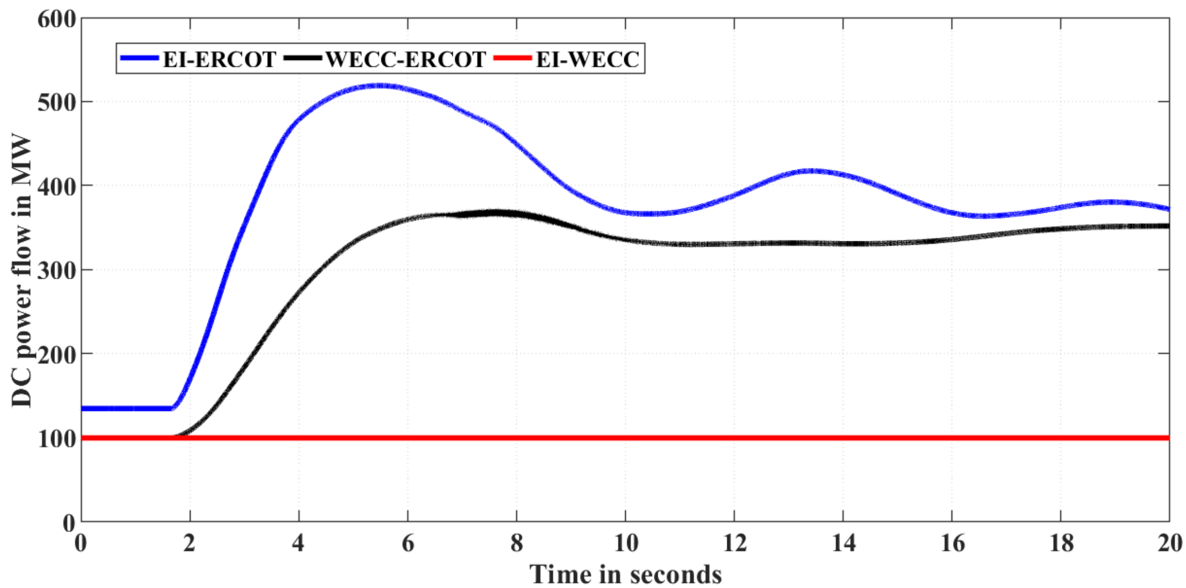


**Figure 7.16:** Power flow in the HVDC links (ERCOT one gen trip using detailed model)

### Two Generators Trip in the WECC System

In order to test frequency support to the WECC interconnection from the other two interconnections, two Palo Verde generation drop amounting to almost 2700 MW in generation drop is simulated. Three scenarios similar to the previous case, the frequency responses of the three interconnections, are shown in Fig. 7.17. The power flow from the EI and ERCOT systems is shown in Fig. 7.18. The nadir when no additional support is provided to WECC is around 59.825 Hz. The frequency response of the system improves significantly to 59.89 Hz when both EI and ERCOT provide additional support. During this time, the frequency of the EI system remains above 59.95 Hz and the frequency response of ERCOT remains above 59.9 Hz.

The power from the EI system reaches a maximum value of 900 MW. In this scenario, the initial power flow direction is actually from WECC to ERCOT. In this scenario, the power flow has to be reversed so that around 150 MW of power can be transferred from ERCOT to WECC. Therefore, the total change in power is around 350 MW of power.

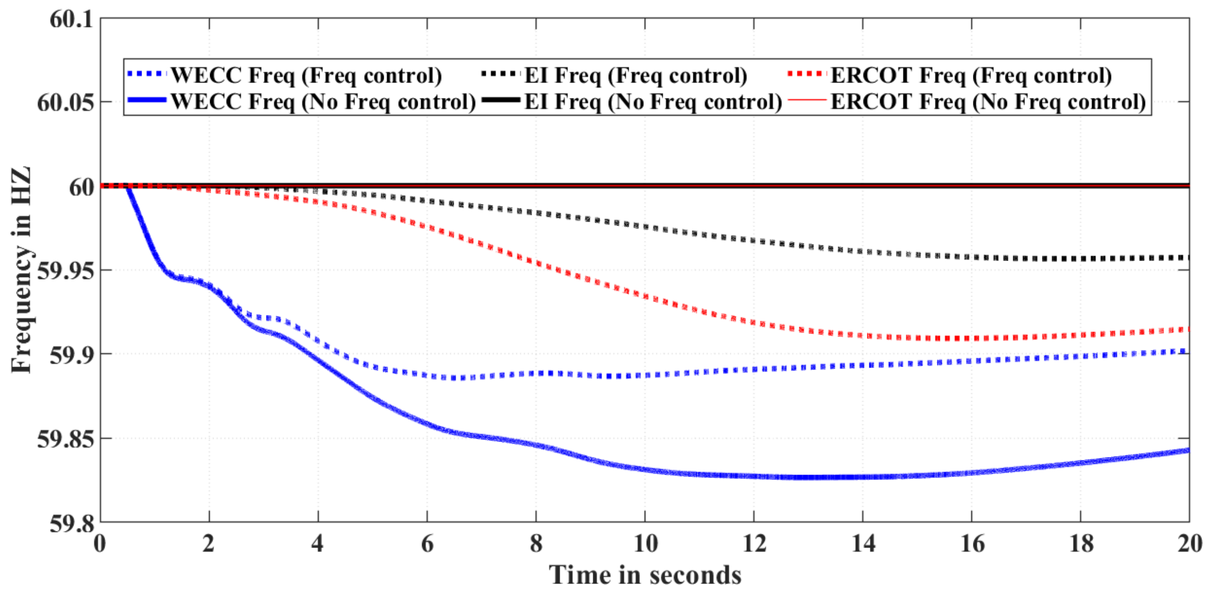


**Figure 7.17:** Frequency responses of WECC, ERCOT, and EI (WECC two gen trip using detailed model)

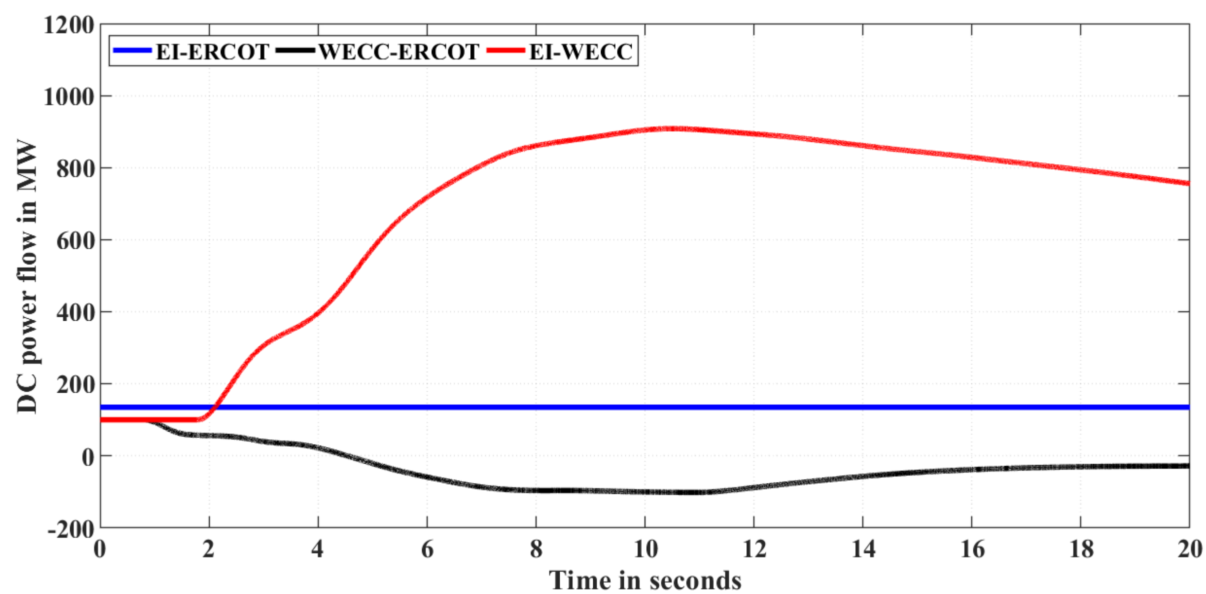


**Figure 7.18:** Power flow in HVDC lines (WECC two gen trip using detailed model)

### Two Generators Trip in the ERCOT System

Among the possible contingencies in ERCOT, a double generation drop leading to a loss of 2400 MW is the most severe. For this contingency, load loss will be initiated in order to maintain the stability. In this scenario, when no additional frequency support was provided, the system becomes unstable. The frequency response is shown in Fig. 7.19. With additional frequency support, the system becomes stable. The nadir of the ERCOT interconnection is around 59.65 Hz. The power flow from each of the interconnection is shown in Fig. 7.20.

With only primary control, the system becomes stable. However, the settling frequency is around 59.7 Hz, which might harm different components if this frequency persists in the system. Therefore, if there isn't sufficient sustained frequency support, additional frequency support can be provided by other systems. The response of ERCOT is shown in Fig. 7.21. The settling frequency is now around 59.82 Hz. The power flow in the HVDC system is shown in Fig. 7.22. After the settling frequency is seen to fall below the secure limits, the HVDC power flow from each of the interconnections is increased at a constant ramp rate. The power flow from EI to ERCOT is increased to 1200 MW (maximum limit) and the power flow from WECC to ERCOT reaches 400 MW.

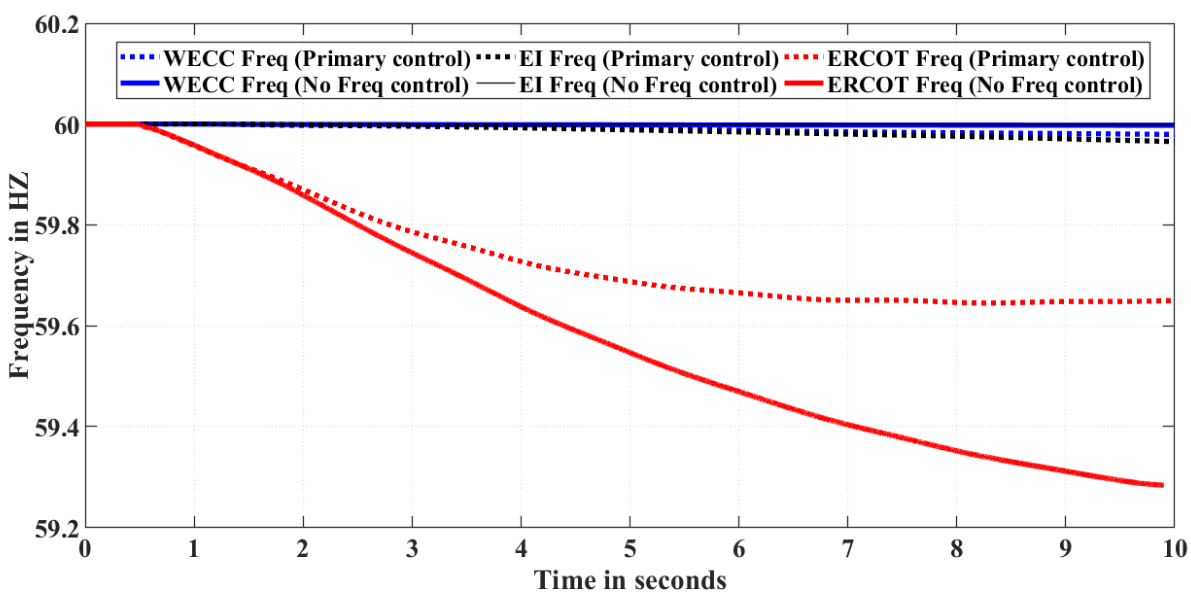


**Figure 7.19:** Frequency responses of WECC, ERCOT, and EI (ERCOT two gen trip using detailed model)

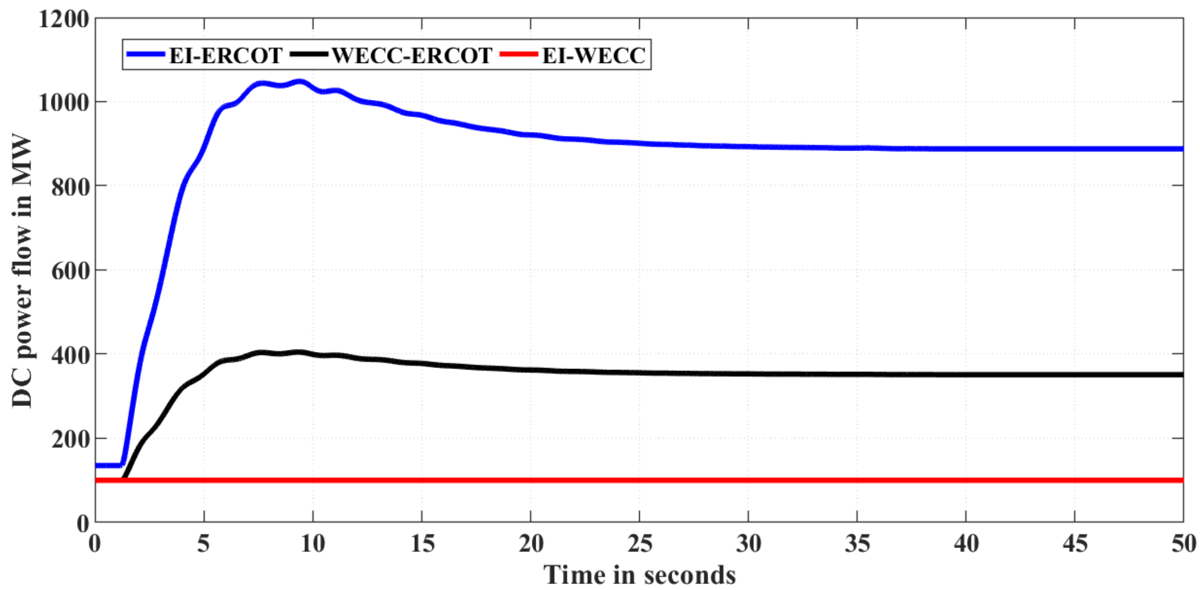


**Figure 7.20:** Power flow in HVDC lines (ERCOT two gen trip using detailed model)

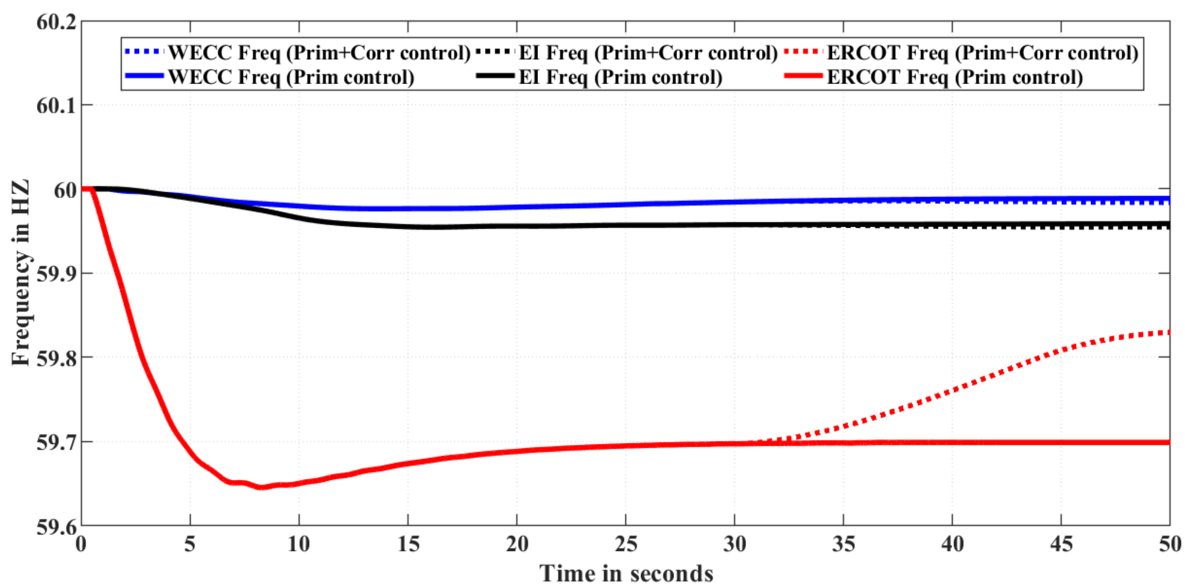


**Figure 7.21:** Multi-step frequency responses in the ERCOT system (detailed model)

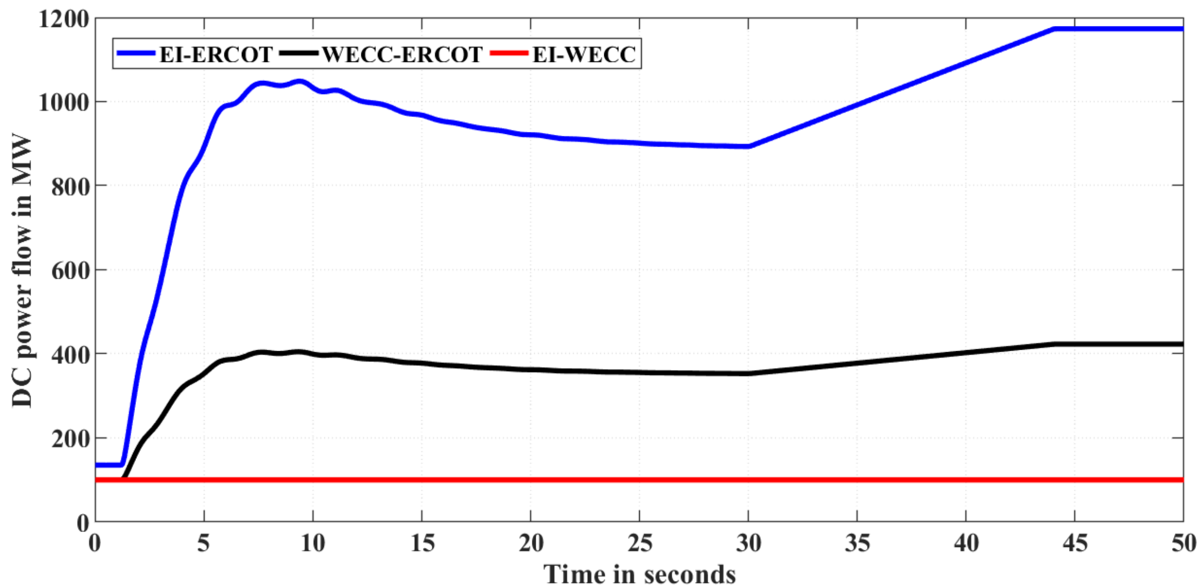


**Figure 7.22:** The multi-step power increase in HVDC lines (detailed model)

## 7.5 Conclusions

A novel frequency controller for HVDC links is proposed for sharing the responsive reserves of the interconnected power systems. The proposed frequency controller can provide fast frequency response for stabilizing the frequency of the disturbed power grid and corrective frequency control for establishing a secure settling frequency. The HVDC links can also participate in the system secondary frequency response as for restoration of system frequency back to its nominal operating frequency.

The test studies are based on a reduced North American grid model with the three interconnections (EI, WECC, and ERCOT) interconnected by respective VSC-HVDC links. The test cases show improved frequency responses, especially for the ERCOT system under critical generator outages. Further studies are to investigate the frequency support capability of HVDC links such as inertial response, fast frequency response, primary frequency response, etc. as required by the ancillary service markets.

# Chapter 8

# Conclusion and Future Work

With the rapidly changing nature of power systems, the challenges of operating them reliably have definitely increased. However, with advancements in measurement technology, simulation tools and techniques, and increased knowledge of the system, there are new avenues opening up to ensure that the power system is operated more reliably and more efficiently and also using cleaner resources. In this work, several challenges related to reliable operation of the bulk electric system has been studied in detail. A detailed analysis of the possible mitigation and its adverse effects have also been studied. Depending on the objective of the analysis, the appropriate tools and techniques have been used to further analyze the system. In the first part of the system, the effect of momentary cessation on the frequency response of WECC system has been studied in detail. Considering the lack of sufficient information, an estimation regarding the actual resources that went into momentary cessation has been done. It also highlights the fact that distribution level generators have now started to affect the bulk electric system. One of the challenges of this phenomenon has been that the exact amount of generation trip could not be assessed. In Chapter 3, a new ROCOF-based algorithm has been tested on the WECC system to determine the generation trip. This method seems to be promising, but future use of artificial intelligence algorithms will improve its accuracy further. In Chapter 4, the influence of load modeling on frequency response of the system has been assessed. In the Chapter 5, the possibility of using short-term overloading capability of HVDC to improve the first swing stability limit of the WECC system has been studied. As this affects the stability of the entire region, wide area simulation is done to study its impact. The increase in stability limit is shown for the cases tested. In Chapter 6, the process of development of a continent-wide power system model is discussed. In Chapter 7, frequency response sharing between the interconnections is proposed and discussed.

Based on the work so far, it is assessed that changing resource mix is a more urgent and important concern that could affect the reliable operation of the power system. Therefore, in the future, the plan is to study effects on the large power system. With changing resource mix, the need to study the adequacy of the frequency response with deteriorating inertia will be studied in detail in future.

# Bibliography

[1] R. I. steering committee, “Report on resilience,” tech. rep., NERC, November 2018. 1

[2] R. E. P. N. for the 21st Century, “Renewables 2019 global status report,” tech. rep., 2019. 3

[3] T. Hodge, “Eia forecasts natural gas to remain primary energy source for electricity generation,” 2019. 3

[4] Y. Liu, S. You, J. Tan, Y. Zhang, and Y. Liu, “Frequency response assessment and enhancement of the u.s. power grids toward extra-high photovoltaic generation penetrations—an industry perspective,” *IEEE Transactions on Power Systems*, vol. 33, pp. 3438–3449, May 2018. 6, 42

[5] J. Tan, Y. Zhang, S. Veda, T. Elgindy, and Y. Liu, “Developing high pv penetration cases for frequency response study of u.s. western interconnection,” in *2017 Ninth Annual IEEE Green Technologies Conference (GreenTech)*, pp. 304–311, March 2017. 42

[6] G. Kou, P. Markham, S. Hadley, T. King, and Y. Liu, “Impact of governor deadband on frequency response of the u.s. eastern interconnection,” *IEEE Transactions on Smart Grid*, vol. 7, pp. 1368–1377, May 2016. 6

[7] K. S. Shetye, W. Jang, and T. J. Overbye, “System dynamic model validation using real-time models and pmu data,” in *2018 Clemson University Power Systems Conference (PSC)*, pp. 1–7, Sep. 2018. 6

[8] A. G. Phadke, “Synchronized phasor measurements in power systems,” *IEEE Computer Applications in Power*, vol. 6, pp. 10–15, April 1993. 8

[9] Yong Liu, Shutang You, and Yilu Liu, *Communication, Control and Security Challenges for the Smart Grid*. Energy Engineering, Institution of Engineering and Technology, 2017.

[10] Y. Liu, Y. Cui, W. Yu, Y. Zhang, L. Wu, S. You, and Y. Liu, “Recent application examples of fnet/grideye,” in *2018 IEEE 12th International Conference on*

*Compatibility, Power Electronics and Power Engineering (CPE-POWERENG 2018)*, pp. 1–6, April 2018. 8

[11] Bin Qiu, Ling Chen, V. Centeno, Xuzhu Dong, and Yilu Liu, "Internet based frequency monitoring network (fnet)," in *2001 IEEE Power Engineering Society Winter Meeting. Conference Proceedings (Cat. No.01CH37194)*, vol. 3, pp. 1166–1171 vol.3, Jan 2001. 8

[12] Y. Zhang, P. Markham, T. Xia, L. Chen, Y. Ye, Z. Wu, Z. Yuan, L. Wang, J. Bank, J. Burgett, R. W. Conners, and Y. Liu, "Wide-area frequency monitoring network (fnet) architecture and applications," *IEEE Transactions on Smart Grid*, vol. 1, pp. 159–167, Sep. 2010. 8

[13] G. Kou, S. W. Hadley, and Y. Liu, "Oak ridge national laboratory (ornl)," 2014. 8

[14] S. You, J. Guo, G. Kou, Y. Liu, and Y. Liu, "Oscillation mode identification based on wide-area ambient measurements using multivariate empirical mode decomposition," *Electric power systems research*, vol. 134, pp. 158–166, 2016. 8

[15] R. M. Gardner, J. N. Bank, J. K. Wang, A. J. Arana, and Y. Liu, "Non-parametric power system event location using wide-area measurements," in *2006 IEEE PES Power Systems Conference and Exposition*, pp. 1668–1675, Oct 2006. 8

[16] R. Gardner, J. Wang, and Y. Liu, "Power system event location analysis using wide-area measurements," in *2006 IEEE Power Engineering Society General Meeting*, 2006 IEEE Power Engineering Society General Meeting, pp. 7 pp.–7, IEEE, 2006. 8

[17] T. Xia, *Frequency Monitoring Network (FNET) Algorithm Improvements and Application Development*. PhD thesis, Virgina Tech., 2010. 8, 9, 16

[18] Z. Yuan, "Inter-area oscillation analysis using wide area voltage angle measurements from fnet," *Proc. 2008 IEEE Power Eng. Soc. Gen. Meet.*, pp. 1–7. 8

[19] Y. Zhang, *Frequency Monitoring Network (FNET) Data Center Development and Data Analysis*. PhD thesis, University of Tennessee, 2014. 9

[20] L. Wu, *Power System Frequency Measurement Based Data Analytics and Situational Awareness*. PhD thesis, University of Tennessee, 2018. 9, 12, 14, 17

[21] V. V. Terzija, "Adaptive underfrequency load shedding based on the magnitude of the disturbance estimation," *IEEE Transactions on Power Systems*, vol. 21, pp. 1260–1266, Aug 2006. 9, 19

[22] R. Azizipanah-Abarghooee, M. Malekpour, M. Paolone, and V. Terzija, "A new approach to the online estimation of the loss of generation size in power systems," *IEEE Transactions on Power Systems*, vol. 34, pp. 2103–2113, May 2019. 9

[23] P. M. Ashton, C. S. Saunders, G. A. Taylor, A. M. Carter, and M. E. Bradley, "Inertia estimation of the gb power system using synchrophasor measurements," *IEEE Transactions on Power Systems*, vol. 30, pp. 701–709, March 2015. 10

[24] P. M. Ashton, C. S. Saunders, G. A. Taylor, A. M. Carter, and M. E. Bradley, "Inertia estimation of the gb power system using synchrophasor measurements," *IEEE Transactions on Power Systems*, vol. 30, pp. 701–709, March 2015. 11, 19

[25] NERC, "Frequency Response Standard Background Document," tech. rep., NERC, November 2012. 15

[26] N. Shams, P. Wall, and V. Terzija, "Active power imbalance detection, size and location estimation using limited pmu measurements," *IEEE Transactions on Power Systems*, vol. 34, pp. 1362–1372, March 2019. 21

[27] NERC, "1,200 MW Fault Induced Solar Photovoltaic Resource Interruption Disturbance Report," tech. rep., NERC, June 2017. 23

[28] NERC, "900 MW Fault Induced Solar Photovoltaic Resource Interruption Disturbance Report," tech. rep., NERC, June 2017.

[29] W. R. E. M. T. Force, "WECC PV Power Plant Dynamic Modeling Guide," tech. rep., NERC, April 2014. 23, 26, 27

[30] Inverter-Based Resource Performance Task Force, "Prc-024-2 gaps whitepaper," tech. rep., NERC, 2018. 24

[31] Inverter-Based Resource Performance Task Force, "Inverter-based resource disturbance analysis," tech. rep., NERC, 2018. 24

[32] NERC, "Modeling Notification Recommended Practices for Modeling Momentary Cessation Initial Distribution," tech. rep., NERC, February 2018. 25

[33] N. R. guidline, "Power Plant Model Verification for Inverter-Based Resources," tech. rep., NERC, June 2018. 25

[34] I.-B. R. P. T. F. (IRPTF), "Resource Loss Protection Criteria Assessment," tech. rep., NERC, February 2018. 25

[35] WECC, "April and May 2018 inverter events," tech. rep., WECC, August 2018. 25

[36] J. H. Eto, J. Undrill, C. Roberts, P. Mackin, and J. Ellis, "Frequency control requirements for reliable interconnection frequency response," tech. rep., Energy Analysis and Environmental Impacts Division,Lawrence Berkeley National Laboratory, February 2018. 40, 86, 88

[37] E. Ela, M. Milligan, and B. Kirby, "Operating reserves and variable generation," tech. rep., NREL, August 2011. 40

[38] "Docket rm13-11, frequency response and frequency bias setting reliability standard," tech. rep., July 2018. 40

[39] N. A. E. R. Corporation, "Nerc bal-003-1 frequency response and frequency bias setting reliability standard," tech. rep., 2014. 40

[40] NERC, "Proposed Resource Loss Protection Criteria," tech. rep., NERC, 2019. 40

[41] CALISO, "frequency response study," tech. rep., February 2016. 41

[42] A. Arif, Z. Wang, J. Wang, B. Mather, H. Bashualdo, and D. Zhao, "Load modeling—a review," *IEEE Transactions on Smart Grid*, vol. 9, pp. 5986–5999, Nov 2018. 43

[43] NERC, "Reliability guideline, developing load model composition data," tech. rep., March 2017. 44

[44] C. Roselund, "California blows through solar power, renewable energy output records," *PV magazine*, May 2018. 44

[45] P. Kundur, J. Paserba, V. Ajjarapu, G. Andersson, A. Bose, C. Canizares, N. Hatziargyriou, D. Hill, A. Stankovic, C. Taylor, T. Van Cutsem, and V. Vittal, "Definition and classification of power system stability ieee/cigre joint task force on stability terms and definitions," *IEEE Transactions on Power Systems*, vol. 19, pp. 1387–1401, Aug 2004. 56

[46] T. Machida, "Improving transient stability of ac system by joint usage of dc system," *IEEE Transactions on Power Apparatus and Systems*, vol. PAS-85, pp. 226–232, March 1966. 56

[47] J. Arrillaga and I. M. Elamin, "Transient stability performance of a 3-machine system including an h.v. d.c. link," *Proceedings of the Institution of Electrical Engineers*, vol. 123, pp. 1239–1244, November 1976. 56

[48] C. W. Taylor, F. R. Nassief, and R. L. Cresap, "Northwest power pool transient stability and load shedding controls for generation-load imbalances," *IEEE Transactions on Power Apparatus and Systems*, vol. PAS-100, pp. 3486–3495, July 1981. 57

[49] R. Eriksson, V. Knazkins, and L. Soder, "On the assessment of the impact of a conventional hvdc on a test power system," in *2007 iREP Symposium - Bulk Power System Dynamics and Control - VII. Revitalizing Operational Reliability*, pp. 1–5, Aug 2007. 57

[50] Z. Huang, Y. Zeng, L. Guan, and J. Cao, "Study on a new power modulation strategy of hvdc to improve transient stability in china southern power grid," in *2013 1st International Future Energy Electronics Conference (IFEEC)*, pp. 844–848, Nov 2013. 57

[51] X. Zhou, H. Sun, B. Zhao, J. Wen, and A. Waqar, "Applying high-voltage direct current emergency control to suppress the peak value of ultra-high-voltage tie-line power oscillation," *IET Generation, Transmission Distribution*, vol. 9, no. 16, pp. 2485–2492, 2015. 57

[52] B. Pierre, R. Elliott, D. Schoenwald, J. Neely, R. Byrne, D. Trudnowski, and J. Colwell, "Supervisory system for a wide area damping controller using pdci modulation and real-time pmu feedback," in *2016 IEEE Power and Energy Society General Meeting (PESGM)*, pp. 1–5, July 2016. 57, 59

[53] C. Lu, X. Wu, J. Wu, P. Li, Y. Han, and L. Li, "Implementations and experiences of wide-area hvdc damping control in china southern power grid," in *2012 IEEE Power and Energy Society General Meeting*, pp. 1–7, July 2012. 57, 59

[54] R. King, O. Bagleybter, D. Wilson, and J. Yu, "Hvdc stability control using wide area measurements for optimising transmission boundary transfer," in *11th IET International Conference on AC and DC Power Transmission*, pp. 1–5, Feb 2015. 57

[55] K. W. V. To, A. K. David, and A. E. Hammad, "A robust co-ordinated control scheme for hvdc transmission with parallel ac systems," *IEEE Transactions on Power Delivery*, vol. 9, pp. 1710–1716, July 1994. 57

[56] G. A. Huang and V. Krishnaswamy, "Hvdc controls for power system stability," in *IEEE Power Engineering Society Summer Meeting,*, vol. 1, pp. 597–602 vol.1, July 2002. 57

[57] Yu Tao, Shen Shande, Zhu Shouzhen, Zhao Yuzhu, and Zhu Weijiang, "A novel auxiliary frequency controller for hvdc transmission links," in *Proceedings. International Conference on Power System Technology*, vol. 1, pp. 515–519 vol.1, Oct 2002.

[58] P. Ye, "Transient stability analysis of hu-liao hvdc and ac parallel transmission system," *Smart Grid and Renewable Energy*, vol. 01, pp. 74–80, 01 2010. 57

[59] J. Pan, "Hvdc control for improving grid transient stability," *IP*, 2018. 58

[60] C. Eriksson, "Critical intertie," *Power Engineering International*. 62

[61] T. U. Group, "COI Utilization Report," tech. rep., WECC, May 2011. 63

[62] WECC, "Western Interconnection Congestion Management study," tech. rep., WECC, 2006. 63

[63] S. Hoff, "U.s. electric system is made up of interconnections and balancing authorities," 2016. 71

[64] M. A. Elizondo, N. Mohan, J. O'Brien, Q. Huang, D. Orser, W. Hess, H. Brown, W. Zhu, D. Chandrashekhara, Y. V. Makarov, D. Osborn, J. Feltes, H. Kirkham, D. Duebner, and Z. Huang, "Hvdc macrogrid modeling for power-flow and transient stability studies in north american continental-level interconnections," *CSEE Journal of Power and Energy Systems*, vol. 3, pp. 390–398, Dec 2017. 72, 87

[65] K. Shetye, *Validation of power system transient stability results*. PhD thesis, University of Illinois at Urbana-Champaign, 2011. 73

[66] K. S. Shetye, T. J. Overbye, S. Mohapatra, R. Xu, J. F. Gronquist, and T. L. Doern, "Systematic determination of discrepancies across transient stability software packages," *IEEE Transactions on Power Systems*, vol. 31, pp. 432–441, Jan 2016.

[67] K. S. Shetye, T. J. Overbye, and T. L. Doern, "Assessment of discrepancies in load models across transient stability software packages," in *2015 IEEE Power Energy Society General Meeting*, pp. 1–5, July 2015. 73

[68] WECC, "WECC approved dynamic model library," tech. rep., WECC, 2018. 76

[69] NERC, "2018 Frequency Response Analysis," tech. rep., NERC, November 2012. 87

[70] C. W. 14.05, "Voltage source converter (vsc) hvdc for power transmission – economic aspects and comparison with other ac and dc technologies," tech. rep., CIGRE, 2002. 87

[71] C. J. C4/B4/C1, "Influence of embedded hvdc transmission on system security and ac network performance," tech. rep., CIGRE, 2013. 87

[72] S. I. Nanou and S. A. Papathanassiou, "Frequency control of island vsc-hvdc links operating in parallel with ac interconnectors and onsite generation," *IEEE Transactions on Power Delivery*, vol. 33, pp. 447–454, Feb 2018.

[73] O. D. Adeuyi, M. Cheah-Mane, J. Liang, and N. Jenkins, "Fast frequency response from offshore multiterminal vsc–hvdc schemes," *IEEE Transactions on Power Delivery*, vol. 32, pp. 2442–2452, Dec 2017.

[74] Z. Wenqiang, W. Yongping, C. Baoli, L. Haiying, and L. Zhiguo, "Study on frequency control strategy for ormoc-naga hvdc project in philippines," in *2016 IEEE PES Transmission Distribution Conference and Exposition-Latin America (PES T D-LA)*, pp. 1–6, Sep. 2016. 87

[75] Z. Yuan, S. You, Y. Liu, Y. Liu, D. Osborn, and J. Pan, "Frequency control capability of vsc-hvdc for large power systems," in *2017 IEEE Power Energy Society General Meeting*, pp. 1–5, July 2017. 87

[76] NERC, "Frequency response initiative report," tech. rep. 88

[77] Y. Rink, L. Held, S. Wenig, M. Suriyah, and T. Leibfried, "On implementation of primary frequency control in mmc-hvdc transmission systems," in *2017 IEEE PES Innovative Smart Grid Technologies Conference Europe (ISGT-Europe)*, pp. 1–6, Sep. 2017. 88

[78] L. Harnefors, N. Johansson, and L. Zhang, "Impact on interarea modes of fast hvdc primary frequency control," *IEEE Transactions on Power Systems*, vol. 32, pp. 1350–1358, March 2017.

[79] M. Andreasson, R. Wiget, D. V. Dimarogonas, K. H. Johansson, and G. Andersson, "Distributed primary frequency control through multi-terminal hvdc transmission systems," in *2015 American Control Conference (ACC)*, pp. 5029–5034, July 2015.

[80] A. Laukhamar, L. Zeni, and P. Sørensen, "Alternatives for primary frequency control contribution from wind power plants connected to vsc-hvdc intertie," in *European Wind Energy Conference amp Exhibition*, October 2014. 88

[81] M. Davies, A. Kolz, M. Kuhn, D. Monkhouse, and J. Strauss, "Latest control and protection innovations applied to the basslink hvdc interconnector," in *The 8th IEE International Conference on AC and DC Power Transmission*, pp. 30–35, March 2006. 88

[82] F. Mazzoldi, J. P. Taisne, C. J. B. Martin, and B. A. Rowe, "Adaptation of the control equipment to permit 3-terminal operation of the hvdc link between sardinia, corsica and mainland italy," *IEEE Transactions on Power Delivery*, vol. 4, pp. 1269–1274, April 1989.

[83] J. Chand, "Auxiliary power controls on the nelson river hvdc scheme," *IEEE Transactions on Power Systems*, vol. 7, pp. 398–402, Feb 1992. 88

[84] J. Undrill, "Primary frequency response and control of power system frequency," tech. rep., Lawrence Berkeley National Laboratory, 2018. 88

[85] M. Scherer and P. Zolotarev, "Frequency-response coupling between synchronous areas in europe," in *2015 IEEE Eindhoven PowerTech*, pp. 1–6, June 2015. 88

[86] P. McNamara and F. Milano, "Model predictive control-based agc for multi-terminal hvdc-connected ac grids," *IEEE Transactions on Power Systems*, vol. 33, pp. 1036–1048, Jan 2018.

[87] E. Rakhshani, D. Remon, A. M. Cantarellas, J. M. Garcia, and P. Rodriguez, "Virtual synchronous power strategy for multiple hvdc interconnections of multi-area agc power systems," *IEEE Transactions on Power Systems*, vol. 32, pp. 1665–1677, May 2017.

[88] E. Rakhshani, H. Mehrjerdi, N. A. Al-Emadi, and K. Rouzbehi, "On sizing the required energy of hvdc based inertia emulation for frequency control," in *2017 IEEE Power Energy Society General Meeting*, pp. 1–5, July 2017. 88

[89] Y. Lu, Y. Lei, G. Kou, K. Tomsovic, and Y. Liu, "Reduced wecc and ei models for education and research," Nov 2016. 93

[90] P. Björklund, K. Srivastava, and W. Quaintance, "Hvdc light® modeling for dynamic performance analysis," in *2006 IEEE PES Power Systems Conference and Exposition*, pp. 871–876, Oct 2006. 93

[91] J. G. Kappenman, S. R. Norr, G. A. Sweezy, D. L. Carlson, V. D. Albertson, J. E. Harder, and B. L. Damsky, "Gic mitigation: a neutral blocking/bypass device to prevent the flow of gic in power systems," *IEEE Transactions on Power Delivery*, vol. 6, pp. 1271–1281, July 1991. 125

[92] M. A. Eitzmann, R. A. Walling, M. Sublich, A. H. Khan, H. Huynh, M. Granger, and A. Dutil, "Alternatives for blocking direct current in ac system neutrals at the radisson/lg2 complex," *IEEE Transactions on Power Delivery*, vol. 7, pp. 1328–1337, July 1992.

[93] L. Bolduc, M. Granger, G. Pare, J. Saintonge, and L. Brophy, "Development of a dc current-blocking device for transformer neutrals," *IEEE Transactions on Power Delivery*, vol. 20, pp. 163–168, Jan 2005.

[94] A. D. Rajapakse, N. Perera, F. R. Faxvog, W. Jensen, G. Nordling, G. Fuchs, D. B. Jackson, T. L. Volkmann, N. Ruehl, and B. Groh, "Power grid stability protection against gic using a capacitive grounding circuit," in *PES T D 2012*, pp. 1–6, May 2012. 125, 127, 128

[95] F. R. Faxvog, W. Jensen, G. Fuchs, G. Nordling, D. B. Jackson, B. Groh, N. Ruehl, A. P. Vitols, T. L. Volkmann, M. R. Rooney, and R. Neal, "Power grid protection against geomagnetic disturbances (gmd)," in *2013 IEEE Electrical Power Energy Conference*, pp. 1–13, Aug 2013. 125, 127

[96] P.Barnes and et.al, "Electric Utility Industry Experience with Geomagnetic Disturbances," tech. rep., Oak Ridge National Laboratory, 1991. 125

[97] J.G.Kappenman, "Low Frequency Protection Concepts for the Electric Power Grid: Geomagnetic Induced Current (GIC) and E3 HEMP Mitigation," tech. rep., Oak Ridge National Laboratory, 2010.

[98] E. Arajarvi, R. Pirjola, and A. Viljanen, "Effects of neutral point reactors and series capacitors on geomagnetically induced currents in a high-voltage electric power transmission system," *Space Weather*, vol. 9, pp. 1–10, Nov 2011.

[99] K. R. Padiyar, *Analysis of subsynchronous resonance in power system.* Power Electronics and Power systems, Springer US, 1999. 125, 126, 135

[100] EPRI, "Torsional Interaction Between Electrical Network Phenomena and Turbine-Generator Shafts," tech. rep., EPRI, 2006. 125, 126

[101] "Reader's guide to subsynchronous resonance," *IEEE Transactions on Power Systems*, vol. 7, pp. 150–157, Feb 1992. 126

[102] J. W. Ballance and S. Goldberg, "Subsynchronous resonance in series compensated transmission lines," *IEEE Transactions on Power Apparatus and Systems*, vol. PAS-92, pp. 1649–1658, Sep. 1973. 126

[103] "Terms, definitions and symbols for subsynchronous oscillations," *IEEE Transactions on Power Apparatus and Systems*, vol. PAS-104, pp. 1326–1334, June 1985. 126

[104] "First benchmark model for computer simulation of subsynchronous resonance," *IEEE Transactions on Power Apparatus and Systems*, vol. 96, pp. 1565–1572, Sep. 1977. 129

[105] "Second benchmark model for computer simulation of subsynchronous resonance," *IEEE Transactions on Power Apparatus and Systems*, vol. PAS-104, pp. 1057–1066, May 1985. 129

[106] M. Inc, "Varistor documentation," tech. rep., MATLAB Inc., 2018. 134

# Appendices

# A Effect of GIC Blocking Devices on Subsynchrnous Oscillations in Generators

## A.1 Introduction

Neutral blocking device (NBD) is considered as one of the most effective approaches for mitigating the effects of Geomagnetic Induced currents( GIC) [91–95]. They are inserted on the neutral of those transformers that are considered at-risk from GICs impact perspective. Typically, in an NBD, a capacitor and a resistor are connected in series to the neutral of the transformer in case of grounded Y, or in series with the phase wires for auto-transformers [91].

NBDs block (strongly attenuate) the very low-frequency components of the GICs from entering the transformer: this prevents the transformer from saturating near the peak of the half-cycle of the power waveform. As it is well known, driving a transformer to saturation leads to generation of an anomalous level of harmonic flow, possibly impacting nearby reactive compensation units (that could go off-line, due to protection tripping). In the most severe cases, this may also have a cascading effect and lead to large-scale voltage instability [96]. Furthermore, prolonged operation in partially saturated conditions may cause thermal damages to the transformer itself.

NBDs have been successfully tested in the field. However, they have not been adopted by the industry as the solution on a large scale. There are some concerns about possible operational issues resulting from NBDs installation, namely a reduced functionality of distant protection relays, impact on the GIC intensity in lines where NBDs have not been inserted, and the establishment of resonant conditions in buses connected to synchronous generators [94]. Some of these issues have been already addressed in the literature [96–99]. In [100], several scenarios were tested on a benchmark model with NBDs during normal and abnormal operations, including short-circuit current, and ferroresonance conditions.

However, the possibility of NBD causing the Sub-Synchronous Resonance (SSR) oscillations has not been studied in detail. The phenomenon that involves the exchange of energy between the mechanical system of the generator (turbine) and the electrical system at a natural frequency below the synchronous frequency of the system (60Hz) is known as Subsynchronous resonance (SSR) [99, 101]. Depending on the nature of the SSR, the magnitude of oscillations, and the severity of its impact can vary significantly [101]. SSRs cause torsional stress in rotating machines, and that can lead to shaft failures [102]. Torsional stress issues related to SSRs in a network with multiple generators have been studied in [100]: in this case, the presence of series capacitor compensation in transmission lines has been found to be one of the main causes for the establishment of SSR conditions.

This provides a justification for the present study: enabling the NBD protection consists essentially to insert capacitor in series on the neutral of a Y-configured transformer winding. Thus, in conditions where the current on the neutral becomes significant (i.e., for large phase unbalance, typically from fault conditions), there is the possibility of triggering a resonant electromechanical oscillation with a synchronous generator in close proximity. This phenomenon is called as torque amplification. In this work, the possibility of torque amplification is studied.

## A.2 Theory of Sub-synchronous Oscillations

Depending on the nature of the interactions, the SSR has been classified into three categories[101, 103]:

1. Induction generator effect: This phenomenon is observed only in the electrical subsystem, and there is a generator in the proximity of a capacitor. When there is an external resonant circuit with a natural frequency of fer, there are armature currents that that are introduced at $f_0 + f_{er}$ and $f_0 - f_{er}$ frequencies. The subsynchronous frequency of $f_0 - f_{er}$ causes a rotating magnetic field that is slower than the rotor magnetic field. Hence, the rotor resistance as viewed from armature terminals is negative, and if this is lesser than the armature and the network resistances, the electrical system is self-excited and might result in an increase in voltages and currents. This phenomenon is considered as a small signal stability issue and is analyzed using linear techniques.

2. Torsional interaction: This phenomenon is observed when one of the resonant frequencies of the external electrical circuit is close to the torsional modes of the rotor. When a small disturbance excites natural modes of the external circuit or the turbine, and they interact with each other in such a way that the resultant armature currents cause the torques to amplify which in turn cause the voltages to increase and lead to sustained oscillations. These oscillations are referred to as torque interaction, and can also be analyzed using linear techniques.

3. Torsional Amplification: When a large disturbance occurs in the power system, and the resonant frequency is closer to the shaft frequency, then the resulting torque in the turbine is much greater than the ones produced during three phase faults and lead to unnecessary mechanical stress. If the timing of the fault reinforces the torque amplification, it can result in even higher torques and hence needs to be studied in detail. Unlike the other two phenomena, this is a nonlinear phenomenon because torque amplification is observed after a severe fault(including an unbalanced fault) occurs. As this is not a small disturbance(in some cases balanced), the assumptions of linearity are not valid. The behavior of all the power system components, including the turbine and generator, is nonlinear. Therefore, to model this phenomenon accurately EMTP type time domain simulation software is needed. In this work, the possibility of torque amplification during large disturbances due to the resonance between the turbine and the NBD is studied in detail.

## A.3 NBD Description

The schematic illustration of a neutral blocking device is shown in Fig. A.1 (reproduced from [94]). There are three modes of operations, depending on the condition of the grid:

1. Normal mode: The neutral is grounded through the switch. This mode is the default configuration in normal operations when no GICs have been detected.

2. Blocking mode: Once GIC is detected, the blocking mode is switched on by inserting a capacitor in series with a resistor on the neutral [95]. The resistor used is close to 1

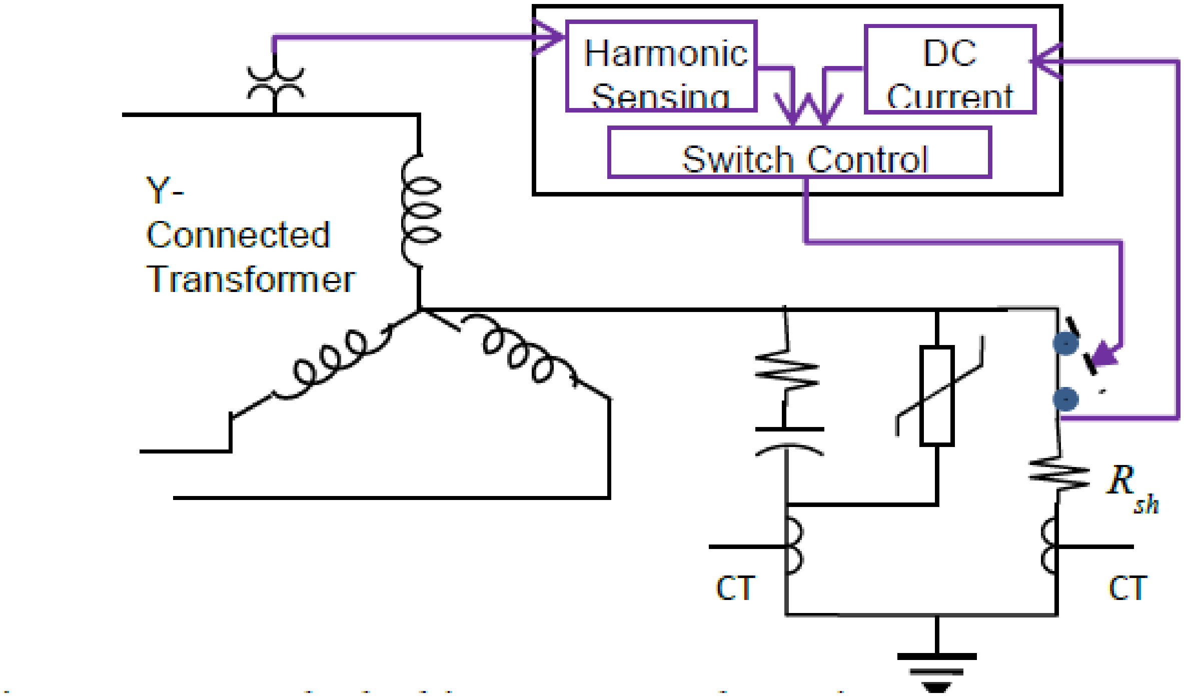


**Figure A.1:** High-level scheme of a GMD Blocking device

Ω and is used to damp the oscillations in the neutral during transients. The capacitor prevents the low-frequency, common-mode GIC flowing into the lines connected to the transformer, while leaves any neutral current at power frequency unaffected.

3. Fault mode: This mode is activated when the device is already in the blocking mode (i.e., GIC currents have been detected) and a ground fault occurs, leading to a large current in the neutral. A metal-oxide varistor (MOV) is used to protect the capacitor from an over voltage condition. A MOV is a nonlinear component whose resistance is drastically reduced when the voltage across it increases. Thus, during a fault, when its applied voltage rises above a specified threshold. In this way, if the voltage builds up on the NBD capacitor becomes larger than the MOV threshold, the MOV provides a bypass for the current in the capacitor, thus protecting it from overvoltage damages. In the model here considered the MOV during the conduction mode is simulated by a small resistor. It typically takes around 1-5 ms for the voltage across the capacitor to trigger the MOV [94]conduction.

## A.4 Model Description and Methodology

The power system model is based on the first IEEE benchmark model [104, 105] and the corresponding MATLAB Simulink model is shown in Fig. A.2. It consists of a single generator connected to an infinite bus through a transformer and a long transmission line. The detailed model of the turbines of the generator is used The three torsional modes of the turbines are 24.65 Hz, 32.39 Hz, and 51.10 Hz. The IEEE benchmark model was initially designed to study the effects of series compensation on torsional modes, and therefore a capacitor is present in series with the transmission line. Since the focus of this work is the energy exchange between the capacitor on the neutral and the generator turbine, the capacitor originally present in series with the transmission line has been removed.

As described in the previous section, an NBD consists of a resistor, a capacitor, and a MOV. The primary objective is to study if the occurrence of a fault could cause significant energy exchanges between the turbine and the capacitor in the NBD. Therefore, initially, the effect of only the capacitor and the resistor on the neutral of the transformer on the subsynchronous oscillations is studied. The model used for this initial study is shown in Fig. A.2. Then a detailed model of NBD including a MOV to conduct a more practical study.

The occurrence of a fault can be in first approximation represented as a rectangular pulse (first is when the fault is switched on, and then when the fault is cleared). The fault triggers

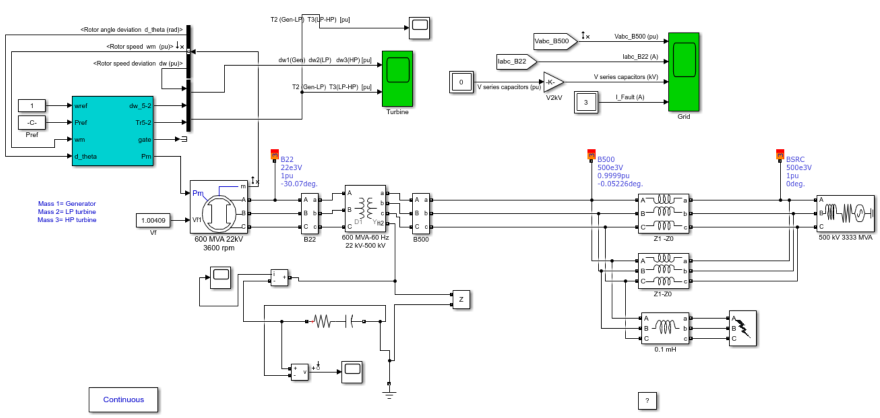


**Figure A.2:** Simulink model of the test system with a capacitor and resistor (without MOV) a step response of the system, where, all the natural frequencies of the system, including the torsional frequencies and the capacitor-resonance frequencies, are present. Since this is a large disturbance, (compared to the nominal parameters during normal operations) there could be significant energy exchange between the turbines and the electrical network, and, if resonant conditions exist, a torque amplification may occur. Following the occurrence of a large fault, the power system components behave nonlinearly, and to study them accurately, EMTP type time domain simulation is needed. Therefore, the Matlab-Simulink tool box is used.

## A.5 Simulation Results

### Effect of a Capacitor on the Neutral on the SSO

The impact of the capacitor in the neutral, in relation to the possible trigger of the Sub-synchronous oscillations, is analyzed by varying the magnitude and the duration fault and observing the effect on the maximum torque in the rotating machine. These results are mostly referring to a theoretical worst-case scenario, because GIC blocking devices are designed to prevent the capacitor from being inserted when the current is above a given level, e.g., for most fault conditions. In order to study the effect of a capacitor inserted on the neutral, asymmetric faults are required; in this case, a line-to-ground (LG) fault is considered. The case of a 50$\mu$F capacitor connected to the neutral of the transformers, when an LG fault is applied and cleared after four cycles are presented in detail in Fig. A.3. In this case, it can be seen that the maximum torque reaches almost 4 pu. The corresponding current through the capacitor in the neutral is also shown in Fig. A.4.

The variation of the magnitude of the maximum torque in the generator for different values of the capacitor in the neutral is shown in Fig. A.5, where it can be seen that the maximum torque occurs for a capacitor of about 50 $\mu$F. This value corresponds to a resonance frequency near 36 Hz, which corresponds to the $60 - f_r$ ($f_r$ corresponding to 24 Hz torsional mode). The maximum torque seen in this case is closer to 3.75 pu, which is an amplitude that might cause serious damage to the shaft of the generators. When the value of the

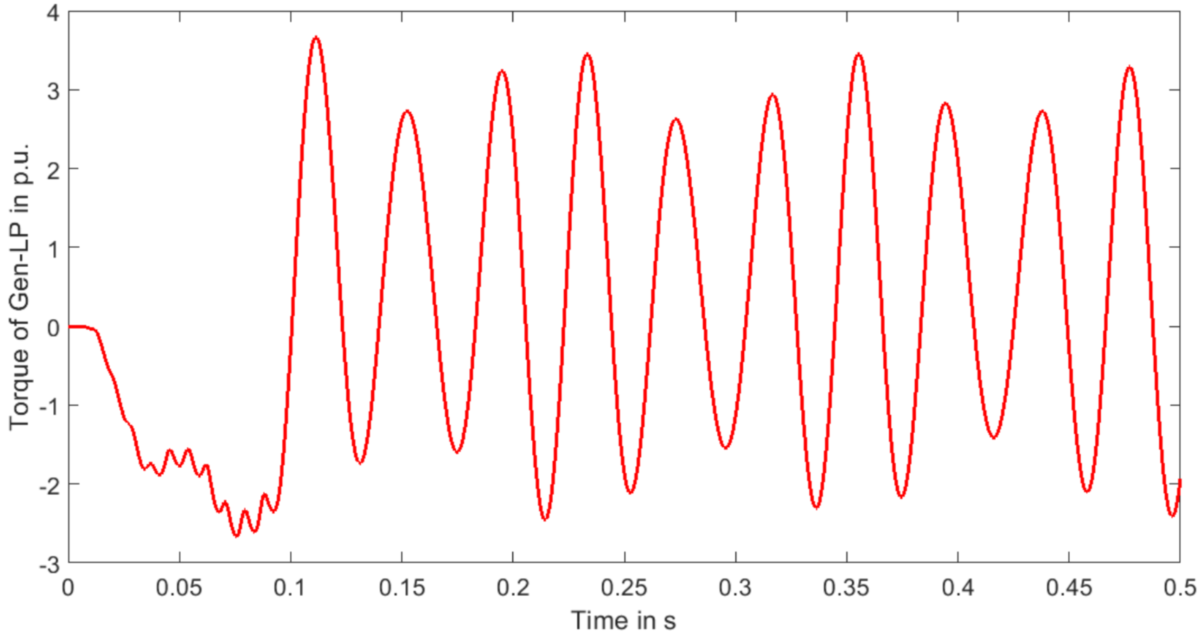


**Figure A.3:** Maximum torque variation observed in generators when sub-synchronous oscillations are triggered (50$\mu$F is connected to the neutral of a transformer)

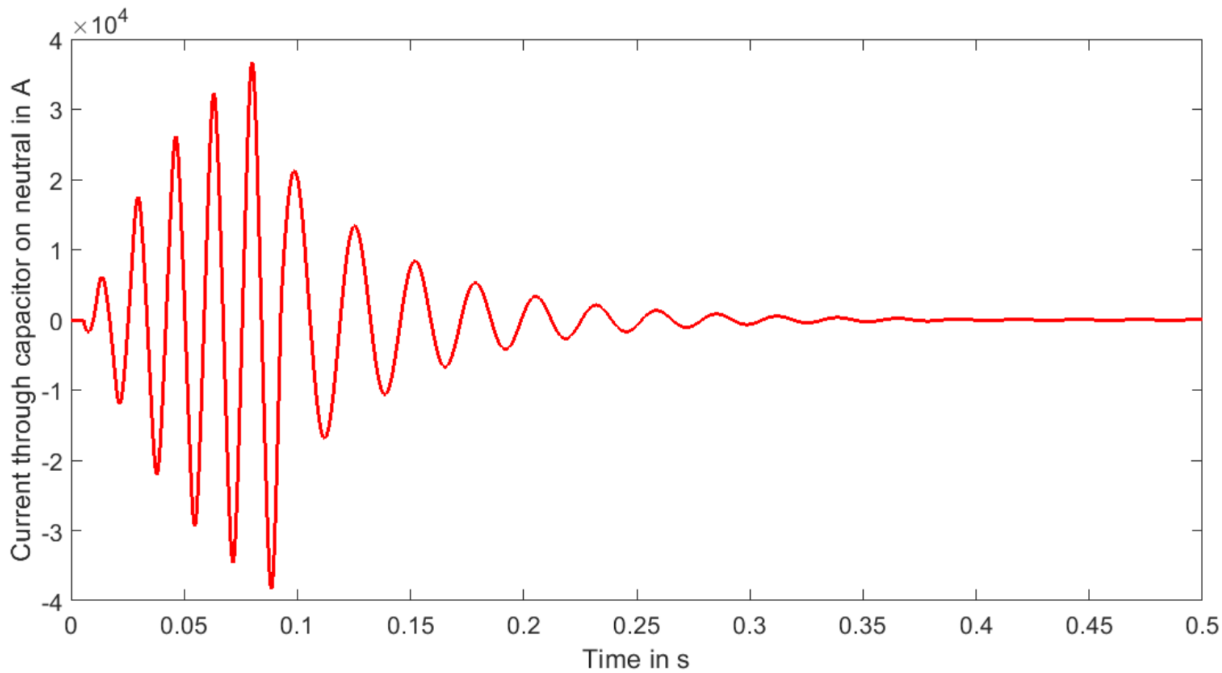


**Figure A.4:** The current through the capacitor on neutral when sub-synchronous oscillations are triggered (50$\mu$F is connected to the neutral of a transformer) capacitor is increased, it can be seen that the torque amplification is significantly reduced, in other words, using a larger capacitor prevents the onset of sub-synchronous resonances.

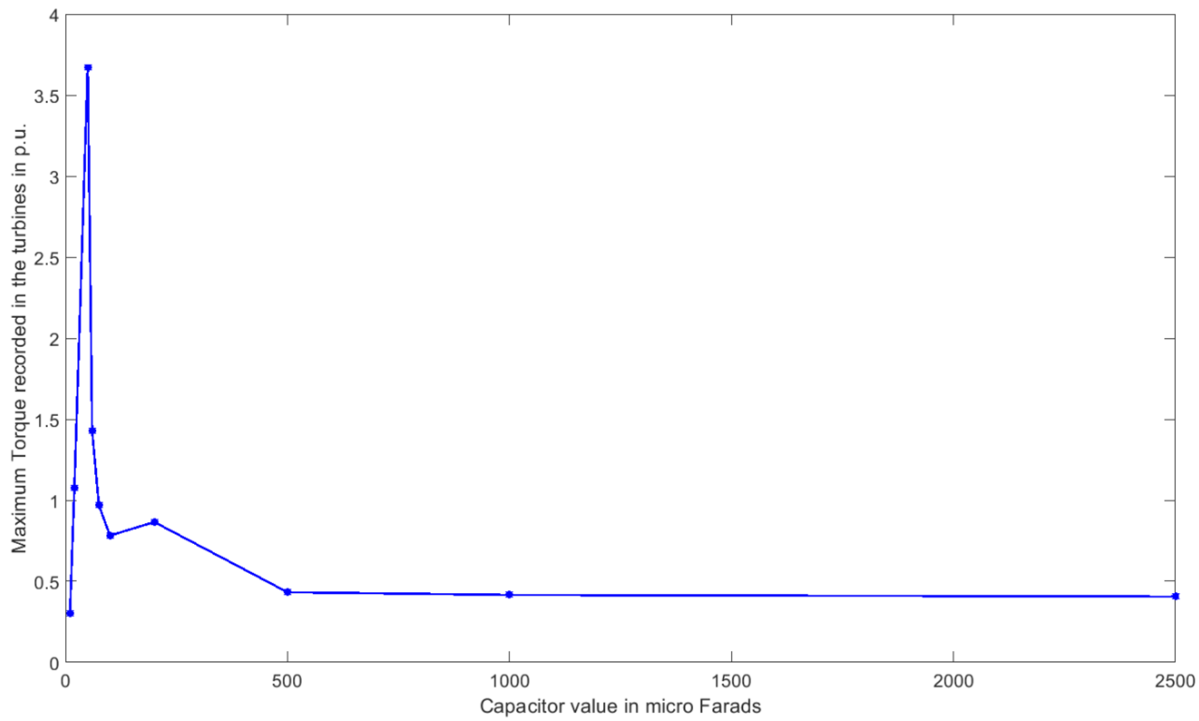


**Figure A.5:** Variation of torque with capacitor

Considering that the effect of a large fault is being studied, the variation of the fault clearing time has a significant influence on the behavior of the system. With a $50\mu$F capacitor, the change of magnitude of the maximum torque vs. fault clearing time is shown in Fig. A.6. Here it can be seen that maximum torques correspond to a fault clearing time in the order of 6 cycles and that when the clearing time is increased beyond that value, the maximum torque is reduced.

Another series of simulations were conducted to study the effects of different fault types on the torque amplification, as shown in Fig. A.7, where the torque vs. time is plotted for the five possible fault scenarios (as in the inset of Fig. A.7). This test shows that the large torque amplification resulting from the fault is present only for the LG case, that is the one that leads to the most unbalanced condition.

The impedance value of $50\mu$ F capacitor at 60Hz is around $50\Omega$. Practically, this high value of impedance is not added to the neutral of the transformer. The value of the impedance

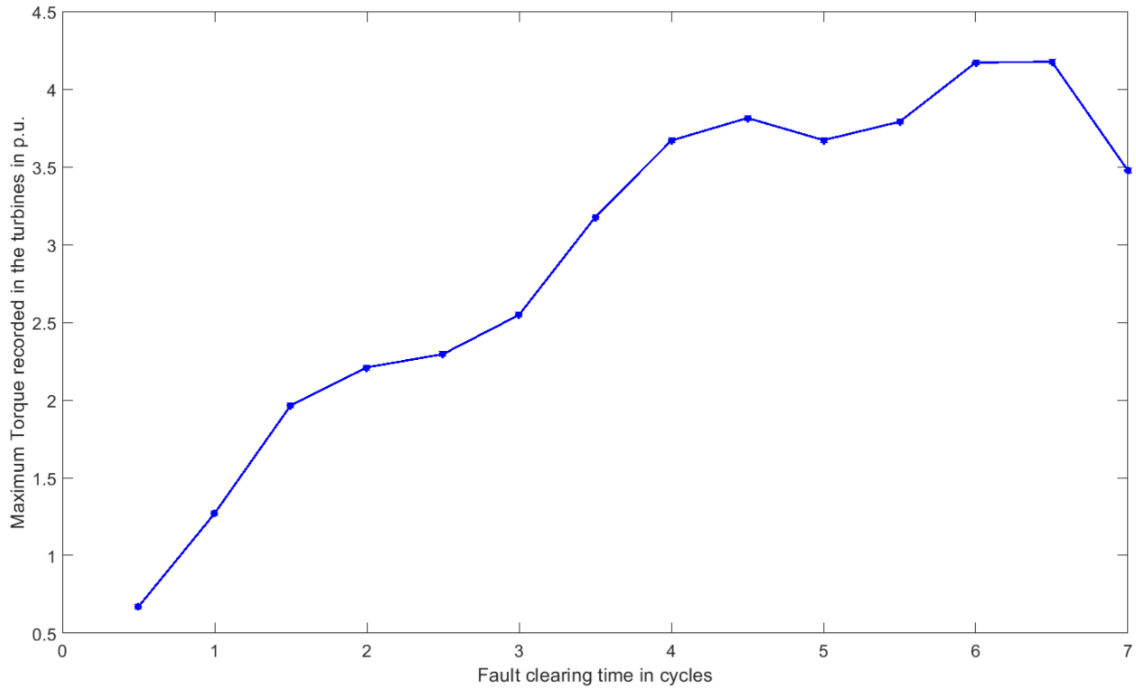


**Figure A.6:** Variation of torque with fault time

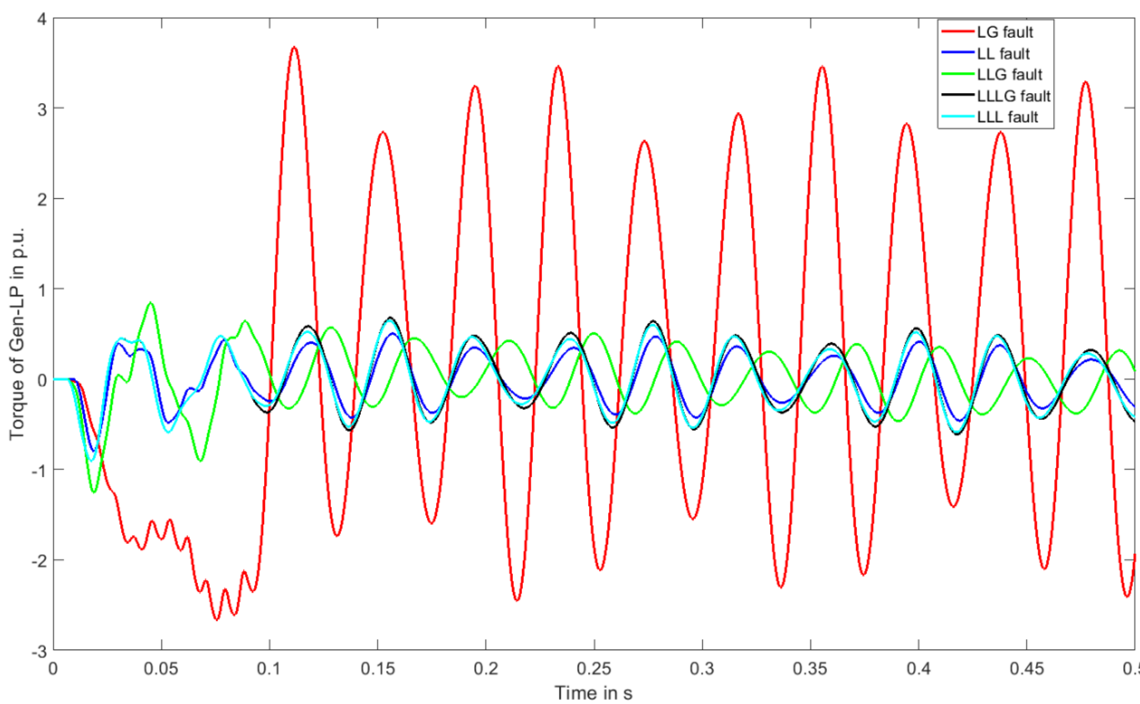


**Figure A.7:** Effect of different faults on the torque output of the generators

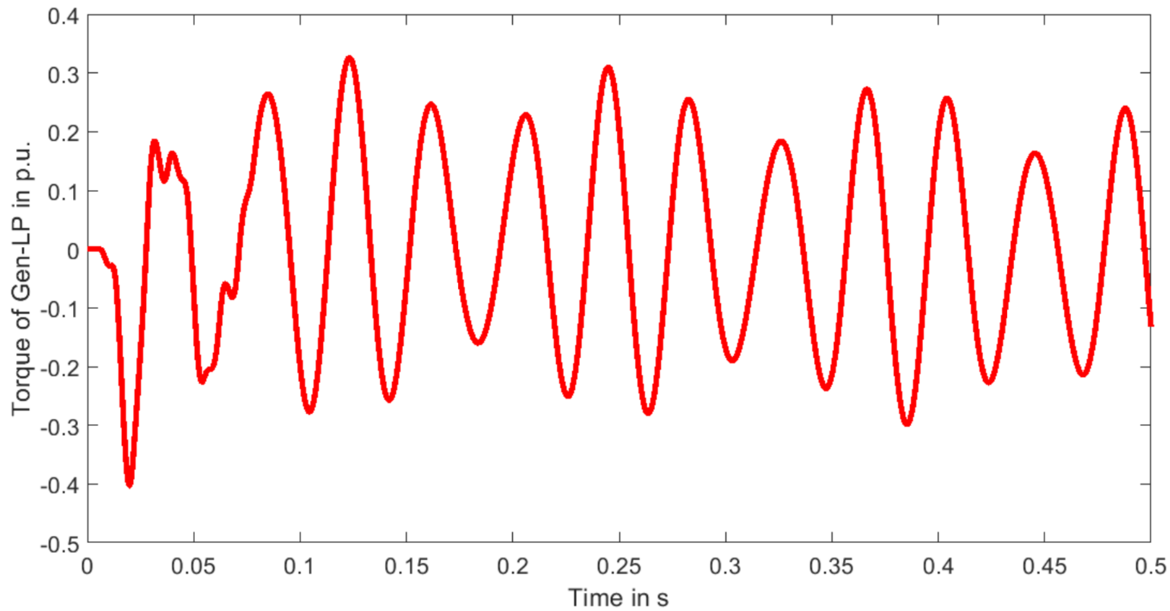


**Figure A.8:** Torque of the generators with capacitor value of (2500 $\mu$F)

usually included is closer to 1Ω which corresponds to 2500 $\mu$F. When a LG fault is initiated and cleared after 4 cycles, the torque seen in the generator turbine is shown in Fig. A.8. It can be seen that the maximum torque only reaches 0.8 pu which is much smaller compared to the values reached in previous simulations.

### Effect of NBD (including MOV) on the SSO

Even though it can be seen that including a capacitor in the neutral could cause torsional interactions, the NBD in reality is designed with a bypass circuit with a MOV to protect the capacitor on the neutral (as shown in Fig. A.9). Thus, during faults, the capacitors are bypassed when the voltage exceeds a given threshold. MOV is basically a voltage-dependent resistor that is commonly used to protect components from high voltage surges. When this device is placed in parallel with the capacitor, it exhibits low resistance when the voltage across the component goes beyond the clamp voltage. Once the MOV enters this pressure relief region, it will not return to the high resistance region. It must be replaced. The detailed model of the MOV is described in [106].

In this work, a varistor has been added in parallel with the capacitor in the neutral of the transformer. The clamp voltage of the MOV is set at 4kV (similar to the one used in

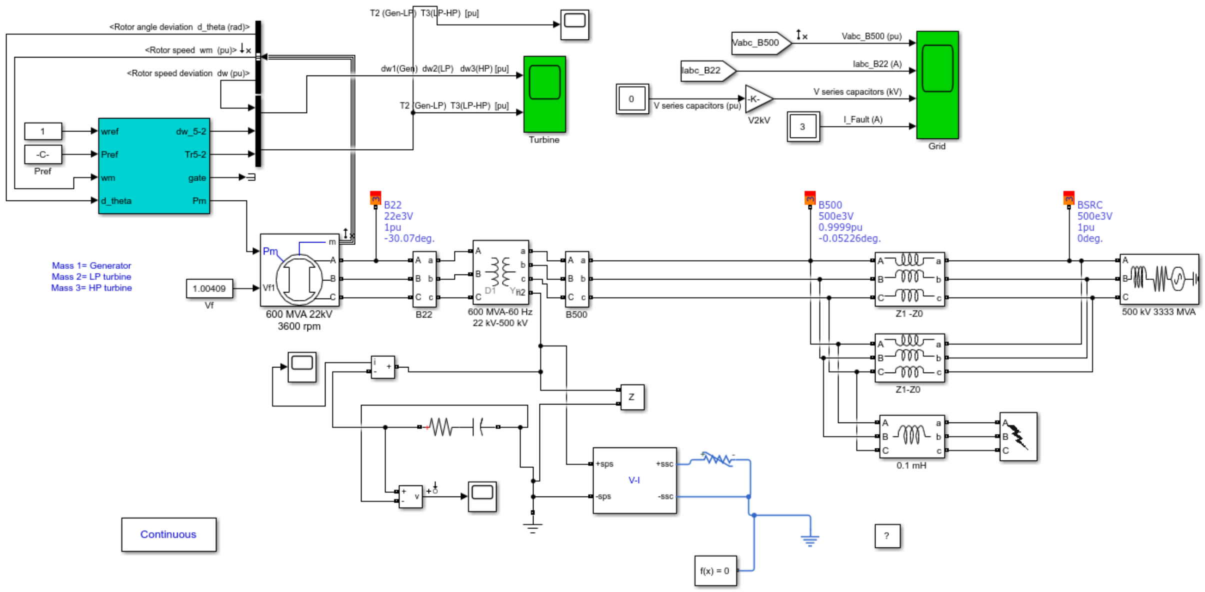


**Figure A.9:** Simulink model of the test system with NBD (with capacitor, resistor and MOV)

[99]) . Thus, additional simulations are conducted with an improved realistic model of the NBD. In this case, when the voltage across the capacitor reaches 4kV, a certain pre-defined threshold, the capacitor is bypassed by an MOV that enters in the conduction mode (this is done to prevent damage to the capacitor) and the energy exchange between the capacitor and the turbine is reduced. In practice, this switching occurs within 1-5 ms, depending on the fault impedance. MOV

It can be seen that when the voltage across the capacitor goes beyond the MOV break down voltage, the current in the capacitor is reduced drastically. The variation of torque with time is shown in Fig. A.10. It can be seen that if the MOV switch operates correctly, then there would be no interaction between the capacitor and the torsional modes of the generator, and torque amplification might be avoided. It can be seen that when the voltage across the capacitor goes beyond the MOV break down voltage, the current in the capacitor is reduced drastically.

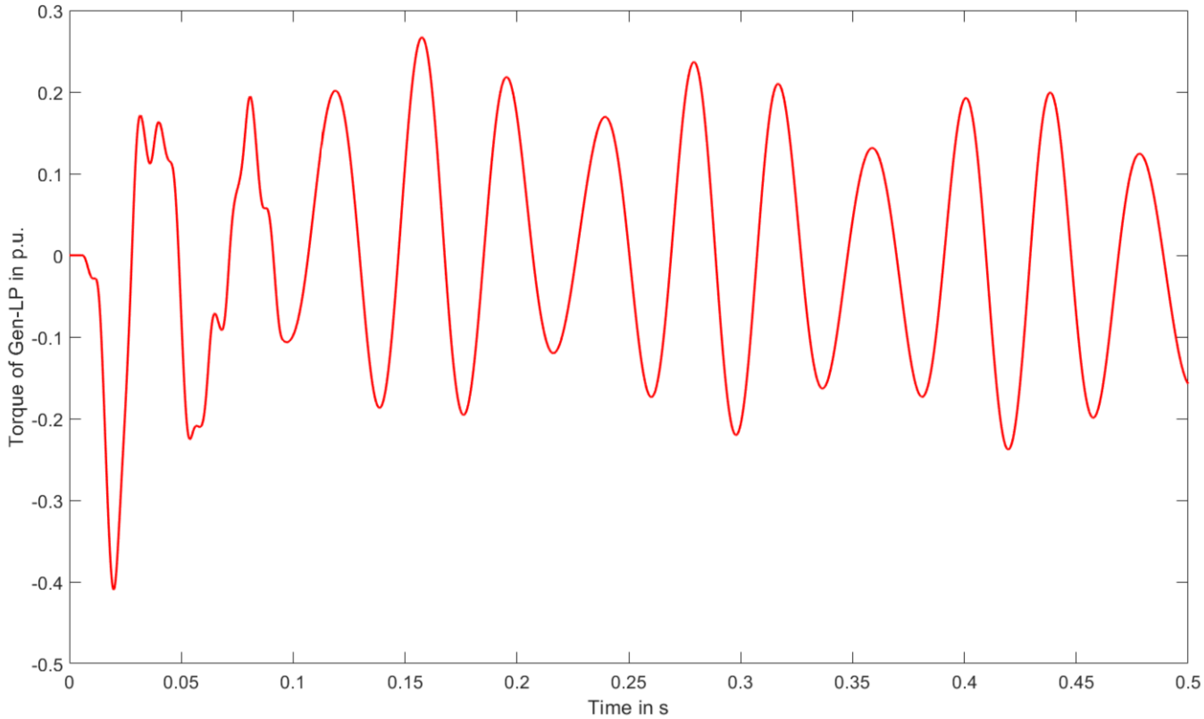


**Figure A.10:** Torque in generators when the fault is applied with NBD model

## A.6 Conclusion

In this chapter, the possibility of Neutral blocking device causing SSR in the generators has been investigated. Specifically, the possibility of torque amplification has been demonstrated. The torque amplification may be particularly severe when the value of the NBD capacitor is small, as compared to standard NBD designs. However, for typical capacitor values and with the MOV operating properly, there seem to be no concern about the triggering of the SSOs.

Since a particular bus system is analyzed in this study, for a more general conclusion, more bus configurations and torsional frequencies should be considered to ensure that even with higher values of capacitors the SSOs can be always avoided. Hence, in general, it would be recommended to conduct similar analysis to the one here presented, regarding the effect of NBD on the SSO before the installation.

# B Faster than Real-time Electrodynamic Simulation using FPGAs

## B.1 Introduction

The work described in this chapter has been done as a part of Grid Self-Aware Elastic Extensible Resiliency (Grid-SEER) project. The purpose of the project is to create an open, scalable, hybrid, real-time, grid simulator and an open software suite (models, solvers, and design/configuration tools) which runs on scalable, commercially available, high-performance hardware (multi-CPU/FPGA/GPU like the low-latency reconfigurable FPGA-supercomputer) integrating wide-area (electromechanical simulations) with multiple "smaller regions" of higher fidelity/time-scale (power-electronics/electromagnetic simulations). As the part of the feasibility study the electromechanical simulation of 9 bus system is developed and tested using LabVIEW software. A faster than real time electromechanical simulation is developed on the NI R series -7976R FPGA platform using LabVIEW FPGA software. An estimation of the resources required to simulate the Eastern Interconnect in real time is done.

The mathematical modeling and numerical techniques involved in simulation of a real power system like Eastern Interconnection are arduous. Massive number of computations need to be carried out in every time step. This is usually achieved in most of these tools by using multiple processors operating in parallel with a communication network to exchange data. Different processors like reduced instruction set computers, digital signal processors, graphical processing units have all been used to improve the performance of the simulations. In spite of extremely efficient parallel algorithms, large communication latency has made simulation of very large systems impractical.

Field Programmable Gate Arrays (FPGA) have gained popularity because large number of computations can be done in parallel. FPGAs have logic blocks and input output blocks that can be customized to the requirements of the simulation. New technologies like PCIe allow high speed communication between FPGAs thus allowing large amount of data exchange. The main reason FPGA based simulators have not gained traction is probably because VHDL programming of FPGA is complex. National Instruments has developed a Graphical User Interface based system design software called LabVIEW. It has been widely accepted in the research community and is used for various applications. It is flexible and also supports a lot of mathematical functions as well. The main advantage of this software is that it has a FPGA design toolbox. FPGAs can be programmed directly using LabVIEW without having to deal with cumbersome programming of FPGAs using VHDL. LabVIEW directly optimizes the design. LabVIEW FPGA is effective and shortens the time for developing the design.

## B.2 Architecture of the FPGA based Simulator

As it has been mentioned before, FPGAs are highly parallel and completely programmable computational platform. From a simulator development standpoint, this is extremely advantageous as one can parallelize the algorithm according to the specific system to ensure optimal use of resources and performance. On, the other hand, this also means that we need to develop not just the computational code but also various control blocks to basically handle the memory, data and communication of the entire system. In case of large system simulator with the multiple FPGAs, there would be a need to develop a central controller that orchestrates the entire thing. The proposed architecture has hierarchical control design, where apart from the central intelligence unit individual FPGAs too have controllers, that control the data flow in the controller and memory access to the block RAM. We provide a general abstraction about this FPGA system. The simulator consists of four major functional blocks as shown in Fig . B.1

1. Central Intelligence Unit (CIU): The primary function of the CIU is that of a main controller. Depending on the algorithm chosen to solve the system, the CIU will partition the set of equations to be solved among the FPGA computation units. The splitting of equations will be depend on the topology of the network and on the regions of electromechanical simulation and electromagnetic simulation. It will also keep track of the nonlinearities present in the system and significant changes in the topology to change the system of equations accordingly. This will be running on the

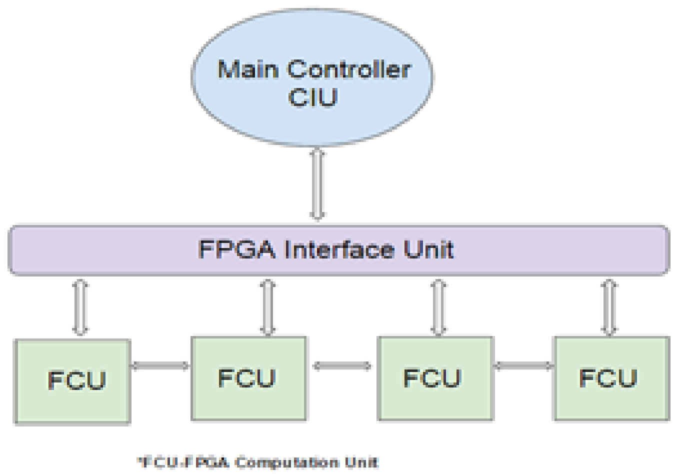


**Figure B.1:** Functional blocks of FPGA simulator

CPU where all the pre-simulation routines likes load flow, Y bus formation, machine parameter calculations will be done. As these routines are not time sensitive, they can be programmed on CPU itself.

2. FPGA Interface Unit: The primary function of this unit is to keep track of the communication between the different parts present in the system. It ensures that the timing constraint of the real time simulator is not violated. It synchronizes all the units at every time step. It is also acts like an intermediate between the CIU and the FPGA computation units.

3. FPGA Computation Units (FCU): These are the primary computation blocks. All the arithmetic operations will be done in these units. Depending on the type of computation (electromagnetic simulation or electrodynamic simulation or both), different topologies are implemented to maximize parallelism and increase the computation speed. Pipelining techniques would be used to ensure large amount of computation can be done simultaneously. Apart from these FPGA based computation units, there may be additional controllers included in the design. The modular designs allows for different sub-systems to be included.

4. Communication Channels: PXIe chassis facilitate large amount of data transfers at a very fast rate. In this system, Zero byte latency is between 1.2 and 2 $\mu$sec depending on

the FPGA card. The FPGA cards currently used utilize gen 2x8 interfaces capable of 3.2 GBytes/sec into or out of the module. The PXIe chassis is capable of 24 GBytes/sec overall bandwidth between all cards in the chassis. Considering communication has been the bottleneck with large scale simulation, this new communication technology will support this architecture. In case of electromagnetic simulation, components like PWM engine were also developed and incorporated into the system. In case of electrodynamic simulation integrator and transformation blocks were developed which are discussed in depth at a later stage. Basically, depending on the simulation conditions, additional blocks might be added to the design hence ensuring the modularity of the design.

The main computational unit of the real time simulator mainly consists of three blocks:

- Integration block.
- Transformation block
- Matrix multiplication block

1. Integration block: In its current form, the explicit integration technique of Forward Euler is used to solve the differential equations. $6^{th}$ order generator model is used to model the synchronous generators in all the cases. Therefore, six differential equations are to be solved for every generator in every single time step. The algorithm has been made flexible to handle more complicated models with additional controls.

2. Transformation block: In order to transform the variables from network reference frame to machine reference frame, trigonometric functions need to be used. The current FPGA target used does not have a direct implementation of the sine and cosine functions. In order to continue computing in single precision, look up tables for sine and cosine functions is implemented in block memory of the FPGA explicitly.

3. Matrix multiplication block: In every time step, a linear equation involving the admittance matrix needs to be solved. The simulation in current form uses the inverse of the admittance matrix stored in the memory to calculate the variables. In

future, a block to invert the admittance matrix will also be included. Apart from the computation blocks, an asynchronous communication protocol is developed to transfer the information of the variables between the FPGA and the host machine.

## B.3 Results

Implementation of the 9 bus system on LabVIEW FPGA:

The FPGA target used for this simulation is an NI- R series 7822 FPGA. Fig. B.2 shows a summary of the resources utilized in the device for the electrodynamic simulation. For the 9 bus system on 10 % of the memory and registers, around 40% of the Slices, and 30% of Look Up tables are used. With additional optimization, it is hypothesized that the final utilization can be reduced to 10%. Single precision floating point is used in these models as this FPGA target does not support the use of double precision.

A small disturbance is created in order to simulate an electromechanical transient. The change in machine speed and machine angles are shown in the Fig. B.3 and Fig. B.4 respectively. The machine speed changes rapidly initially and eventually stabilizes and settles down to the steady state values. The machine angles also changes but not as rapidly as the machine speed and eventually settles down to a steady state value. Each of the iteration step takes 200 $\mu$s which is 5 times faster than the time step actually needed. A number of optimization techniques commonly used in LabVIEW can also be implemented in the future which may reduce computation time further.

## B.4 Estimation of the Resources for Faster than Real-time Simulation of EI system

An estimation is done based on the following assumptions about the resources and the challenges to build a large scale FPGA based simulator. The following assumptions have been made for this estimation:

1. The system can be automatically divided into smaller parts without much loss of accuracy of the model.

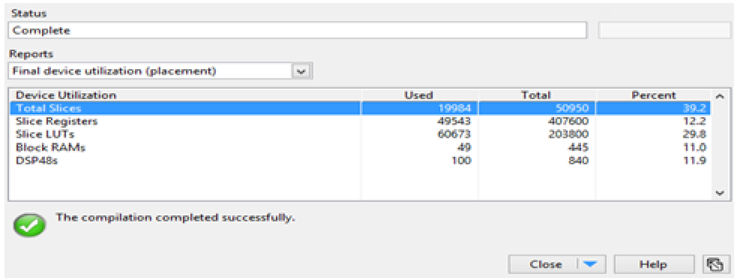
Status
Complete
Reports
Final device utilization (placement)

| Device Utilization | Used | Total | Percent |
|---|---|---|---|
| Total Slices | 19984 | 50950 | 39.2 |
| Slice Registers | 49543 | 407600 | 12.2 |
| Slice LUTs | 60673 | 203800 | 29.8 |
| Block RAMs | 49 | 445 | 11.0 |
| DSP48s | 100 | 840 | 11.9 |

The compilation completed successfully.
Close Help

**Figure B.2:** Device utilization report of the Electrodynamic simulation

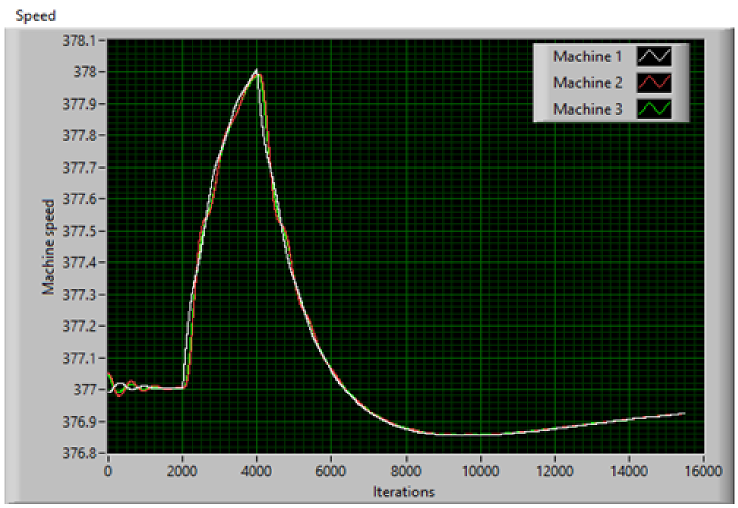


**Figure B.3:** Machine speeds of synchronous generators during a disturbance (9 bus system)

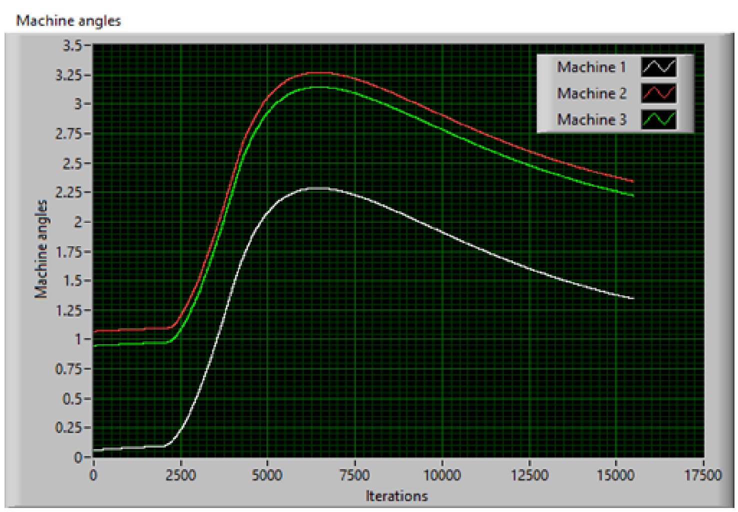


**Figure B.4:** Machine angles of synchronous generators during a disturbance (9 bus system)

2. Double precision (64 bits) data is used for all the variables and constants.
3. The system has been designed with reasonable amount of optimization and pipelining techniques. (This is not the best case scenario possible as the pipe lining technique might itself be too complicated to be implemented.)
4. For this estimation, block memory is considered as default memory used.(In order to use D-RAMs present additional logic needs to be implemented and also the latency is higher for this memory)
5. The generator models used is $9^{th}$ order models that implies 9 differential equations per generator (Includes exciters and governor models).
6. The clock cycle is assumed to be 100MHz (10 ns time period)
7. LU factorization has been done already and all the factors are readily available for the computation units.
8. The specifications used for this assumption is made using FlexRIO 7976R.
9. The explicit backward Euler method is used for this estimation. This is the method used in PSS/E and is not as computationally intensive as the implicit methods like trapezoidal methods which are nonlinear and need to use NR iterations to be solved. (Trapezoidal method is known to be more stable.)

Estimation of the resource required is basically done with respect to the two major parts of the simulator namely, integrator and linear system solver. The transformation block is included with the integrators as they are just 4 additional equations per machine. (2 transformation equations from network to machine and 2 from machine frame of reference to network). The integrator block has to process large number of integration equations in parallel and is optimized with respect to size and speed and pipelined accordingly.

The linear system solver is the other major part of the simulator that will be able to solve Ax=b within 1 time step. There are many possibilities to solve the linear system. For this study two particular methods are considered. One is using the pre-calculated LU factors and the other is using the inverse of the matrix.

For each of these major blocks, an estimation is done assuming that one of these factors namely: memory, computation or communication might be a bottleneck. The final number of FPGAs will have to adhere to the strictest condition. A 9 bus system is also implemented as a part of the project and a practical estimation based on this experimentation has also been documented.

1. Integrator: It is assumed that every generator is represented using $9^{th}$ order model. Thus, there are 9 differential equation that has to be solved for every generator at every time step. In the Eastern interconnect there are 70,000 buses with 8000 generators. Thus 72,000 differential equations would have to be solved in every iteration.

   Memory storage: For every generator there are 9 equations to be solved and there are a total of about 100 constants and variables. The first criteria is the memory constraint. For the purposes of this study, FlexRIO 7976R is used. In order to keep the latency of data retrieval from memory to a minimum the data is assumed to be stored in block memory. The block memory size of 7976R is 8748k bits. 64 bits is needed to store 1 point of data and 16 bits to store the machine number and also constant type. Thus, every machine needs at least 125*64 bits=8k bits. Additional memory is needed for addressing. Hence rounding off, around 1000 machines can be stored in the block memory. With memory being the constraint around 1000 machines can be simulated on 1 FPGA. Hence around 8 FPGAs might be needed just to integrate the entire system. This is assuming that all the computation blocks to carry out the actual operation are present.

   Computation: If 1000 machines needs to be integrated in every time step on every FPGA, there are many possible configurations. Assuming a machine is integrated after the other sequentially but integrate all the differential equations of one machine in parallel. There would be a computation block that can integrate 9 differential equations. However, only 1 machine can be processed at a time. If it is assumed that the time step is 5ms, then in order to complete the integration of all 1000 generators,the integration of every generator has to be completed within $5\mu$s. Assuming the time step is 10ns, about 500 clock cycles is needed to complete an entire set of equations, which is feasible. 2 computation units and process 2 generators can be used at the same time. Thus allowing 1000 clock cycles to complete each generator.

Apart from the integration, the transformation block is included in the integrator. The transformation from network frame of reference to machine frame of reference is done before the integration. After the integration is complete, the variables are transformed into network frame of reference using the current values. One of the complex parts of this block is the trigonometric functions that need to be used. There will be latency when these trigonometric functions are generated. Therefore, the integrator along with transformation of 1000 generators might be possible with 1 FPGA. Thus, around 8 FPGAs is needed for simulating all the equations. Thus if only 1 FPGA is available, it would take 40ms to simulate 5ms time step. Hence, for a simulation of 1s with 5ms time step would actually take about 8s.

Communication: If 1 kByte of data is needed every 5ms, then the communication speed that needs to be handled is 200kB/s, which is not a constraint. By designing a good data and memory transfer onto FPGA, 1000 generators can be processed every time step.

2. Solution of Linear system: For the algebraic equations, the only non-zero entries on the RHS side are the generator buses. Hence, the number of complex linear equations that needs to be solved is equal to the number of generator equations and may be some additional equations as they may have been connected to the normal buses. Hence, the actual number of equations to be solved is increased by 25%.

   Estimation assuming system is solved using LU factors

   Memory: The number of generators present in the eastern interconnect system is around 8,000. The number of complex equations to be solved is assumed as 10,000. Thus, the actual size of the equation to be solved is now 20,000 bus system which is extremely sparse. Assuming that the system is 99.9% sparse, there will be 20 non-zero entries per column. The total number of non-zero elements is now around 400,000 elements. Apart from the 20,000 elements, the addresses of these 420,000 elements will have to be stored.

Memory for the elements =420k*64=26880k

Memory for the pointers=420k*16=6720k

Just in terms of memory space, additional 5 FPGAs will be needed to store all the elements on the block memory of the FPGA. But using LU factors to solve Ax=b will involve complex algorithm that is sequential in nature as depending on the network the columns will have to be processed serially whereas the rows can be processed in parallel.

Computation: Due to the sequential nature of the computation, the worst case scenario of processing every column sequentially is taken as the base case. Using various other optimization techniques, more than one columns can be computed but as seen from device utilization, only around 10-15 computation units (High performance Multiply add units) can be used at the same time. Due to latency in memory retrieval (the sparse structure would need more complicated and sequential addressing compared with inverse matrix approach) and maximum number of computation units is around 10 (as there may be 20 nonzero elements), one parallel set would need 100 cycles and so total amount of cycles required per column would be 200. Hence using the clock frequency of 100 MHz (10ns time step), it would need 2 $\mu$s to process each column. Hence, total columns that can be processed in a time step of 5 ms would be 2,500. As both Lower triangular matrix and upper triangular matrix has to be processed, around 16 FPGAs will be needed to process the computation of LU factorization, assuming LU factors are available.

The critical assumption made in this case is that the entire system can be divided into 16 different regions that can be processed in parallel. In case one of the iterative methods has to be used, then the amount of time taken will increase and so will the number of FPGAs required. There is a way to increase the clock frequency but the resource utilization would increase and then fewer rows can be processed hence taking more amount of time.

Communication: In either of these cases, the data is already assumed to be present on the FPGA. In case the data needs to be communicated, the data transfer rates will be less than 1MB/s. Hence, communication will not be the bottleneck in these cases.

Estimation assuming system is solved using inverse of the matrix

Memory: Every row will have 20,000 elements. So the memory required for every row in block memory is 1280kb. With around 8786kb on Flex-RIO around 8(6) rows can be stored simultaneously. Depending on the computational units, the data retrieval can be pipelined such that the data is available on all the parallel computational unit. Hence in this case, communication and computation blocks will be the main bottlenecks. If the K410T is used which has 28,620 RAM bits about 20 rows can be stored simultaneously. Each computation unit can process up to 25 rows in one time step. Hence, assuming data communication rate is fast and 20 computational unit can be fit and 20*25=500 rows can be computed in every time step. 40 FPGAs will be needed to just solve the linear system of equations. Therefore, storing the inverse of the entire system would not be feasible. A better solution would be to tear the system into smaller parts and then store their inverses.

Computation: In order to utilize the parallel nature of FPGA completely and pre-calculate inverse of A matrix ($A^{-1}$), the total number of non-zero elements will be 400,000k elements. So approximately 400 million multiplication and additions will have to be done in every time step. Assuming a time step of 10 ns. One multiplication-add unit can approximately do 500000 computations in 5 ms. That means it can complete about 25 complete rows. (Each row will have 20,000 computations). With 10 such computation units on each of the FPGA (Assuming each computation unit needs about 10% of the resources. 250 rows can be computed in every FPGA board. Thus 80 FPGA boards would be needed just to solve the linear system of equations with inverse being computed on the host machine. In case 20 computational units are used , the system can be simulated using 40 FPGA boards.

Communication: For every row of the $A^{-1}$ matrix about 20,000 $A^{-1}$ elements and 20,000 elements of x is to be stored. Thus, about 40k *64+40k *16 (data + address) is needed . That is about 3.2Mbits or 400k Bytes. Every 5 ms or the data rate should be around 400kBytes/.005=80Mbytes/s. Considering the transfer rate is 2GB/s, 25 rows worth of data can be transferred within 1 time step.

The summary of the estimation of the resources needed to simulate eastern interconnection is shown in Table B.1

3. Estimation based on experimentation: These estimates are based on the test system developed and tested on NI FPGA 9822R. 9 bus system (3 generators) is simulated faster than real time on 1 FPGA. It took up 40% of the resources. It was simulated with a 40MHz clock. It could simulate one time step in 200 $\mu$s. This system had 3 generators. These FPGAs could go up to 100 MHz but the resource utilization would also increase with increase in frequency of the clock cycle. Some of the high throughput function may not work at this rate.

   Hence 3 generators can be simulated with 40% of the resources at 200 $\mu$s. Utilising 100% of the resources would mean around 8 generators can be simulated for 1 time step within 200 $\mu$s. For 1 second total simulation time with 5 ms time step, the total number of time steps is 200. Hence, for 1 system with 8 generators, 1 second of dynamic simulation can be done in 0.04 s. Extrapolating this estimation to be in real time, around 200 generators can be simulated per FPGA in real time with a time step of 5ms. For 8000 bus system, 40 FPGAs are needed to simulate the Eastern interconnect system. For 100 MHz, an increase in the resources would mean around 5 generators can be simulated for 1 time step within 80 $\mu$s (assuming it takes 8000 cycles). This simulation is 62.5 times faster. Hence around 320 generators can be

**Table B.1:** Number of FPGAs required to simulate Eastern Interconnection

| | Block Memory constraints | Computation Block constraints | Communication constraints |
|---|---|---|---|
| Integrator | 8 | 8 | Not a constraint |
| Linear system solver (LU factors) | 5 | 6 | Not a constraint |
| Linear system solver (Inverse matrix ) | 100(7976 R) or 40 (K410 T ) | 40 | 40 |

simulated per FPGA. Therefore, around 25 FPGAs are needed to simulate the system. This would be the best case scenario. The summary of the estimation is shown in Table B.2.

## B.5 Conclusion

The initial scoping study clearly shows that the communication bottlenecks and timing constraints are not a big hindrance in the case of FPGA based system as have been the case with general purpose processors and Graphical processing units. NI LabVIEW and its graphical programming approach also reduces the complexity involved in programming a FPGA based system through VHDL. This systems needs extensive development before they can compete with the commercially available package. The best case scenario theoretically, would involve using 8 FPGAs for integration and 16 for solving the linear system with LU factors. Based on experimentation, the best case scenario would need around 25 FPGAs. Practically, the number would be closer to 40 FPGAs.

**Table B.2:** Estimation of FPGAs required for simulating EI system based on experimentation

| Clock Cycle frequency | 40 MHz | 100MHz |
|---|---|---|
| Number of FPGAs required | 40 | 25 |

# Vita

Lakshmi Sundaresh was born in Mysore, India. Lakshmi Sundaresh received the Bachelors in Technology degree from National institute of Technology, Karnataka.She received Master in Science degree from Indian Institute of Science, Bangalore in 2014. She is the recipient of the HAY medal from Electrical department of Indian Institute of Science. Her research interests include simulation of large-scale systems, frequency response, and integration of renewable energy resources.